DALHOUSIE UNIVERSITY

Lithospheric flexural controls on landscape evolution during deposition and incision of the Beaufort Formation, western Canadian Arctic

Patrick Manion

SUBMITTED IN PARTIAL FULFILLMENT OF THE REQUIREMENTS FOR
THE DEGREE OF BACHELOR OF SCIENCES, HONOURS
DEPARTMENT OF EARTH SCIENCES
DALHOUSIE UNIVERSITY, HALIFAX, NOVA SCOTIA

April 2017

Distribution License

DalSpace requires agreement to this non-exclusive distribution license before your item can appear on DalSpace.

NON-EXCLUSIVE DISTRIBUTION LICENSE

You (the author(s) or copyright owner) grant to Dalhousie University the non-exclusive right to reproduce and distribute your submission worldwide in any medium.

You agree that Dalhousie University may, without changing the content, reformat the submission for the purpose of preservation.

You also agree that Dalhousie University may keep more than one copy of this submission for purposes of security, back-up and preservation.

You agree that the submission is your original work, and that you have the right to grant the rights contained in this license. You also agree that your submission does not, to the best of your knowledge, infringe upon anyone's copyright.

If the submission contains material for which you do not hold copyright, you agree that you have obtained the unrestricted permission of the copyright owner to grant Dalhousie University the rights required by this license, and that such third-party owned material is clearly identified and acknowledged within the text or content of the submission.

If the submission is based upon work that has been sponsored or supported by an agency or organization other than Dalhousie University, you assert that you have fulfilled any right of review or other obligations required by such contract or agreement.

Dalhousie University will clearly identify your name(s) as the author(s) or owner(s) of the submission, and will not make any alteration to the content of the files that you have submitted.

If you have questions regarding this license please contact the repository manager at dalspace@dal.ca.

Grant the distribution license by signing and dating below.

_____ _____

Name of signatory Date

DALHOUSIE UNIVERSITY

Department of Earth Sciences
Halifax, Nova Scotia
Canada B3H 4R2
(902) 494-2358

DATE: 28 April 2017

AUTHOR: Patrick Manion

TITLE: Lithospheric flexural controls on landscape evolution during deposition and incision of the Beaufort Formation, western Canadian Arctic

Degree: B. Sc. Honours Earth Sciences Convocation: May Year: 2017

Abstract

Lithospheric flexure in response to changing surface loads is an important control on surface processes and topography. The Northwest Passages are a series of waterways in the Canadian Arctic. The passages form interisland channels with depths up to 600 m. Long and in places straight escarpments, which have been previously interpreted as fault-line scarps, border some of the Arctic channels in the eastern Arctic. However, seismic data and field observations suggest the interisland channels in the western Arctic were initially a continuous coastal plain that was subsequently incised by streams and deepened by glaciers.

The uppermost pre-Quaternary unit is the Beaufort Formation. The Beaufort Formation is a sequence of mostly sandy and pebbly braided stream deposits interpreted to have comprised a coastal plain and now interpreted to have extended from Yukon to Ellesmere Island from 3.8 to 2.7 Ma ago. These fluvial sediments and their marine equivalent (part of the Iperk Formation) thicken toward the Canada Basin to 3 km.

This study tests whether the current topography and distribution of the incised Beaufort Formation on the Arctic Islands can be explained by flexure of the Arctic lithosphere in response to: 1) post-Miocene sediment loading of the Arctic continental margin, and 2) Pleistocene incision of the passages. A numerical lithospheric flexure model, gFlex, is applied to test the extent of subsidence by backstripping Pleistocene and Pliocene strata offshore. Models for flexural downwarping by offshore sediment loading predict sufficient flexure to accommodate the subaerially exposed sediments of the Beaufort Formation. The geometry of accommodation space explains the ribbon-like distribution of Beaufort Formation which parallels the Canada Basin margin from Banks Island to Meighan Island. The effect of erosional flexural rebound by channel incision is evaluated by iteratively excavating sediment from the channels until modern bathymetry is achieved after replacing sediment with water in the channels to modern sea-level.

Model experiments with 60-km lithospheric elastic thickness provide the most suitable fit to topography. Peripheral uplift (100's m) on the Arctic islands closely reproduces the topography of Banks and Prince of Wales Island, but the model requires erosion of the channels and the islands since the Beaufort Fm was deposited. The model results, seismic data, and field observations support previous conclusions that erosive ice covered the western Archipelago islands, that ice streams caused much deeper erosion of the channels, and that the Northwest Passages were opened after 2.8 Ma as a result of erosion, not tectonics.

Keywords: Canadian Arctic, flexure models, landscape evolution, Beaufort Formation, erosional isostasy

Table of Contents

Table of Figures

Table of Tables

List of Abbreviations

Units	**Abbreviation**
Eureka Sound Group	ESG
Ballast Brook Formation	BBF
Beaufort Formation	BF

Flexure Terms	Symbol
Bending moment (1D)	$M(x)$
Bending moment (2D)	$\vec{M}$
Deflection	$d(x)$
Density	ρ
Differential shear stress	$V(x)$
Elastic thickness	T_e
Fibre stress	σ_{xx}
Fibre strain	ε_{xx}
Flexural rigidity (constant, 1D)	D
Flexural rigidity (2D)	$\boldsymbol{D}$
Poisson's Ratio	ν
Seismic thickness	T_S
Thermal thickness	T_T
Vector of curvature	$\vec{\kappa}$
Young's Modulus	E

Acknowledgements

I would like to thank my supervisors Dr. Chris Beaumont and Dr. John Gosse for their efforts guiding me through modelling and research practices. I have gained skills in addition to learning a tremendous amount from them. Without their help, this project would not be of the calibre it has reached.

Furthermore, I would like to thank Rod Smith for all of his help with seismic interpretations and access to the Ion-GXT data. Also, I would like to thank Tom Brent, Keith Dewing and others at the Geological Survey of Canada, Arctic Division. Travel to Calgary in the fall would not have been possible without funding provided by the Offshore Energy Research Association (OERA).

Lastly, I would like to thank all faculty, staff and students in the Earth Science department for help and support through this project. Special thanks to the members of the Cosmogenic Radionuclide lab for support and advice, Charlie Walls for all the GIS help, and Djordje Grujic for coordinating ERTH 4200 this year.

Chapter 1 Introduction

The theory of isostasy assumes an equilibrium between the floating lithosphere and underlying viscous asthenosphere (Barrell, 1914). Static buoyancy forces from the underlying viscous asthenosphere support the lithosphere. Dynamical changes in the lithosphere require consequent changes in the static buoyancy forces to achieve re-equilibration (Barrell, 1914). Isostasy modelling is useful for calculating the response from variations in surficial and internal forces of the lithosphere, i.e. changes in mass above the depth of compensation (applied loads) (Barrell, 1914). The depth of compensation is the depth at which the weight of overlying rock is equal everywhere on Earth (Barrell, 1914). At the depth of compensation, the isostatic forces disappear and only hydrostatic forces remain from the flow of the asthenosphere (Barrell, 1914). Mass-balance above the depth of compensation is often applied for modelling isostatic adjustments of the lithosphere (airy isostasy calculation, zero-dimensional case). Adding mass to the surface (deposition) will require the removal of mantle mass below, subsiding the surface to preserve mass above the depth of compensation. Similarly, removing material from the surface (erosion) will require a greater mantle mass above the depth of compensation, uplifting the region to preserve mass. In higher-dimensional isostasy calculations, flexure of the lithospheric plate and underlying flow of the asthenosphere must be considered to understand the regional isostatic adjustment. One and two-dimensional modelling are the primary methods of modelling regional isostatic adjustments from applied loads.

The Northwest Passages are a geologically young feature in the Canadian Arctic (Tozer, 1955) which connect the Pacific, Arctic, and Atlantic oceans through a series of circumpolar waterways (Berton, 2001). The geological effects from the opening of the Arctic channels remain uncertain in our understanding of landscape evolution of the western Canadian Arctic. The focus of this study is to model the isostatic adjustments of the Arctic lithosphere across the western Canadian Arctic in response to the surface processes related to the formation of the Arctic Archipelago. The late-Cenozoic surface processes which led to the formation of the Arctic channels transported sediment from onshore and within the channels to the continental terrace wedge along the eastern margin of the Beaufort Sea. The redistribution of sediment in the western Arctic shaped the landscape through changes in surface loading and resultant isostatic adjustments. Experimental model results presented in this study predict flexure of the Arctic

lithosphere had a significant control on landscape evolution of the western Canadian Arctic, owing to incision of the Arctic channels and sediment loading offshore.

Tectonics and climate change are first-order controls of surface processes. Molnar and England (1990) proposed a link between Cenozoic climate change and surface uplift based on geologic observations globally. Localities observed by Molnar and England (1990) to have substantial Cenozoic surface uplift include the fjords of Greenland and Norway, the Colorado Plateau, the Tibetan Plateau, and the Alps. The timing of such events correlates with well-documented global climate changes, for example, global cooling at the Pliocene-Pleistocene transition 2.6 Ma (Molnar and England, 1990).

The Pliocene saw significantly warmer climates in polar regions (Hansen et al., 2013), reaching as much as 19 °C warmer than today from polar insolation (Rybczynski et al., 2013). Widespread sediment deposition during the Pliocene is observed across the western Canadian Arctic, forming a continuous clastic wedge extending from the Canada Basin-Mackenzie Delta region to Ellesmere Island (Braschi, 2015; Fyles, 1990; McNeil et al., 2001; Miall, 1976, 1984). A large fraction of the continental clastic wedge is the Pliocene-aged Beaufort Formation, a fluvial deposit exposed in a dissected ribbon-like distribution along the western Arctic coast (Fyles, 1990) (Fig. 1.1). The depositional environment for the fluvial component of the Beaufort Formation is interpreted to be a coastal braid plain (Fyles, 1990; Miall, 1976, 1984).

The depositional environment of the Beaufort Formation appears to be similar to the Pleistocene Beaumont Formation in the Texas Gulf Coast and Mississippi Delta regions (Blum and Aslan, 2006). Pleistocene stream and glacial erosion carving the Arctic channels dissected the once continuous coastal plain. The glaciers and streams redistributed sediment in the western Canadian Arctic, driving isostatic adjustments and altering topographic relief on the western Arctic Islands. Recent work from the PoLAR-FIT (PliOcene Landscapes and Arctic Remains, Frozen in Time) research group (Gosse et al., submitted 2017) have advanced the

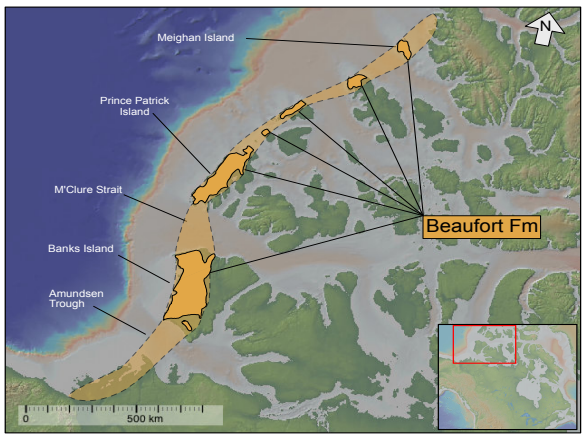

Figure 1.1 Map of the modern subaerial exposures of the Beaufort Formation. Subaerial exposures of the Beaufort Formation are outlined (opaque orange polygons) along the western Arctic Islands, displaying the dissected ribbon-like distribution (transparent orange polygon, dashed lines). Modified from Fyles (1990), base map from Jakobsson (2008).

understanding of the Pliocene Arctic substantially through paleoenvironental, paleobiological and geological studies. However, no previous studies have attempted to quantify late-Cenozoic isostatic adjustments (surface subsidence or uplift) in the western Canadian Arctic related to the Beaufort Formation load and its subsequent incision to form the Northwest Passages.

Two primary geologic observations support the idea that flexure of the Arctic lithosphere had a control on Quaternary landscape evolution in the western Canadian Arctic. One observation is that topographic gradients on several of the western Arctic islands are steeper than that of a coastal plain, suggesting post-depositional tilting of the Beaufort Formation. More indicative, the north-south topographic profiles of some Arctic islands (e.g. Banks Island, Fig. 1.1) are concave up, with elevated regions adjacent to the Arctic channels. While the concave up profile could simply suggest relatively greater erosion in the centre of the islands, some evidence of rock uplift has been observed. For instance, an originally horizontal prominent late Miocene to early Pliocene peat layer on northern Banks Island is observed to have a north-west tilt of approximately 6 m/km (Fyles et al., 1994).

This study has two primary goals. The first goal is to determine the amount of flexure along the western Arctic margin owing to Pliocene-Pleistocene sediment loading offshore. Can the ribbon-like distribution of the Beaufort Formation be explained by accommodation space generated from subsidence from sediment loading? Can the observed tilt of the peat layer be a consequence of flexural downwarping along the Beaufort Sea coast? The second primary objective of this study is to quantify uplift generated from incision of the channels. Can the topographic profiles and gradients on the Arctic Islands be explained by isostatic adjustment from incision of the Arctic channels?

Numerical modelling of the effect of Pliocene-Pleistocene sediment loading offshore and incision of the Arctic channels was accomplished using gFlex, a python based program for elastic deformation of the lithosphere. A conscious decision was made to separate models into two respective groups of experimental models to simplify and clarify results. Project 1 models deal with lithospheric flexure induced by sediment loading offshore. Project 2 models focus on uplift generated from incision of the Arctic channels. Methodology in Chapter 3 outlines the general approach to flexure calculations, providing a derivation for the governing equations for elastic flexure of the lithosphere. For readability, methods for each modelling project are with their respective model results and uncertainties in Chapter 4.

Chapter 2 Geological Background

The following sections will outline the geological framework composing the western Arctic Archipelago. The focus of this chapter is to provide a brief tectonic history, an idea of temporal variations in sediment sourcing, and important climate change events which have impacted landscape evolution of the western Arctic in the Cenozoic.

2.1 Stratigraphic Framework of the western Canadian Arctic

2.1.1 Laurentian Crust and Pre-Cenozoic strata

The southwestern Canadian Arctic Archipelago is underlain by Laurentian crust (Malone et al., 2014). An estimated 14-18 km of undifferentiated Proterozoic bedrock forms the base of the stratigraphic framework based on seismic velocities from reflection and refraction data (Harrison and Brent, 2005). The metamorphosed suite is composed of metasedimentary passive margin rocks and orthogneisses associated with the Grenville-Sveconorwegian Orogen of Laurentia and Baltica (Malone et al., 2014). Up section is a 10-14 km thick package of variably metamorphosed strata of Neoproterozoic to Devonian age, associated with the Franklinian basement sequence in the Alaska and Mackenzie delta regions (Harrison and Brent, 2005; Houseknecht and Bird, 2011) (Fig. 2.1). Importantly, these thick basement packages provide the primary strength of the lithosphere which will be discussed further in Chapter 3.

Jurassic rifting between Canada and Alaska opened the Beaufort Sea (Chian et al., 2016). Rift-related strata form three phases of sedimentation along the Beaufort Sea margins (Houseknecht and Bird, 2011) exposed on several islands in the western Arctic Archipelago (Harrison and Brent, 2005) (Fig. 2.1). Pre-rift strata are passive margin deposits of Mississippian to early-Jurassic age, including carbonates and deltaic successions (Houseknecht and Bird, 2011). Middle-Jurassic to early-Cretaceous syn-rift strata are clastic in nature and derived from the uplifting rift flanks (Harrison and Brent, 2005; Houseknecht and Bird, 2011). Post-rift sediments include late-Cretaceous and early-Cenozoic strata composed of a thick clastic wedge of variable provenance across the Arctic Archipelago (Harrison and Brent, 2005). Post-rift sediments contain bituminous coal of variable maturity (Bustin, 1986; Harrison and Brent, 2005).

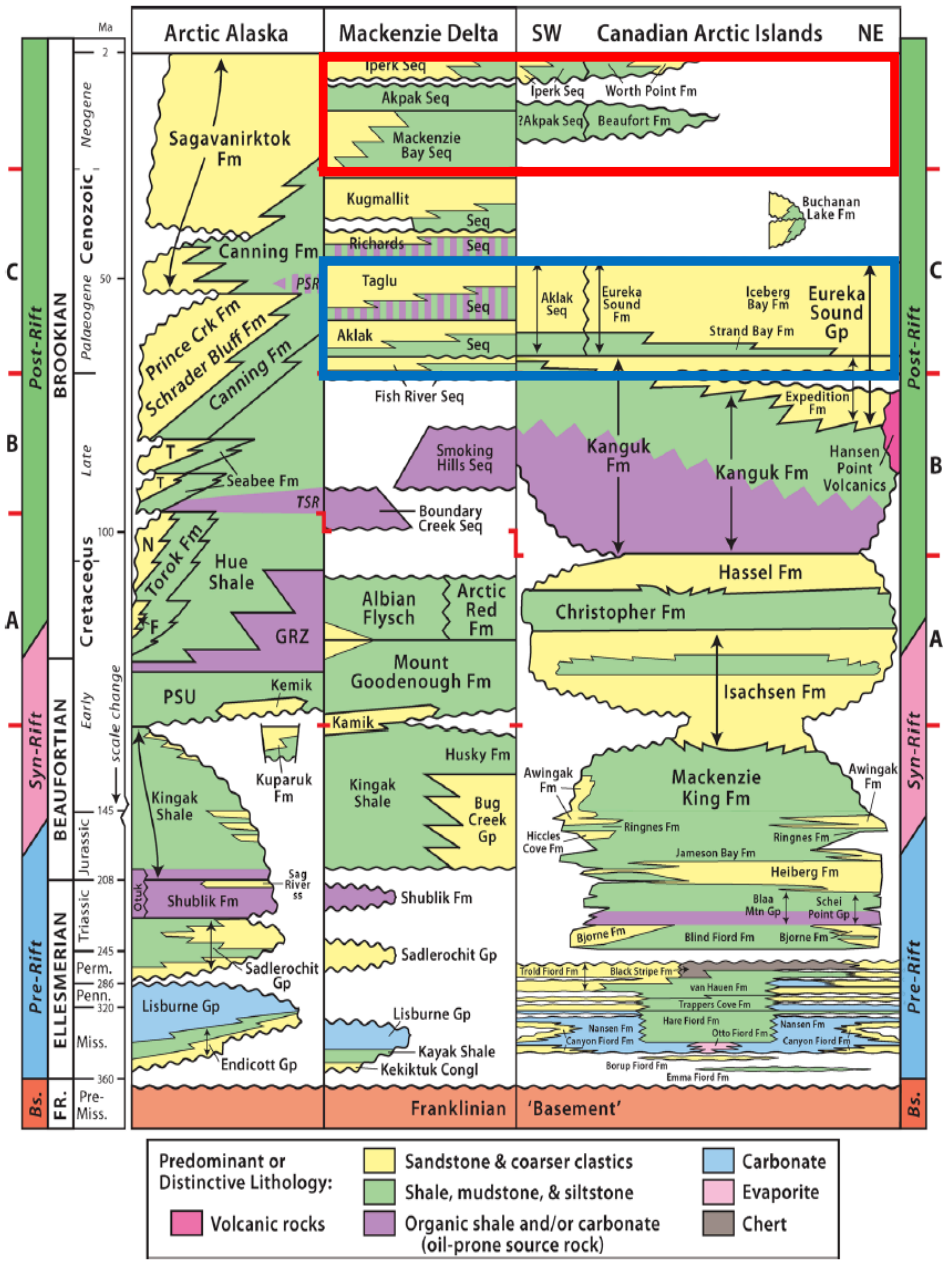

Figure 2.1 Stratigraphic column of the Canadian Arctic islands. Stratigraphic column across the three rift shoulders of the Beaufort Sea from Houseknecht and Bird (2011). The red box highlights the Neogene sedimentary units (Beaufort Formation, Ballast Brook Formation and equivalents). The blue box highlights the Eureka Sound Group and equivalents (ESG). Note, this stratigraphic column is out of date. Unit correlations have changed since publication, such as the Iperk Formation correlating with the Beaufort Formation. The stratigraphic column is provided to provide a geological context for the geological history outlined.

2.1.2 Eureka Sound Group

The Eureka Sound Group (ESG) is a primarily unconsolidated wedge of Paleocene to (latest) Oligocene (Miall, 1976) sediment found in seven intraplate basins across the Arctic Archipelago. Outcrops of ESG stretch as far north as Ellesmere Island and as far east as Bylot Island. The ESG is composed of fluvial and deltaic successions including both marine and non-marine facies containing soft shale beds, silt, sand, lignite coal and braided stream deposits (Miall, 1976). Detritus of carbonised wood characteristic of boreal forests is common in ESG outcrops (Rybczynski et al., 2013). ESG sediments are correlative with the timing of the Eurekan orogeny and postulated to be molasse deposits in some areas (Miall, 1976). Late Cretaceous to Paleogene transpressional shortening as a consequence of oblique-slip motions during pivoting of Greenland relative to the Canadian Arctic (De Paor et al., 1989) led to the Eurekan orogeny. The Eurekan Orogen is exposed in the eastern and northern Canadian Arctic as evidenced by thrusting, strike-slip faulting, and folding (Miall, 1984). The highlands generated may have supplied sediment for the ESG (Miall, 1984). ESG sand facies are composed of mostly quartz (Fyles, 1990) and have a maturity comparable to deposits of the Mississippi Delta (Miall, 1976). The thick sequences of the ESG spanned most of the western Canadian Arctic. Similarities between the ESG and overlying Beaufort Formation suggest the ESG sediments provided large amounts of sediment for the Beaufort Formation (Braschi, 2015).

2.1.3 Ballast Brook Formation

While post ESG strata were undoubtedly deposited in local basins and along the western rift margin their onshore exposure is limited to banks along a 10 km reach of Ballast Brook (north-west Banks Island, Fig 2.2). The Miocene Ballast Brook Formation (BBF) is up to 40 m thick in the valley (Fyles et al., 1994). It is separated from the Pliocene Beaufort Fm. By an angular unconformity. The BBF contains sandy and silty clay strata with characteristically compressed peat beds and compressed woody detritus. The depositional environment is interpreted as a combination of braided and meandering streams with accompanying overbank, floodplain-pond, and back swamp deposits (Fyles et al., 1994). Paleomagnetic, palynological, and insect fossil records place the BBF early to mid-Miocene in age (23-13 Ma) (Barendregt et al., 1998; Fyles et al., 1994; Matthews and Ovenden, 1990). The prominent feature of the BBF is a 2-4 m thick autochthonous peat at or near the top of the formation. The erosional surface (Miocene-Pliocene Unconformity) between the BBF and overlying Beaufort Formation intersects the peat layer at a

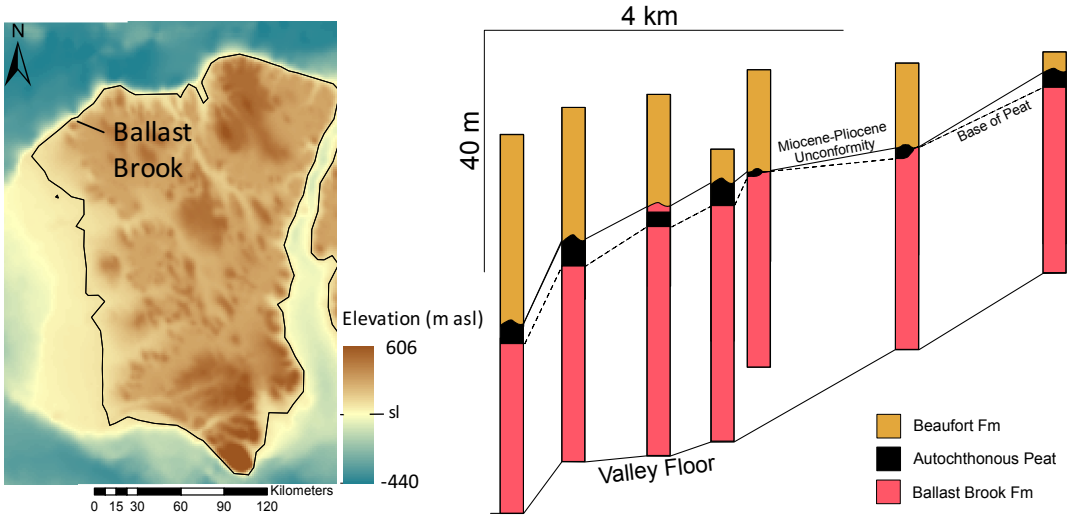

Figure 2.2 Stratigraphic correlation for peat layer at Ballast Brook. Stratigraphic correlation for the Miocene-Pliocene unconformity over several sites at Ballast Brook (above left, black line). Note the near parallel behaviour of the peat layer and the Miocene-Pliocene unconformity. The peat is observed to have a tilt of approximately 6.4 m/km. Stratigraphic correlation modified from Fyles (1994), map from Jackobsson et al (2008).

very shallow angle and appears parallel to the peat over short distances (< 1 km). Peat accumulation requires no topographic gradient because stagnant water is required (Moore and Bellamy, 1974). However, at Ballast Brook, measurements show a significant tilt in the prominent peat bed, approximately 6 m/km (Fyles et al., 1994) (Fig 2.2). There is no previous indication of a tectonic origin for the observed tilting of the peat although we cannot preclude that the peat has been tilted during rifting. It is possible that other processes may have caused the post-depositional tilting. One plausible interpretation is that flexural downwarping induced by Pliocene-Pleistocene sediment loading offshore has tilted the peat layer. How much tilting of this peat bed, if any, can be attributed to flexure from sediment loading offshore? Phase 1 modelling of the study will test if the tilt of the peat bed is the result of lithospheric flexure from sediment loading offshore.

2.1.4 Beaufort Formation

The Beaufort Formation (BF) is an unconsolidated lithostratigraphic unit that is exposed subaerially in a dissected ribbon-like distribution along the western margin of the Canadian Arctic Archipelago (Fig. 2.3). The BF consists of unconsolidated quartz-rich sands and gravels containing some lithic fragments and chert. The dominant depositional environment is gravel-

bearing sandy braided streams (Fyles, 1990). A significant characteristic of the BF is the ubiquitous presence of undeformed detrital wood as large as 40-cm diameter tree boles, which is distinct from the Ballast Brook Formation which contains deformed and more coalified wood fragments. It has been postulated that the BF was the result of long-term deposition along a continuous braid plain extending from the Mackenzie Delta region to Ellesmere Island (Braschi, 2015; Fyles, 1990; McNeil et al., 2001; Miall, 1976, 1984). Paleo-flow directions measured on Banks Island and Prince Patrick Island are generally toward the Canada Basin and do not deflect towards any of the modern inter-island straits or channels. This indicates the Arctic channels were not present during deposition of the Beaufort (Fyles, 1990).

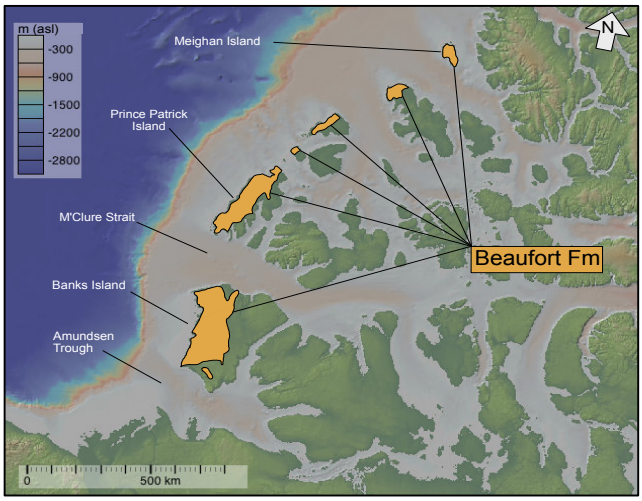

Figure 2.3 Map of BF exposures. Dissected ribbon-like subaerially exposed sections of the BF along the western Arctic margin. Outcrops annotated from Fyles (1990), basemap from Jakobsson et al. (1990).

Chronostratigraphic control of the BF has been of interest over the last several decades because of the abundance of subfossilized paleoenvironmental records that have provided some of the world's best records of fauna, flora, and climate proxies. Its age was restricted to the Pliocene (5.3 to 2.6 Ma) by biostratigraphy (Matthews and Ovenden, 1990) and magnetostratigraphy (Barendregt et al., 1998). Amino acid racemization and Sr dates from marine shells on Meighan Island (Brigham-Grette and Carter, 1992) indicated that an estuarine deposit there dated >2.4 ± 0.5 Ma and 2.8-5.1 Ma respectively. On Ellesmere Island, terrestrial cosmogenic nuclide burial dating using ^{26}Al and ^{10}Be has yielded ages of $3.4^{+0.6}_{-0.4}$ Ma for a fossil reach peat (Beaver Pond Site) and $3.8^{+1.0}_{-0.7}$ Ma for the Fyles Leaf Bed (Rybczynski et al., 2013), $3.5^{+0.6}_{-0.4}$ Ma for sediment above the Meighan Island estuarine deposit, and >2.7 Ma on northern Banks Island (Braschi, 2015). Correlative deposits in the Yukon (White Channel Gravel) yield burial ages that also range from 3.8 to 2.8 Ma (Gosse et al., in prep). Paleo-erosion rates can be estimated using TCN dating for the catchment supplying sediment to the region. Paleo-erosion

rate estimates vary substantially, reaching 178 $^{+27}/_{-21}$ cm/ka for the BF on Banks Island (Braschi, 2015).

The BF is correlative to the Pliocene offshore Iperk Formation (Fig. 2.4). The relatively large volume of Pliocene sediment reaches up to 3 km thick offshore (McNeil et al., 2001) owing to an apparent 23-fold increase in sedimentation rates during the Pliocene (Braschi, 2015; McNeil et al., 2001). Can the dissected ribbon-like distribution of the BF be explained by an increase in accommodation space provided during subsidence from sediment loading? Phase 1 models will estimate the amount of subsidence along the coast from the deposition of the BF.

The source of sediment for the BF is variable along the Archipelago. For example, Axel Heiberg was the source for volcanic lithic fragments in the BF on Meighen Island (Fyles, 1990) but BF on Banks Island appear to have a source from the south and east. Given the similarity between the ESG and BF, sediment from the underlying unconsolidated formations is likely the primary source of sediment. Formations which likely supplied sediment to the BF include the ESG, sandy members of the Hassel and Kanguk Formations (Fig. 2.1) and the BBF (Braschi, 2015).

Many significant paleoenvironmental and climatic records are preserved within the BF, such as fossils of Pliocene camels (Ballantyne et al., 2006; Chandan and Peltier, 2017; Csank et al., 2011; Rybczynski et al., 2013). The Pliocene was characterised by warmer mean global temperatures, estimated 2 $^{\circ}$C warmer than the present (Fig 2.4). However, owing to the contemporaneous shallowing of the latitudinal thermal gradient, it is estimated the Canadian Arctic was approximately 19°C warmer than present based on tree-ring isotopes, paleovegetation, and tetra-ether in bacterial lipids (Ballantyne et al., 2010; Chandan and Peltier, 2017). The lack of snow and sea-ice decreased summer albedo and increased regional warming. Furthermore, if the Pliocene Arctic landscape consisted of a continuous landmass the summer temperatures would have been more extreme than today. The climate proxies also reveal that the winters were even warmer relative to today (Ballantyne et al., 2006; Chandan and Peltier, 2017; Csank et al., 2011; Rybczynski et al., 2013). Warming allowed for boreal-type forests (Matthews and Ovenden, 1990; Rybczynski et al., 2013) to cover most of the Pliocene landscape as evidenced by logs, leaf beds and an abundance of wood detritus.

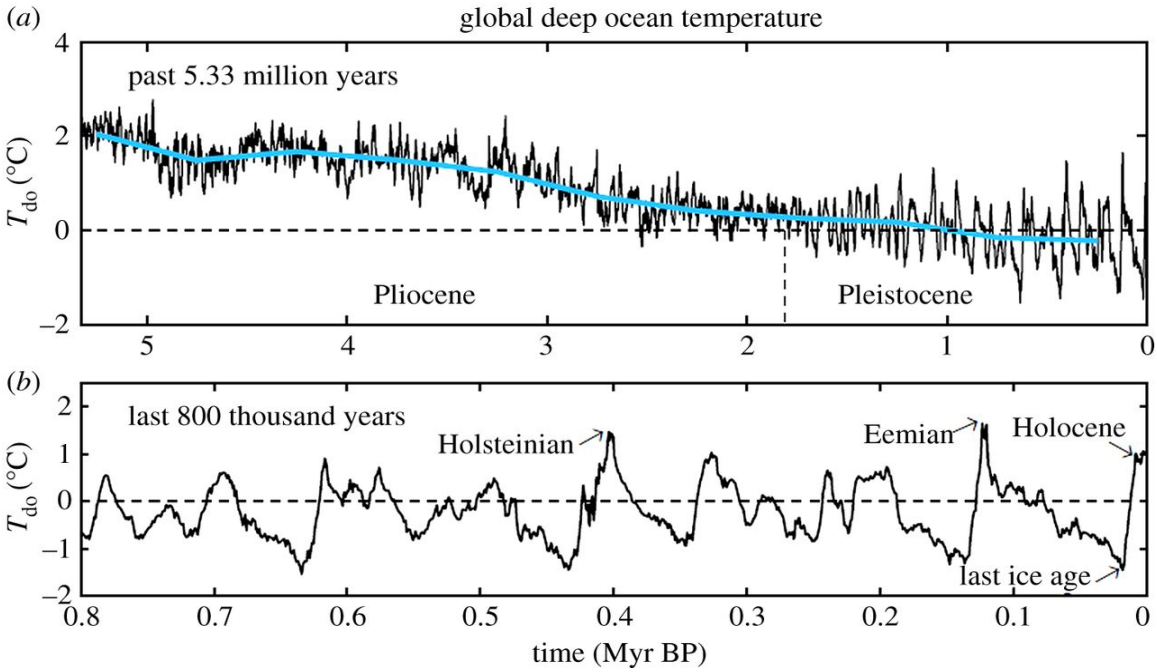

Figure 2.4 Pliocene-Pleistocene global temperature records from Hansen et la. (2013)(a) Mean annual global temperature records for the Pliocene and Pleistocene from δ18 O deep ocean records. (b) Higher resolution late-Pleistocene (last 800 ka) global temperature records. Evident glacial and interglacial periods in high frequency temperature variations.

What are the effects from post-Pliocene incision of the channels? How much isostatic compensation has occurred from incising the deep (600 m in areas) Arctic channels? Experiment 2 modelling in this study will focus on answering these questions through erosional isostasy modelling of the western Canadian Arctic.

2.2 Pleistocene glaciations

Second only to the deposition of the BF, erosion and sedimentation during the numerous Quaternary glaciations contributed significantly to landscape evolution across the Canadian Arctic (England et al., 2006). The Pleistocene was a period dominated by a high variability in global mean temperature, particularly during the five-major eccentricity-dominated glacial cycles (Hansen et al., 2013; Lisiecki and Raymo, 2005) (Fig. 2.4). The separation of Arctic Islands from a continuous landmass may potentially be explained entirely through glacial erosion. One of the earliest hypotheses relates Laurentide Ice Sheet dynamics to the incision of the passages during the Pleistocene (Dyke and Prest, 1987). Fast-moving warm-based glaciers and ice streams

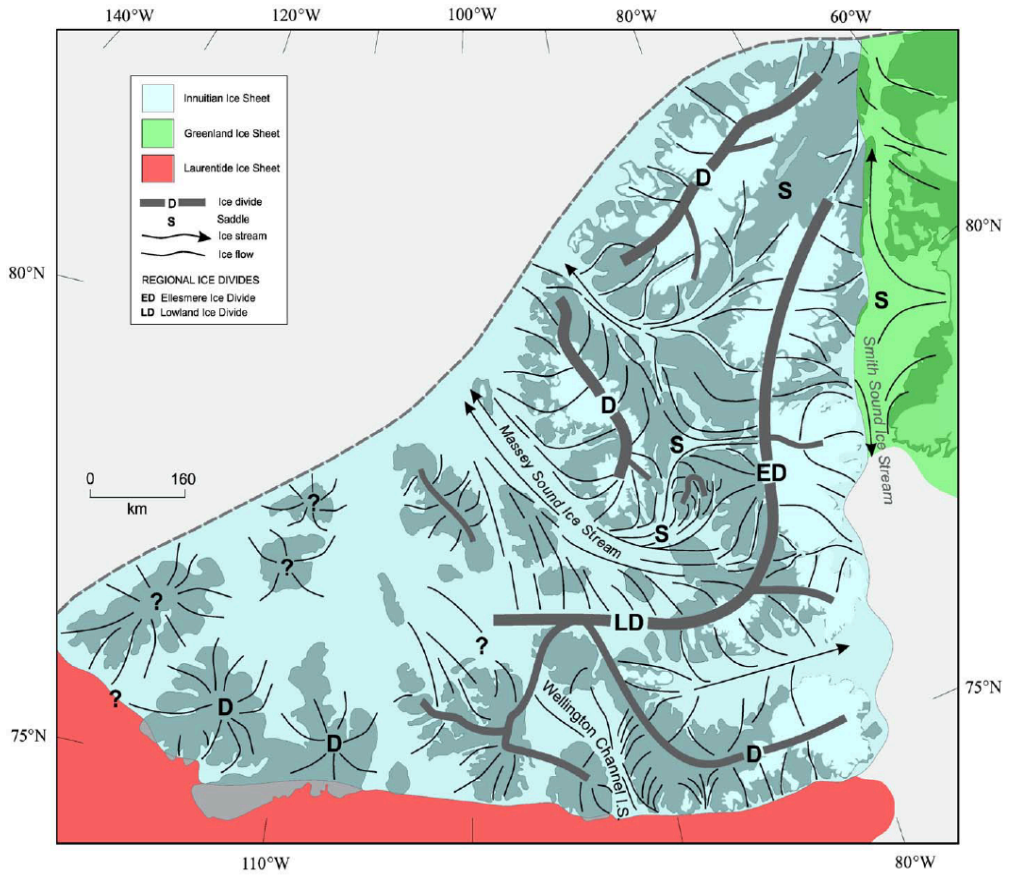

Figure 2.5 Ice sheet reconstruction for the last glacial maximum. Innuitian Ice Sheet reconstruction from the last glacial maximum from England et al. (2006). Ice streaming is interpreted to have occurred among the extant Arctic islands, carving the modern Arctic channels. The extant Arctic islands were covered by cold-based glaciers or ice-divides and ice caps.

occupied the interisland regions, creating channels of erosion, whereas regions occupying extant islands were preserved, or relatively less-eroded, under cold-based glaciers and ice-caps (England et al., 2006; Lakeman and England, 2012). Ice-streams, accelerated regions of ice within an ice-sheet, are likely the primary cause of differential erosion under the Innuitian and Laurentide ice sheets during Pleistocene glaciations. Reconstructions of the Innuitian and Laurentide ice sheets show ice streaming in many of the Arctic channels (England et al., 2006) (Fig 2.5). Recent findings have shown ice thickness was likely sufficiently thick (at least 1000 m) to ground the ice-streams and avoid floating (England et al., 2006), allowing for ice-streaming to erode below sea-level. Further evidence for late-Wisconsinan ice-streaming is present in Amundsen trough (MacLean et al., 2015) and M'Clure Strait (Stokes et al., 2005) While it is probable that fluvial incision during late-Pliocene sea-level fall may have initiated the Northwest Passages, the observation that all but one age indicates that the BF was abandoned

after 2.7 Ma and the lack of paleoflow deflections towards the channels strongly support the predominantly glacial origin of the Northwest Passages.

2.3 Geological uncertainties

Several geological uncertainties exist at this time for the Cenozoic deposits in the western Canadian Arctic. Data limitations are present as the region has little economically viable resources and therefore research funding is limited.

Seismic data is limited along the western Arctic margin as industry is not currently interested in the region. Seismic data is predominantly found for the Canada Basin, a known hydrocarbon reservoir. Therefore, it is hard to constrain the thickness of the units of interest in this study (Pliocene and Pleistocene). Seismic interpretations from the Arctic Division of the Geological Survey of Canada (Calgary, AB) (Appendix B) do not provide sufficient extents on the desired sedimentary packages. Spatial extrapolation of the surface depths was required outside the seismically mapped regions, with increasing uncertainty in unit thicknesses away from Banks Island. Further seismic data with full coverage of Pliocene and Pleistocene sedimentary packages would allow for more quantitative analyses in the region.

The dissected ribbon-like distribution of the BF (oldest 2.7 Ma) suggests incision of the Arctic channels began in the Pleistocene, within the last 2.7 Ma. Continuous deposition of the BF from Banks Island to Meighan Island would not be possible if the channels were present. Therefore, the Arctic channels were not present or filled with sediment during the Pliocene.

A distinction must be made between erosion of bedrock and sediment in the channels. Erosion of bedrock constitutes the formation of the channels. From core records and seismic interpretations, the idea that sediment filled the channels in the Pliocene is more plausible. ESG and BF sediments are observed at the base of Amundsen Trough and M'Clure Strait. Pliocene deposition in the channels is not possible if the channels had not formed then. Therefore, the assumption was made that the Arctic channels did not exist during the Pliocene and were subsequently excavated from fluvial and glacial erosion. This follows the ideas from England (1987), suggesting the channels formed from large Cretaceous grabens which were subsequently filled with Tertiary sediment. However, the seismic data does not show large faults binding M'Clure Strait and Amundsen Trough and therefore do not agree with a graben geometry for the channels. The significance of this assumption will be further discussed with the uncertainties in the erosional isostasy models (§4.1.3).

2.4 Hypotheses

The questions sought to answer in this study pertain to late-Cenozoic sediment loading offshore and incision of the Arctic channels. The following will reiterate the questions and provide the hypotheses established prior to modelling.

The goal of project 1 was to provide a first-order approximation for the late-Cenozoic flexural subsidence along the western Arctic margin. Is the dissected ribbon-like distribution of the BF explainable by Pliocene sediment loading offshore? Hypothesis 1a: the orientation, width, and thickness of the currently exposed BF is consistent with the geometry and orientation of the accommodation space generated by sediment loading offshore. Did sediment loading offshore tilt the Arctic coast basinward from flexural downwarping? Hypothesis 1b: The tilt of an originally horizontal Miocene peat bed should be basinward and equal or greater than that predicted by loading from deposition of the Pliocene and Pleistocene sediments.

project 2 addressed the effects of incision of the channels on the western Arctic islands. Can the elevated regions on some of the Arctic islands be explained by the regional isostatic response from incision of the channels? Hypothesis 2a: The elevated regions of the Arctic islands are a result of uplift from incision of the Arctic channels. Are the concave up topographic profiles of some Arctic islands the result of uplift from incision of the channels? Hypothesis 2b: The concave up topographic profiles are the result of greater uplift on the Arctic islands near the channels.

Chapter 3 Modelling

This chapter provides an overview of the principles and equations governing lithospheric flexure modelling (§3.1), programs used for modelling (§3.2), flexure in 1D (§3.3), and model sensitivity analyses (§3.4). Detailed methods used in each model experiment are included in Chapter 4. The last section (§3.5) outlines similar studies for which some concepts in this study were drawn from.

3.1 Principles for elastic flexure of the lithosphere

3.1.1 The lithosphere

The crust and uppermost mantle comprise the lithosphere, Earth's strong outermost mechanical layer. The strong, thin lithospheric plates move on and in the rest of the mantle. Lithospheric dynamics is driven by the fluid-like behaviour of the underlying asthenospheric mantle which flows over geologic timescales. However, lithospheric rocks behave as an elastic solid under short periods (10's Ma) of stress, accommodating stress without incurring permanent deformation (Eaton et al., 2009). The ability for the lithosphere to support significant loads, such as mountain belts, over geologic timescales supports the idea that part of the lithosphere behaves as an elastic solid. The elastic lithosphere describes the upper part of the lithosphere which can support applied loads elastically without incurring permanent deformation (Eaton et al., 2009). The seismic lithosphere is defined as the high velocity outer layer of the Earth that rests above a low velocity layer (Eaton et al., 2009). The base of the thermal lithosphere, the upper part of the Earth cooled by conduction (Eaton et al., 2009), roughly corresponds to the depth of the 1200°C (±100°C) isotherm (Turcotte and Barry, 1979). From studies of relaxation of elastic stress in the lithosphere, the thickness of the elastic lithosphere roughly corresponds to the depth of the 600°C (±100°C) isotherm (Caldwell and Turcotte, 1979; Turcotte and Barry, 1979). Geothermal gradients vary spatially and temporally and therefore isotherms do not correlate to a constant depth. Thus, the elastic thickness and strength of the lithosphere can vary at sub-plate scales.

3.1.2 Applied loads and deflection

Lithospheric flexure is defined as bending of the lithosphere to support applied loads and can be used to estimate regional isostasy (Barrell, 1914; Turcotte and Barry, 1979). Kirchoff-Love plate theory is often applied to calculate vertical motions associated with lithospheric flexure from an assumed flat earth, under the assumption that wavelengths of deflection are significantly

shorter than the radius of the Earth (Turcotte and Barry, 1979). Kirchoff-Love plate theory is an expansion of 1D Euler-Bernoulli beam theory that provides a 2D mathematical model for calculating the stresses and elastic deformation from forces and moments acting on a thin plate (Turcotte and Barry, 1979). Flexure is generated from isostatic buoyancy restoring forces generated within the lithosphere. Restoring forces generated are proportional to the deflection and local buoyancy of the plate. In Euler-Bernoulli beam theory and Kirchoff-Love plate theory the isostatic restoring forces are applied at the base of the lithosphere with constant flexure through the beam or plate at a given point. The following derivation will outline flexure of a 1D beam based on Turcotte and Barry (1979), Burov (2010), and Wickert (2016).

The thickness of the modelled plate is not equivalent to the thickness of the seismic (T_S) or thermal lithosphere (T_T) but is equivalent to the thickness of the elastic lithosphere (Barrell, 1914; Eaton et al., 2009; Turcotte and Barry, 1979). The thickness of the modelled plate is termed the equivalent, or effective elastic thickness (T_e) (Burov, 2010; Burov, 2011; Eaton et al., 2009; Tesauro et al., 2012; Turcotte and Barry, 1979). T_e is a proxy for the regional strength of the lithosphere (Barrell, 1914; Burov, 2011) which is determined by the time-dependent relaxation of the lithosphere (Turcotte and Barry, 1979) and residence time of applied loads. The relaxation of stress in the lithosphere is from higher temperatures in the lower lithosphere. Deformation of the lithosphere initially involves flexing of the lithospheric plate to support loads with a thickness similar to the T_T. However, the lower lithosphere is too hot to sustain the flexural fibre stresses in the plate. The lower lithosphere therefore relaxes these stresses until all stresses for regions above the 600°C isotherm have been relaxed. Therefore, over geologic timescales the flexural rigidity of the plate appears to correlate to the 600°C isotherm. Similarly, T_S is inferred to reach a depth of 220 km, where radial seismic anisotropy is seen in the earth (Eaton et al., 2009). T_e on Earth are observed to be substantially less than 220 km (120 km at most (Burov, 2011)). Therefore, the elastic lithosphere is thinner than both the thermal and seismic lithosphere.

Lithospheric flexure under the flat earth assumption for an applied load ($q(x)$) is described by a fourth-order ordinary differential equation (derived below). The solution is the deflection or vertical motion of the lithosphere during flexure ($d(x)$).

Let x be the distance along the undeformed beam and z the vertical distance from the reference position halfway through the beam (the midpoint). By definition, the top and bottom of

the beam are $\frac{T_e}{2}$ and $\frac{-T_e}{2}$, respectively. A second coordinate system must be defined for analysis of the deformed state of the beam, denoted x' and z' (Fig. 3.1).

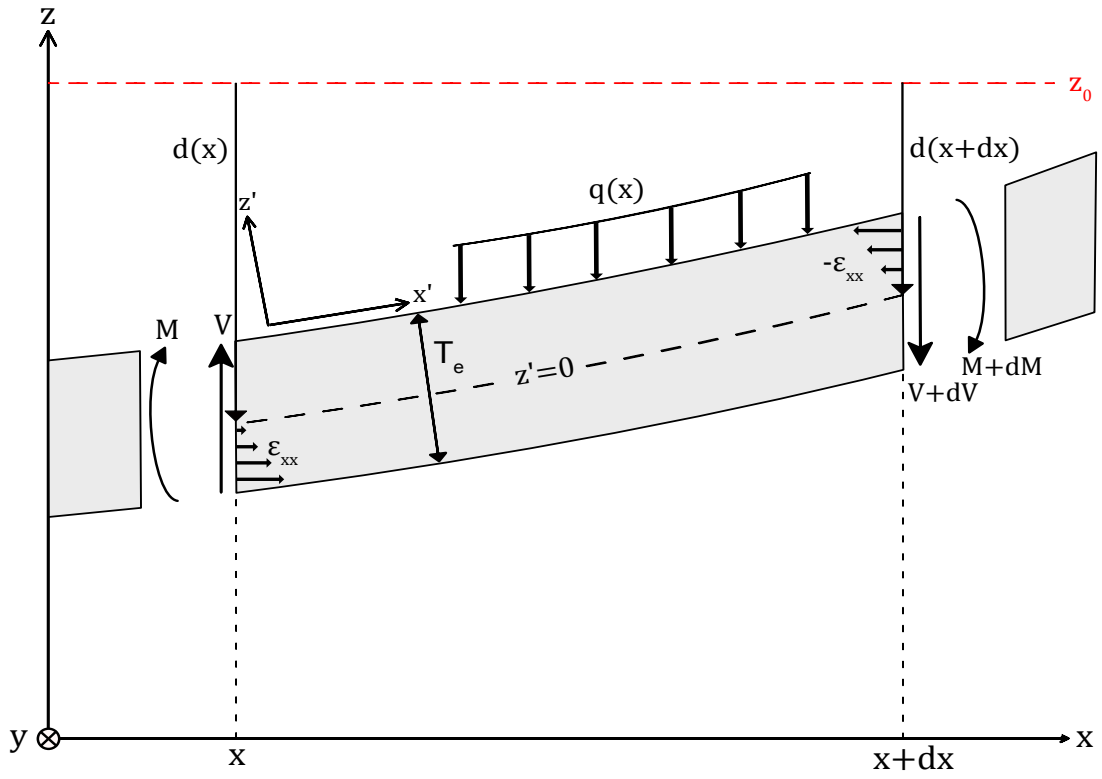

Figure 3.1 Forces and moments acting on a beam. Schematic representation of the forces ($V(x)$) and moments ($M(x)$) acting on an infinitely small length (dx) of a beam under applied vertical stresses by a load ($q(x)$). Figure modified from Turcotte and Schubert (1979).

Stress is defined as the applied force per unit area exerted on a material and strain is the resultant deformation. Elastic deformation results in longitudinal fibre stresses (σ_{xx}) that vary with depth in the beam. The midpoint (layer halfway through the beam, $z' = 0$) experiences zero net compression or tension. Young's Modulus (E) (GPa) is a measure of the elastic strength of the beam and defines the deformational relationship between stress and strain for a material. Poisson's Ratio (v) is a measured comparison of shortening to lengthening in a given material under stress. Fibre strain ($\varepsilon_{x'x'}$) in each layer of the plate is referenced to z' because strain increases away from the midpoint. The deflection ($d(x)$) is assumed significantly smaller (often an order of magnitude) than the wavelengths of deflection generated (λ). Since $d(x)$ is the measure of the vertical motions and z' is the vertical distance from the plate, $d(x) = z'$ and then fibre strain in the x' direction ($\varepsilon_{x'x'}$) is equal to the fibre strain in the x direction (ε_{xx}) (Eq. 1).

The assumption $\varepsilon_{x'x'} = \varepsilon_{xx}$ makes no difference in the flexure calculation following from the small deflection assumption.

$$\varepsilon_{xx} = \varepsilon_{x'x'} = z' \frac{d^2 d(x)}{dx^2} \quad (1)$$

The bending moment ($M(x)$) of the plate is a function of the fibre stresses ($\sigma_{x'x'}$) and their respective lever arm (z') (Eq. 2). Integrating the fibre stresses ($\sigma_{x'x'}$) over T_e, $M(x)$ can be approximated in terms of the sum of fibre stresses (σ_{xx}) (Eq. 2). Applying the elastic relationship from Hooke's law (Eq. 3 and 4), $M(x)$ can be written in terms of the fibre strain ($\varepsilon_{x'x'}$) (Eq. 5).

$$M(x) = \int_{\frac{-T_e}{2}}^{\frac{T_e}{2}} \sigma_{x'x'} z' dz' \quad (2)$$

$$\sigma_{x'x'} = E\varepsilon_{x'x'} + v\sigma_{y'y'} \quad (3)$$

$$\sigma_{y'y'} = E\varepsilon_{y'y'} + v\sigma_{x'x'} \quad (4)$$

$$M(x) = \frac{E}{1 - v^2} \int_{\frac{-T_e}{2}}^{\frac{T_e}{2}} \varepsilon_{x'x'} z' dz' \quad (5)$$

For the 1D case, $\varepsilon_{y'y'}$ and $\sigma_{x'x'}$ are zero. E and v are constants and can be factored out of the integrand. Thus, $M(x)$ is a function of both material properties (E, v and T_e) and the curvature of the deflection ($\frac{d^2 d(x)}{dx^2}$). The material properties form a constant elastic property called the flexural rigidity (D) (Pa·m^3) (Eq. 6). D is a measure of the resistance to bending the beam exhibits, that is the ratio of the applied bending moment to the resulting curvature. D is a function of the third power of T_e (Eq. 6). Regions with a thicker elastic lithosphere (larger T_e) are stronger and therefore will incur less bending under applied loads. $M(x)$ can thus be written in terms of the flexural rigidity of the beam and the curvature of deflection (Eq.7).

$$D = \frac{E\, {T_e}^3}{12(1 - v^2)} \quad (6) \qquad M(x) = D \frac{d^2 d(x)}{dx^2} \quad (7)$$

Summing the forces acting on the beam provides an equation for deflection in terms of differential shear stress (the difference between greatest and least compressive stresses ($V(x)$)

(Eq. 8). A relationship between $M(x)$ and $V(x)$ is derived by summing the torque (bending moment) acting on the beam (Eq. 9). Substituting $V(x)$ in terms of D and $d(x)$, the differential equation for flexure becomes Eq. 10 and is valid for a constant D.

From the principle of isostasy, the net load ($q(x)$) must equal the total restoring forces acting on the beam. The buoyancy restoring forces driving lithospheric flexure are the forces opposing loading to balance the system which are generated from the displacement of fluid asthenosphere ($\Delta\rho g d(x)$)(Eq. 8, 10) (Turcotte and Barry, 1979). The restoring force is proportional to the density contrast ($\Delta\rho$ where $\Delta\rho = \rho_m - \rho_f$) (Eq.12) between the mantle (ρ_m) and the material infilling the depression generated from deflection (ρ_f) (for instance, the net density of water and sediment).

$$\frac{dV(x)}{dx} - \Delta\rho g d(x) = -q(x) \quad (8)$$

$$V(x) = -\frac{dM(x)}{dx} = -\frac{d}{dx}\left(D\frac{d^2 d(x)}{dx^2}\right) \quad (9)$$

$$D\frac{d^4 d(x)}{dx^4} + \Delta\rho g d(x) = q(x) \quad (10)$$

The solution to the differential equation (Eq. 10) is a sinusoid, with deflection that exponentially increases or decreases laterally (Eq. 11). Deflection cannot increase exponentially laterally from the load and requires the increasing exponential portion (positive exponential in Eq.11) to be negated, leaving a dampened sinusoidal function (negative exponential Eq.11). The flexural parameter (α) (Eq.12) arises in the solution (Eq. 11) and is the distance from the maximum deflection (x_0 in Fig. 3.2) to the point of zero deflection (x_α in Fig. 3.2). The flexural parameter (α) is proportional to the flexural wavelength (λ) (Eq. 13) which is the wavelength of the deflection function ($d(x)$).

$$d(x) = e^{\frac{x}{\alpha}}\left(C_1\cos\frac{x}{\alpha} + C_2\sin\frac{x}{\alpha}\right) + e^{-\frac{x}{\alpha}}\left(C_3\cos\frac{x}{\alpha} + C_4\sin\frac{x}{\alpha}\right) \quad (11)$$

$$\alpha = \left(\frac{4D}{g(\rho_m - \rho_f)}\right)^{\frac{1}{4}} \quad (12)$$

$$\lambda = 2\pi\alpha \quad (13)$$

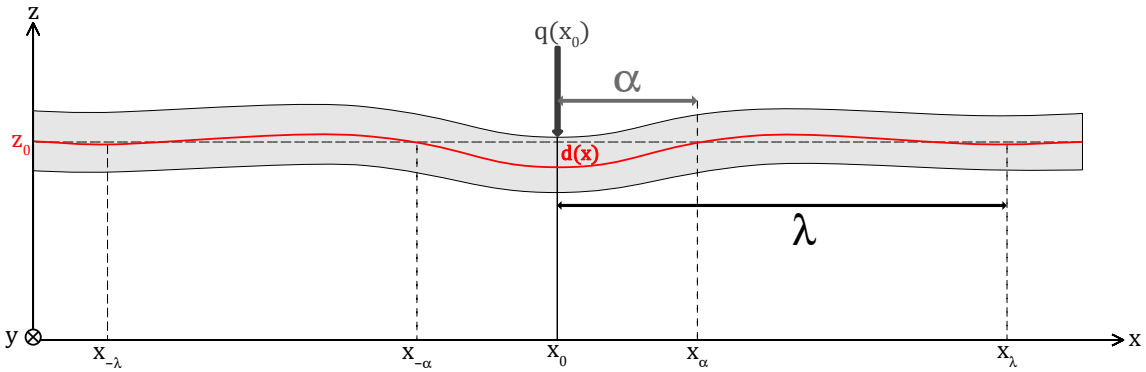

Figure 3.2 Schematic diagram for flexure of a 1D beam under an applied point load. The deflection (red line, $d(x)$) shows the deflection of the midpoint of the beam away from equilibrium. The flexural parameter (gray, α) and flexural wavelength (black, λ) are shown. Modified from Turcotte and Schubert (1979).

The expansion from 1D Euler-Bernoulli beam theory to 2D Kirchoff-Love plate theory involves partial differential equations for the flexure in the x and y directions, as the stress and strain in the y' direction is no longer zero ($\sigma_{y'y'} \neq \varepsilon_{y'y'} \neq 0$). A vector of curvature is required ($\vec{\kappa}$) (Wickert, 2016), which describes the curvature of deflection ($d(x,y)$) of the plate in 3D space (Eq.14). Furthermore, the flexural rigidity must be defined in 3D space (Eq. 15). The bending moment ($\vec{M}$) can then be defined for a 2D plate in a similar manner to that in 1D, i.e. it is the product of the flexural rigidity and the curvature of deflection (Eq. 16) (Turcotte and Barry, 1979; Wickert, 2016). The differential equation (Eq.10) becomes a partial differential equation for the deflection of a thin 2D plate in the x and y directions ($d(x,y)$) under an applied load ($q(x,y)$) (Turcotte and Barry, 1979).

$$\vec{\kappa} = \begin{bmatrix} \dfrac{\partial^2 d(x)}{\partial x^2} \\ \dfrac{\partial^2 d(x)}{\partial y^2} \\ \dfrac{\partial^2 d(x)}{\partial x \partial y} + \dfrac{\partial^2 d(x)}{\partial y \partial x} \end{bmatrix} \qquad 14$$

$$\boldsymbol{D} = \begin{bmatrix} 1 & \upsilon & 0 \\ \upsilon & 1 & 0 \\ 0 & 0 & \dfrac{1-\upsilon}{2} \end{bmatrix} \qquad 15$$

$$\vec{M} = \boldsymbol{D}\vec{\kappa} \qquad 16$$

3.2 Modelling program

3.2.1 gFlex

Calculations of elastic plate flexure were conducted using gFlex (Wickert, 2016), an open-source Python based lithospheric flexure module following Kirchoff-Love thin plate theory based on van Wees and Cloetingh (1994). gFlex is a versatile program with the ability to calculate flexure for 1D (beam/transect) and 2D (plate/planform) models for elastic flexure from applied loads. gFlex can calculate flexure in several Python-based programs, such as Landlab and GRASS-GIS, as well as in stand-alone python scripts. This study uses the stand-alone Python script approach to running gFlex (Appendix A). gFlex calculates flexure for either numerical or analytical solution types.

3.2.2 Overview of Flexure in 1D

Drawing from the equations outlined in Section 3.1.2, a simple calculation in gFlex schematically demonstrates deflection in 1D. Lithospheric flexure calculations only consider the net change in loading over the analysed period, allowing for either inverse modelling (moving back in time) or forward modelling (moving forward in time) to be conducted. In addition, plate flexure is linear in the sense that loads can be applied incrementally and the resultant flexure calculated as the sum of the flexural increments. An equilibrium state refers to a fixed reference surface which in this study refers to the topography prior to loading. Inverse modelling starts with the final state and applies loads in a backward sense to reach the initial equilibrium state. Conversely, forward modelling starts with an initial equilibrium state and applies loads to reach the final equilibrium state. In the case of surface loading, both the stress (applied load) and strain (elastic flexure) will lead to changes in surface topography.

Two types of loading can affect the lithosphere through surface processes. Adding a load at the Earth's surface (positive loading) stresses the lithosphere by the addition of material, leading to deflection of the lithosphere toward the centre of the Earth (negative $d(x)$) and flexural subsidence near the load (Fig 3.3). Subsidence will be classified as negative deflection ($d(x)$). The negative peripheral flexure around the load constitutes the accommodation space created from subsidence (Fig 3.3). A well understood geologic example for flexural downwarping from

the addition of material is that of foreland basins, for example the Western Canada Sedimentary Basin (Tufano, 2016) and the eastern interior of North America (Beaumont et al., 1988).

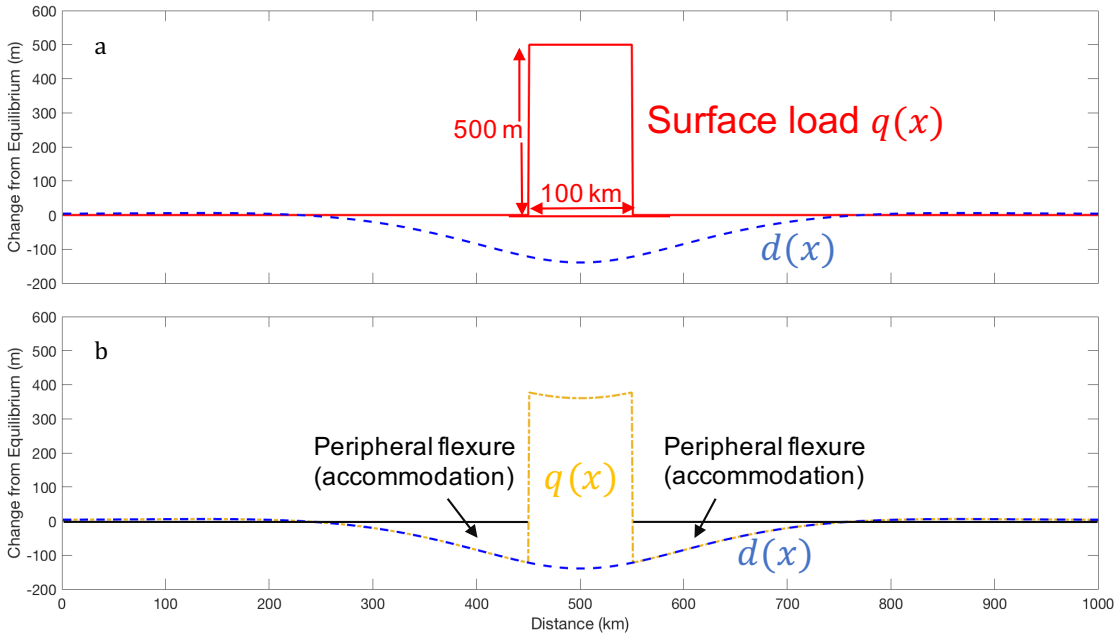

Figure 3.3 Forward model for the application of a positive surface load. (a) Plot of $q(x)$ (solid red line) (500 m x 100 km) and $d(x)$ (dashed blue line). (b) Plot of $d(x)$ (dashed blue line) and net change from equilibrium (stippled gold line). Run using periodic boundary conditions, $\rho_m = 3300\ kg/m^3$ (mantle density), $\rho_s = 2165\ kg/m^3$ (sediment density), $\rho_f = 0$ (density of infilling material).

Similarly, deflection from the removal of material at the surface (negative loading) can be calculated. Applying a negative load equivalent in magnitude to that from positive loading (Fig. 3.3 and 3.4) results in a mirrored upward deflection about equilibrium. Sediment backstripping follows the principle that a load of a given magnitude will have identical but mirrored flexural patterns in both forward models, adding material in sedimentary packages or water volumes to calculate subsidence generated from the loading of each layer, and from removing the sedimentary package or water and calculating uplift. For elastic modelling, net loading is the only stress on the lithosphere and the response to loading is considered to be instantaneous. Thus, the rate and timing of loading are irrelevant for calculating deflections. For example, to apply sediment backstripping where the thickness of a unit is known, only the flexure for the removal of the unit needs to be applied.

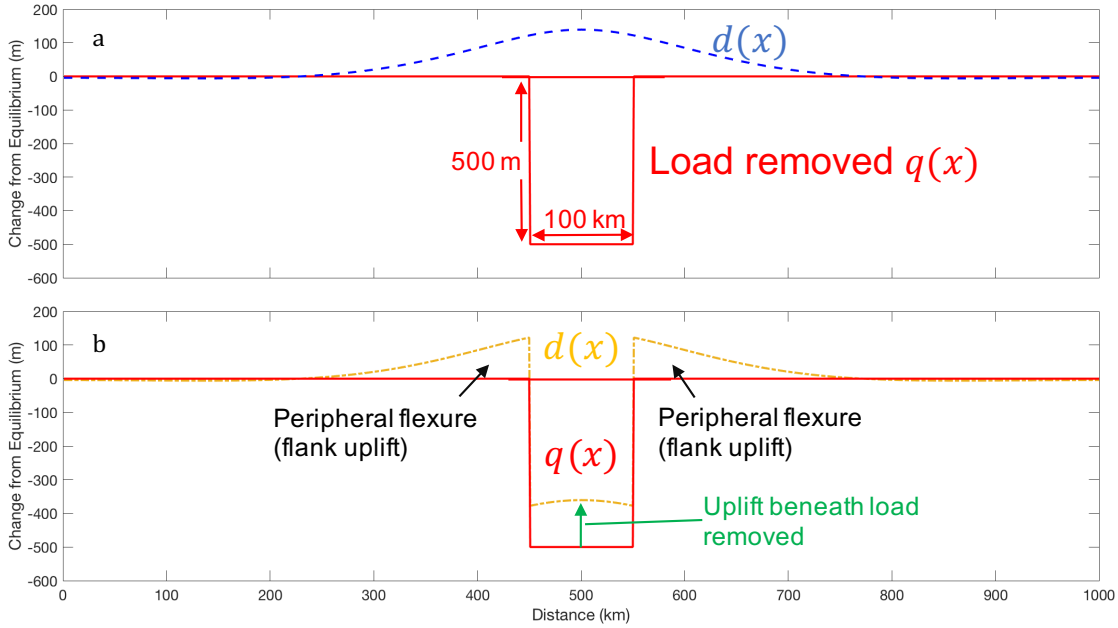

Figure 3.4 Forward model for the application of a negative surface load. (a) Plot of $q(x)$ (solid red line) (500 m x 100 km) and $d(x)$ (dashed blue line). Note the symmetry about 0 with respect Fig. 3.1(a). (b) Plot of q(x) (solid red line) and net change from equilibrium (stippled gold line). Run using periodic boundary conditions, $\rho_m = 3300\ kg/m^3$ (mantle density), $\rho_s = 2165\ kg/m^3$ (sediment density), $\rho_f = 0$ (density of infilling material).

One problem arises from calculating flexure from the basic applied load (force equal to channel mass of channel geometry) is the flexure beneath the base of the load (Fig. 3.3 and 3.4). Flexure beneath the load creates unrealistic geometries, such as concave down channel profiles (Fig. 3.4). Flexure can be viewed as linear in the sense that the solution can be taken as the sum of incremental flexural steps Iteratively adding flexural increments to the basic load will converge on a solution. Flexural increments are adjustments to the applied load to account for the flexure beneath the load. If not enough accommodation space or uplift is generated from the calculation for the basic load, then a further erosion or deposition is required to adjust the model. For example, increasing erosion in forward incision models accounts for the deflection in the channel in order to reach observed channel profiles in the model. However, the gFlex module cannot incorporate iterations directly into the module and therefore secondary python scripts were required to calculate the flexural increments/load adjustments (Appendix A). After approximately five iterations the model should converge on a solution.

3.3 Sensitivity Analyses

3.3.1 Varying elastic thickness

Several model sensitivities were considered in testing the hypotheses. Primary model sensitivity stems from the uncertainty in T_e, owing to a lack of information of lithospheric flexural properties under the Arctic region of interest. Variations in T_e will have substantial impacts on the regional elastic strength, and consequently a substantial effect on deflection ($d(x)$) (Fig. 3.5) (Eq.5). Increasing the elastic strength of the plate increases (increasing T_e) requires a greater bending moment ($M(x)$) is to bend the plate to an equivalent curvature (Eq. 6, §3.1.2). Lithospheric plates with a larger D under an identical stress will have a greater flexural wavelength (λ) (Eq. 10,11, §3.1.2) and shallower deflection ($d(x)$). As T_e approaches zero the deflection will approach local airy isostasy, where the plate is not strong enough to support the load and the load sinks into the plate. The load is directly exchanged with mantle material and the deflection geometry matches that of the initial loading.

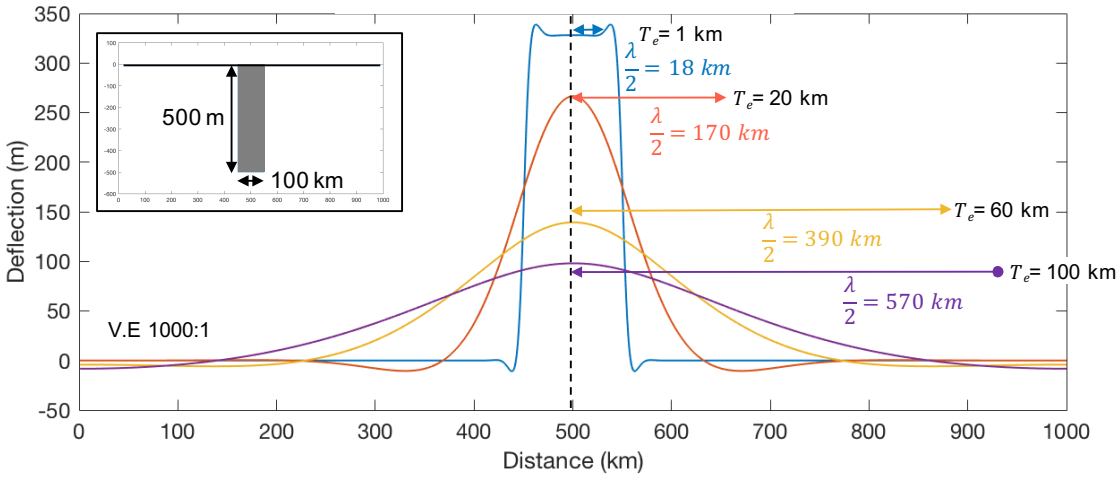

Figure 3.5: Deflection ($d(x)$) for varying T_e under a given negative load (inset above left, identical to Fig. 3.2, 500 m x 100 km). Run using a periodic boundary conditions, $\rho_m = 3300\ kg/m^3$ (mantle density), $\rho_s = 2165\ kg/m^3$ (sediment density), $\rho_f = 0$ (density of infilling material).

Globally, values for T_e range between 3 and 110 km (Burov, 2011). Understanding regional tectonics aids in understanding and estimating the regional elastic strength of the lithosphere. (Table 3.1).

Regional geophysical surveying would aid in quantitative analysis of T_e over the western Arctic. However, these surveys are difficult in the Arctic owing to logistical costs, sea ice, and permafrost. No prior geodynamical studies of the western Canadian Arctic exist with data suitable for use in this study. Geomorphic (raised beaches formed since deglaciation) and sedimentary markers (tilted beds or unconformities) can be used to quantify regional uplift and subsidence histories and estimate local T_e. Models were run for T_e of 30, 60 and 90 km to demonstrate the sensitivity of the output on regional T_e. A useful outcome of the numerical modeling in this thesis is a first order approximation of the regional T_e across the western Canadian Arctic. Further studies are required to improve the precision of regional T_e.

Table 3.1 T_e variations in North America

Region	Elastic thickness (T_e)
Basin and Range	1-20 km (Tesauro et al., 2012)
Canadian Cordillera	20-40 km (Fluck et al., 2003)
Canadian Shield	100 km (Fluck et al., 2003)
Arctic Canada	30 km (Burov, 2011)
Young oceanic lithosphere	0-20 km (Burov, 2011)
Old oceanic lithosphere	10-50 km (Burov, 2011)

3.3.2 Relationship between elastic thickness, flexural wavelength, and load width

The relationship between load width, T_e, and d(x) must be considered before running a model. Variations in net loading and the subsequent increases and decreases in deflection are easy to visualise, as larger applied loads will generate greater surface deflections. This is entirely dependent on the two factors, T_e (from the previous section) and loading geometry. Varying load width for a constant T_e will provide some insight into this relationship between the width of the load, flexural wavelength and T_e (Fig. 3.6). For flexure owing to narrow loads the deflection has the characteristic wavelength predicted by Kirchoff-Love thin plate theory. If load widths are taken drastically (10 times) larger than T_e, local airy isostasy will be seen, similar to decreasing T_e (in Fig. 3.5). These observations follow from the change in magnitude of loading in comparison with T_e, as increasing the magnitude of applied stress will create greater bending moments for the plate. For greater load widths, the wavelength is predicted by the convolution of the delta-function response (Green function).

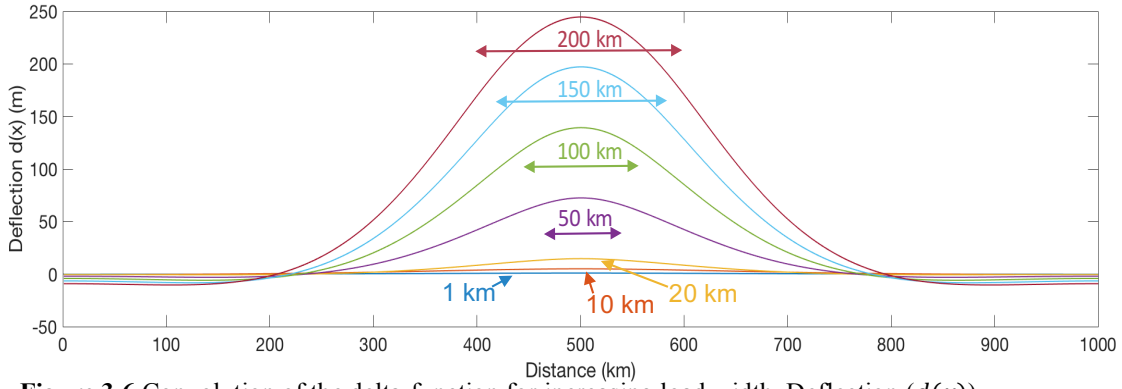

Figure 3.6 Convolution of the delta-function for increasing load width. Deflection ($d(x)$) calculations for varying load widths for constant T_e (100 km). All loads are rectangular and negative, schematically showing 500 m of sediment removal from surface for varying load widths from 1 km to 200 km. Colour coded arrows are load widths for the corresponding deflection pattern. Note decrease in amplitude of deflection (flattening of deflection $d(x)$) as load width approaches 0, as load width is sufficiently smaller than T_e. Contrary, as load width exceeds T_e, amplitude of deflection increases. Run using periodic boundary conditions, $\rho_m = 3300\ kg/m^3$ (mantle density), $\rho_s = 2165\ kg/m^3$ (sediment density), $\rho_f = 0$ (density of infilling material).

From analysis of the variations in T_e and loading width, models should be scalable based upon relationships among T_e, loading width and grid resolution. The scalable nature of the model is the result of the convolution of the delta-function. The grid resolution is the spacing between points in the model, i.e. raster cell size in 2D models. Smaller grid spacing will increase the model resolution. Sensitivity analyses in gFlex were carried out to identify any potential scaling issues by applying constant relationships for load width, T_e, and grid resolution to ensure expected deflection patterns arise (Appendix A). Results indicate there are no scaling issues in gFlex provided the grid resolution is sufficiently high.

3.3.3 Model boundary conditions

The gFlex module contains several model boundary conditions (Table 3.2). Each boundary condition used in gFlex is based on a physical interpretation of a geological environment. Choice of boundary condition can have a significant impact on flexure close to the boundary. There exists some sensitivity to the chosen model boundary conditions. Choice of boundary conditions may not exactly match the desired geologic environment, creating uncertainty near the model boundaries. However, taking model boundaries at distances much greater than flexural wavelengths from the applied loads minimizes the effect of the boundary condition becomes less significant. The approach here is to place the model boundaries at distances sufficiently far from

loads to minimize the uncertainty owing to choice of boundary condition. Boundary conditions used in this study are mirror and periodic.

Table 3.2 gFlex boundary conditions

Boundary Condition	Physical Interpretation
0Displacement0Slope	No displacement, clamped boundary
0Moment0Shear	Broken plate with a free (cantilever) end
0Slope0Shear	Free vertical displacement of a horizontally clamped boundary
Mirror	Mirror symmetry along boundary
Periodic	Infinite tiling of model domain (wrapping boundary)
NoOutsideLoads	Analytical solutions with uniform D

Periodic boundary conditions were used for the northern and southern boundaries to wrap model boundaries and limit deflection near the boundaries. A periodic boundary assumes the loads and deflection are periodic in nature and will periodically appear outside of the model. The east-west trending channels are periodic in nature and are assumed to continue near the northern and southern model boundaries. Mirror boundary conditions used for the eastern and western extents of the model provided symmetric boundaries. Symmetric boundaries allow for the model area to be decreased (faster computation) while not significantly effecting the flexure for loading near the boundary.

3.4 Similar lithospheric flexure models

3.4.1 Greenland Fjords

Greenland and Norwegian margins exhibit large fjords from glacial deepening of fluvial incised valleys (Medvedev et al., 2008). Coastal margins in the south-east of Greenland display tectonic-scale uplift (~ 2 km), while a central depression is covered by a thick continental ice sheet which occupies central Greenland (Medvedev et al., 2013). Mesozoic marine sediments at elevations 2 km above modern sea-level suggest significant rock uplift along the passive margin since the Mesozoic (Medvedev et al., 2008). Japsen et al. (2006) suggested three stages of Cenozoic uplift along the Greenland margins from apatite-fission track dating. The first uplift event (60 Ma) relates to rift-flank uplift from nearby rifting and seafloor spreading during the opening of the Atlantic Ocean. The second uplift event (30-36 Ma) post-dates rifting by 30 Ma and is likely related to the Iceland hotspot track (Japsen and Chalmers, 2000; Medvedev et al.,

2013). The last uplift events (7 Ma) correspond to the initiation of glaciation on Greenland. There is continued debate over the interpretations of Japsen et al. (2006). To resolve the debate, recent geodynamical studies tested whether uplift along the southeastern margins can be explained by incision of the fjords along the margins (Medvedev et al., 2008; Medvedev et al., 2013).

Their approach accounts for flexure from continental ice sheet loading, unloading during incision of fjords, and sediment loading offshore. They developed a finite-element-based software called Proshell (in MATLAB) to construct elastic deformation models using shell-theory (elastic flexure without the flat earth assumption) and used inverse models to refill the glacially eroded fjords with sediment from offshore. Applying an iterative solution, the model converges on pre-erosional topography. Iterations account for subsidence owing to flexure from loading material back into the fjords, converging on a paleosurface after several infilling steps. In addition to the flexural isostasy modelling from incision of the fjords, flexure owing to continental ice-sheet loading was considered. Models were calculated using low T_e, typically less than 30 km. Model resolution is 1-1.5 km from DEM's (digital elevation models).

Their model results show up to 1.2 km of uplift can be attributed to flexural isostasy in regions of Greenland (Fig. 3.7). This, however, cannot completely explain the 2 km elevations of Mesozoic marine sediments above modern sea-level and suggests multiple processes contributing to uplift, including thermal and isostatic causes of rift flank uplift. Results indicate ice loading has driven up to 850 m of subsidence in central Greenland. However, peripheral bulge effects from ice loading are negligible along the margins of Greenland. Medvedev et al. (2013) also considered that emplacement of Paleogene basaltic dykes may have caused several hundred meters of local uplift (i.e. the second stage of uplift outlined by Japsen et al. (2006)). Moucha et al. (2008) and Pedersen et al. (2016) suggest that Neogene dynamic topography may have contributed several hundred metres more of uplift along the North Atlantic margins. The additional uplift may account for the several hundred metres of additional uplift estimated along the southeastern margins of Greenland (Medvedev et al., 2013)

A similar method will be applied in the two modelling projects in this study. However, the volume of sediment removed from the channels and the volume of Pleistocene sediment offshore are unknown for the western Canadian Arctic. Therefore, modelling in this study will consist of

forward models for incision from an estimated initial paleosurface rather than inverse modelling for the addition of material back into the channels to estimate an initial paleosurface.

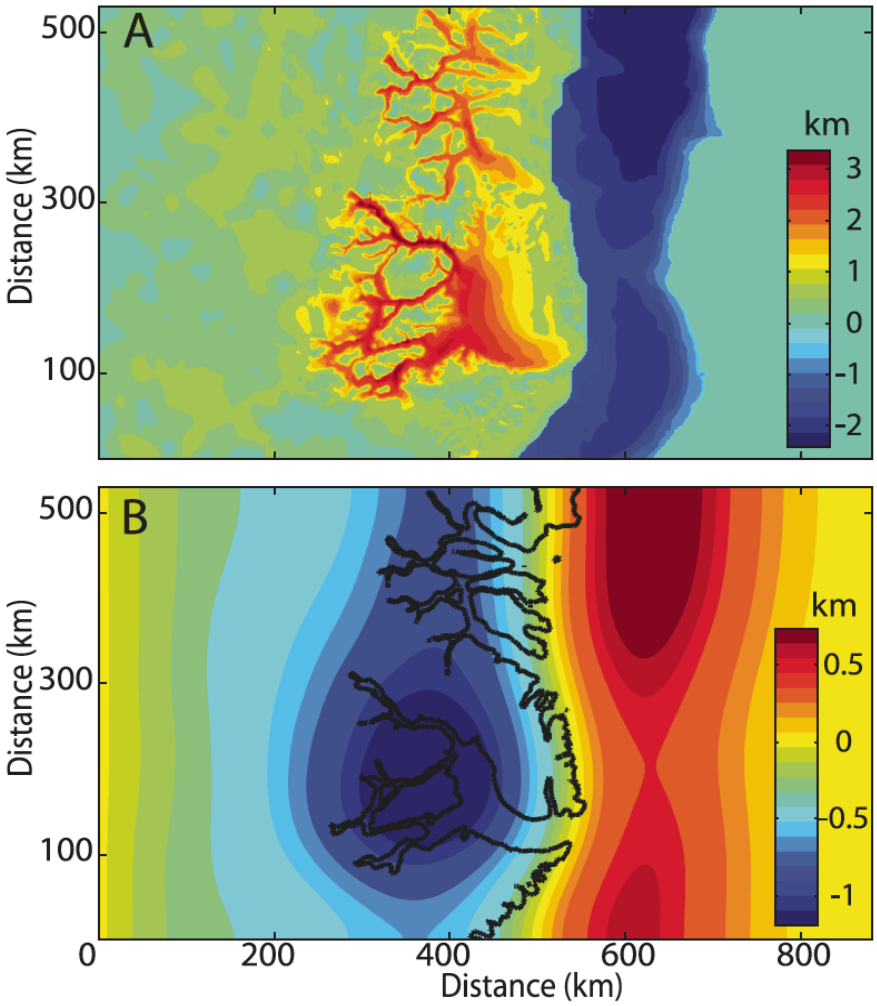

Figure 3.7 Results of Medvedev et al. (2008) for flexural calculations on the eastern margin of Greenland. (A) Raster image displaying the thickness of material removed (negative) and added (positive) along the southeastern Greenland margin. (B) Lithospheric deflection induced from restoring material back into fjords. Figure from Medvedev et al. (2008).

3.4.2 Colorado Plateau

Early studies have concluded that the Grand Canyon and deep canyons of the Colorado Plateau are a consequence of mostly non-tectonic incision dating back 30-70 Ma (Lazear et al., 2013). New models and geologic constraints suggest otherwise, with incision concentrated in the last 6-10 Ma (Karlstrom et al., 2008; Lazear et al., 2013; Moucha et al., 2009; Pederson et al., 2002; Roberts et al., 2012; Roy et al., 2009). Three Cenozoic exhumation events of the Colorado Plateau are postulated: 1) late-Cretaceous, 2) mid-Cenozoic, and 3) Neogene-present (last 10

Ma) (Lazear et al., 2013). Lazear et al. (2013) have refocused previous models for the uplift of the Colorado Plateau to Neogene flexural uplift while incorporating surrounding tectonic environments such as the Basin and Range to the west. Their study focused on reconstructing a 10 Ma paleosurface for the Colorado Plateau from differential uplift rates of the Colorado Plateau. Thermal modelling errors related to volcanogenic heat flow and perturbations from assumed topography were difficult to evaluate in their model and pose a significant uncertainty in their results.

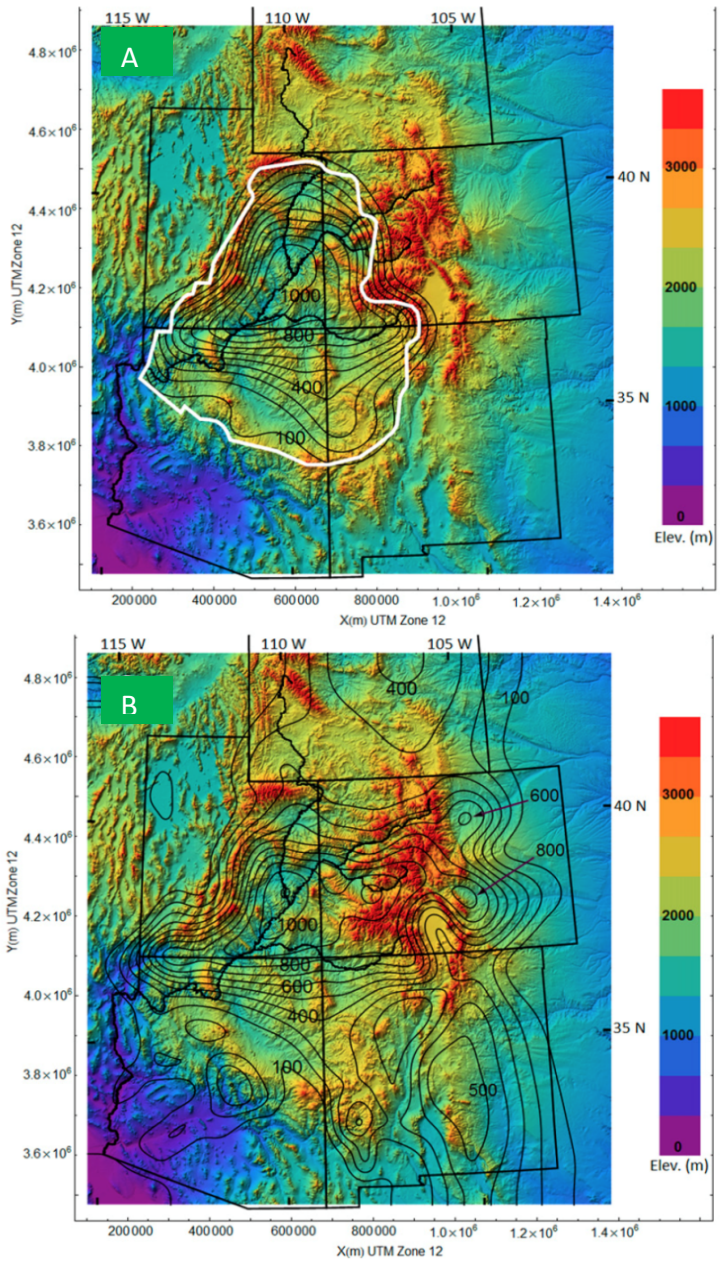

Figure 3.8 Model results for erosional isostasy calculations for the Colorado Plateau with variable T_e. (A) Uplift generated from limiting model to the Colorado Plateau. Isostatic adjustment forms bullseye pattern within the restricted model. (B) Unrestricted model, incorporating surrounding tectonic environments and landscape evolution into model. Figure from Lazear et al. (2013).

Thermochronological data constrain models used to reconstruct the 10 Ma paleosurface. Thermochronological data include apatite fission track and apatite U-Th/He (AHe). In addition to thermochronological data, inverted topography from 8-12 Ma basalt flows that preserved erosional features in the landscape were estimated. Constraints are used to estimate 13 subregions within the Colorado Plateau and surrounding areas. Differential erosion and rock uplift are calculated from control points in differing subregions and applied to the broader region, inclusive of the Colorado Plateau, southern Rocky Mountains and eastern Basin and Range. The 10 Ma paleosurfaces constructed for each subregion were compiled to create a regional 10 Ma paleosurface.

Control points had an irregular distribution so a triangular network with linear interpolation spanned the region. A 2D Gaussian filter of 1σ radius aesthetically smoothed the estimated 10 Ma paleosurface. An estimate of net eroded thickness was obtained from the difference between modern topography and the estimated paleosurface. Some models incorporated a variable elastic thickness (Lowry et al., 2000) and net eroded thickness applied as a lithospheric load. Findings suggest up to 1 km of exhumation from erosion in the Colorado Plateau, concentrated around the upper Colorado River (Fig. 3.8). Results compared to previous studies suggest incision of the Colorado River has predominantly occurred since 6 Ma, contradicting the long-held idea of passive incision over a much longer period.

The study of the western Canadian Arctic also requires the reconstruction of a paleosurface for the Pliocene. However, no such thermochronologic data are available for the western Canadian Arctic to estimate paleosurfaces. The incision of the Grand Canyon resembles that of the Arctic channels. Widespread Cenozoic basalt flows on the Colorado Plateau suggest a Cenozoic paleotopography with little relief. The western Arctic landscape prior to incision likely constituted a coastal plain with little topographic relief, similar to much of the Colorado Plateau and Greenland margins.

Chapter 4 Modelling Results

The following sections outline the specific methods, results, and uncertainties in the modelling experiments. Modelling was split into two projects. Project 1 (section 4.1) involved modelling the amount of flexural subsidence from Pliocene-Pleistocene sediment loading offshore. Project 2 (section 4.2 and 4.3) models the isostatic response in the western Canadian Arctic from incision of the Arctic channels. The primary focus for modelling is in the area of Banks Island and Prince Patrick Island. Most of the model constraints and sedimentological studies into landscape evolution of the western Arctic Pliocene coastal plain come from Banks Island, Prince Patrick Island, and the neighbouring Canada Basin (Fig. 4.1).

4.1 Project 1: Sediment loading models

4.1.1 Approach to sediment loading modelling

Project 1 consisted of modelling lithospheric flexure caused by late-Cenozoic sediment loading along the western Canadian Arctic passive margin (Fig. 4.1). The sediment loading models required backstripping of late-Cenozoic sedimentary units. Sediment backstripping is the process in which sedimentary packages are sequentially removed (backward in time) to calculate flexural uplift (Fig. 4.2). Sediment backstripping follows from the symmetrical nature of lithospheric flexure from equal negative and positive loading about equilibrium (zero deflection).

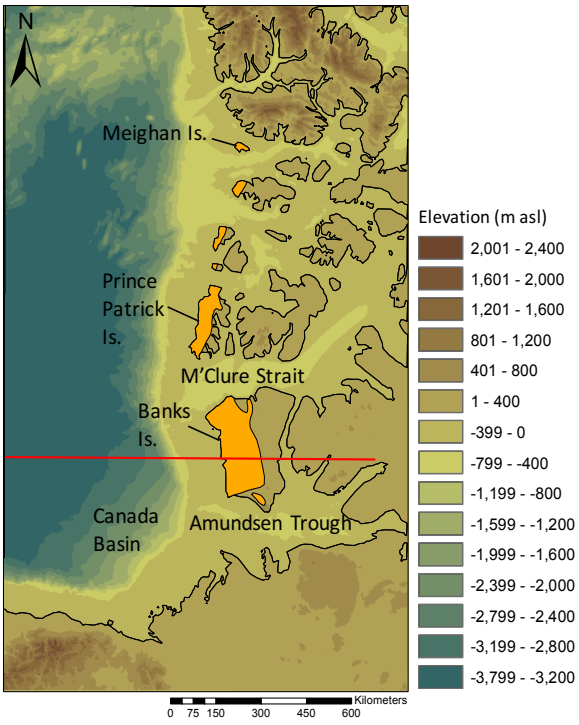

Figure 4.1 Area of interest for sediment loading modelling. East-west transect through Banks Island for 1D model is outlined in red. Elevation is measured in metres above modern mean sea level (m asl).

The onshore and offshore Pliocene and Pleistocene deposits form the upper fraction of a clastic continental terrace wedge along the western passive margin of the western Canadian Arctic. The Holocene sediments are relatively thin and were deposited after incision of the Northwest Passages. Thus, the Pliocene and Pleistocene units are the focus in both projects. Project 1 determined: a) the degree of tilting by lithospheric flexure that should be recognized in future field visits to the remote islands (as exemplified by dipping peat at the Ballast Brook locality on Banks Island), and b) the width and thickness of subaerially exposed Beaufort Formation (BF) as a consequence of accommodation space created owing to loading. On a larger scale, sediment loading modelling was carried out to gain a first-order approximation for late-Cenozoic flexural subsidence and its implications on landscape evolution of the western Canadian Arctic. Based on field observations and existing mapping (Chapter 2) the two hypotheses tested in Project 1 are:

Hypothesis 1a: The orientation, width, and thickness of the currently exposed BF is consistent with the geometry and orientation of the accommodation space generated by loading.

Hypothesis 1b: The tilt of an originally horizontal Miocene peat bed should be basinward and equal or greater than that predicted by loading by the Pliocene and Pleistocene sediments. The tilt of the peat may be greater than that predicted in the models owing to additional tilting from other processes, such as faulting.

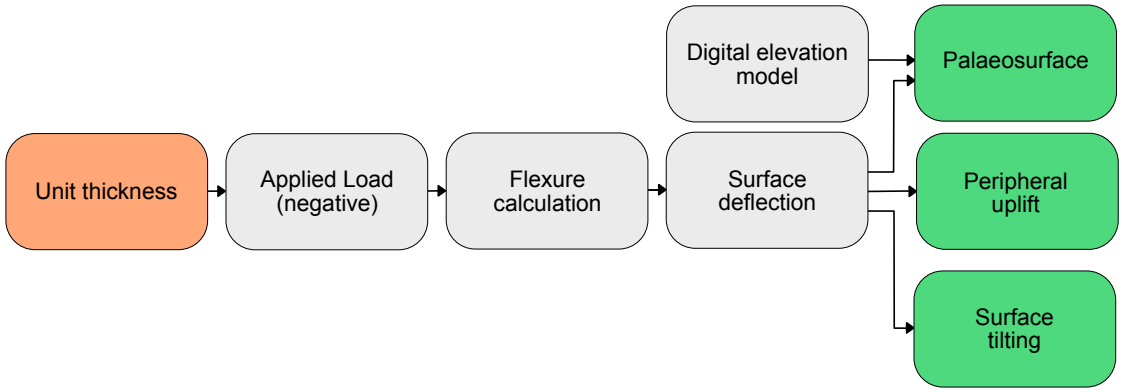

Figure 4.2 Flowchart for sediment backstripping applied to test flexural subsidence from sediment loading. The orange box highlights the input and the green boxes highlight the outputs.

The base map for the sediment loading models is a rotated version of the IBCAO Version 2.23, 2 km grid resolution digital elevation model (DEM). Its projection is WGS 84 polar stereographic with true scale at 75°N and it uses modern mean sea level for the vertical datum (Jakobsson et al., 2008) (Fig. 4.1). The initial raster (dot matrix composed of rectangular gridded

point values) was rotated in ArcMap using a bilinear interpolation. The rotation of the map allowed for the east and west boundaries to be along strike of the coast and to orient north to the top of the map. Additionally, the rotation of the map allowed for a raster (now clipped square) to be converted to text file arrays relatively simply. Calculations were completed in gFlex for the flexural uplift from the removal (negative loading) of the units of interest for various T_e (30, 60, 90 km and a west-to-east linearly increasing T_e through the continental shelf). Creation of the varying T_e model tested the possible effects of a decrease in T_e moving toward the rifted margin. Furthermore, the converse calculation for flexural subsidence from the positive loading was calculated in gFlex. Table 4.1 outlines the values for parameters used in the sediment loading models.

Table 4.1 Sediment loading model parameters

Parameter	Value/Condition
Gravity constant (g)	9.81 m/s^2
Young's Modulus (E)	65 x 10^9 GPa
Poisson's Ratio (ν)	0.27
Mantle density (ρ_m)	3300 kg/m^3
Sediment density (ρ_s)	2300 kg/m^3
Water density (ρ_w)	1000 kg/m^3
Elastic thickness (T_e)	30, 60, 90 km and variable (25-60 km)
Horizontal grid spacing (dx)	2 km
Vertical grid spacing (dy)	2 km
North boundary condition	Periodic
South boundary condition	Periodic
West boundary condition	Mirror
East boundary condition	Mirror

Seismic data (pre-stack depth migrated (PSDM) BasinSPAN^{TM} seismic courtesy GX Technology Corporation) held by the Geological Survey of Canada (GSC-Calgary) were used to estimate thicknesses for the Pliocene and Pleistocene sedimentary packages offshore Banks Island (Appendix B). The marine seismic profile data available did not provide full volumes for the wedge sediments along the margin and therefore required extrapolation. A cross-section

through the data (perpendicular to the strike of the coast) (Fig. 4.1) outlines the areas where the data needed to be extrapolated (Appendix B). Subtracting the thicknesses from the modern seafloor (in ArcMap) provided depths to the base of the Pliocene and Pleistocene. Cubic functions were applied to the ends of the available data to taper out the units based on the seismic lines in Helwig et al. (2011) and to follow a typical clinoform geometry. Thus, the thicknesses of the units are only estimates at this time owing to partial coverage of the units in available seismic data.

Using the extrapolated thicknesses from the transect through Banks Island (Fig. 4.1), sediment backstripping techniques (Fig. 4.2) were applied to construct 1D models for the flexural uplift from the removal of the two units of interest. Sediment was assumed to be primarily deposited below sea level and therefore only displacing water. Multiplying the unit thickness by the density (ρ_L) and the gravity constant ($g = 9.81$ m/s^2) converts the thickness to an applied (negative) load. Under the assumption sediment only displaces water, the net density of the applied load is the difference between the density of the sediment ($\rho_s = 2300$ kg/m^3) and the density of sea-water ($\rho_w = 1000$ kg/m^3) ($\rho_L = 1300$ kg/m^3). Sediment density in the model is from educated guesses of the density of the units. There exist some uncertainties in the density for the units of interest and any variations with depth. The significance of these uncertainties will be discussed in section 4.1.3.

Extrapolation of the Pliocene and Pleistocene units along strike of the continental shelf break allowed for the expansion of the 1D models into 2D. The continental shelf break appeared to be the most accurate marker for maintaining unit thickness along the continental margin. Extrapolation using isopachs (thickness contours) constructed perpendicular to the east-west transect through Banks Island and along strike of the continental shelf break allowed for expansion of the thickness (1D) into a volume (2D). Increasing the isopach resolution decreased the uncertainty in the isopach surfaces and sediment volume. The isopachs formed a thickness surface (converted in ArcMap) and provided an estimated volume of sediment for each unit.

Conversion of the isopach surfaces to an applied load utilized the same techniques as for the transect model above under the assumption water replaced all sediment removed ($\rho_L = 1300$ kg/m^3). gFlex was used to calculate the flexural uplift from the removal (negative loading) of the units of interest (section 4.1.2). Summing the flexural uplift from sediment removed (negative

loading) in the late-Cenozoic estimated the net flexural subsidence over the region and provided some indication for landscape evolution along the western Canadian Arctic margin.

4.1.2 Results of sediment loading modelling

Sediment loading modelling included 1D and 2D models from sediment backstripping (Fig. 4.2) of the Pleistocene and Pliocene units along the western Arctic passive margin. 1D model calculations for sediment loading vary for T_e of 30, 60, 90 km, as well for a linearly variable T_e (Fig. 4.3 (d) and 4.4 (d)). Varying the T_e over the region tested if there is a difference in the results from a weaker oceanic lithosphere ($T_e = 25$ km) compared to continental ($T_e = 60$ km).

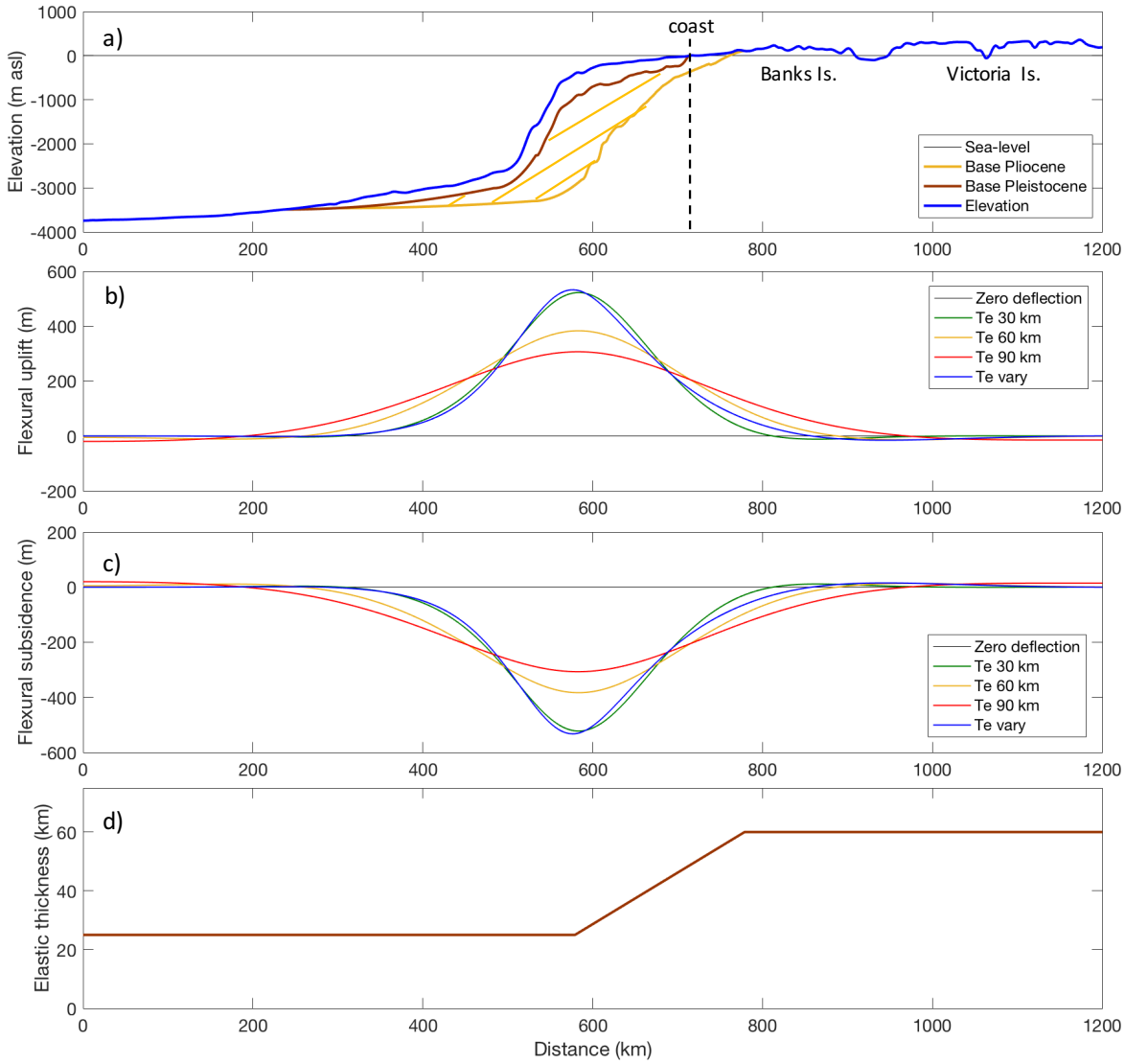

Figure 4.3 1D sediment backstripping for Pliocene sedimentary package offshore of Banks Island (Fig. 4.1). a) cross-section for the late-Cenozoic sedimentary packages offshore (Pliocene and Pleistocene) with the Pliocene unit marked by banded pattern. b) The flexural uplift calculated from the removal of the Pliocene unit for various T_e. c) The flexural subsidence calculated for the addition of the Pliocene unit for various T_e. d) Spatially variable elastic thickness used in variable T_e In b) and c). Model parameters can be found in Table 4.1.

The thickness of the Pleistocene unit offshore reaches a maximum of approximately 750 m (Fig. 4.3 (a)), tapering out laterally to the east and west. Similarly, the Pliocene sedimentary package has a maximum thickness of 2000 m, tapering out laterally to the east and west (Fig. 4.4(a)). Flexural uplift was calculated in gFlex for the removal of the Pliocene and Pleistocene (negative loading, positive deflection) (Fig. 4.3 (b) and 4.4 (b)). Conversely, adding the Pliocene and Pleistocene units in gFlex calculated the flexural subsidence from deposition of the units

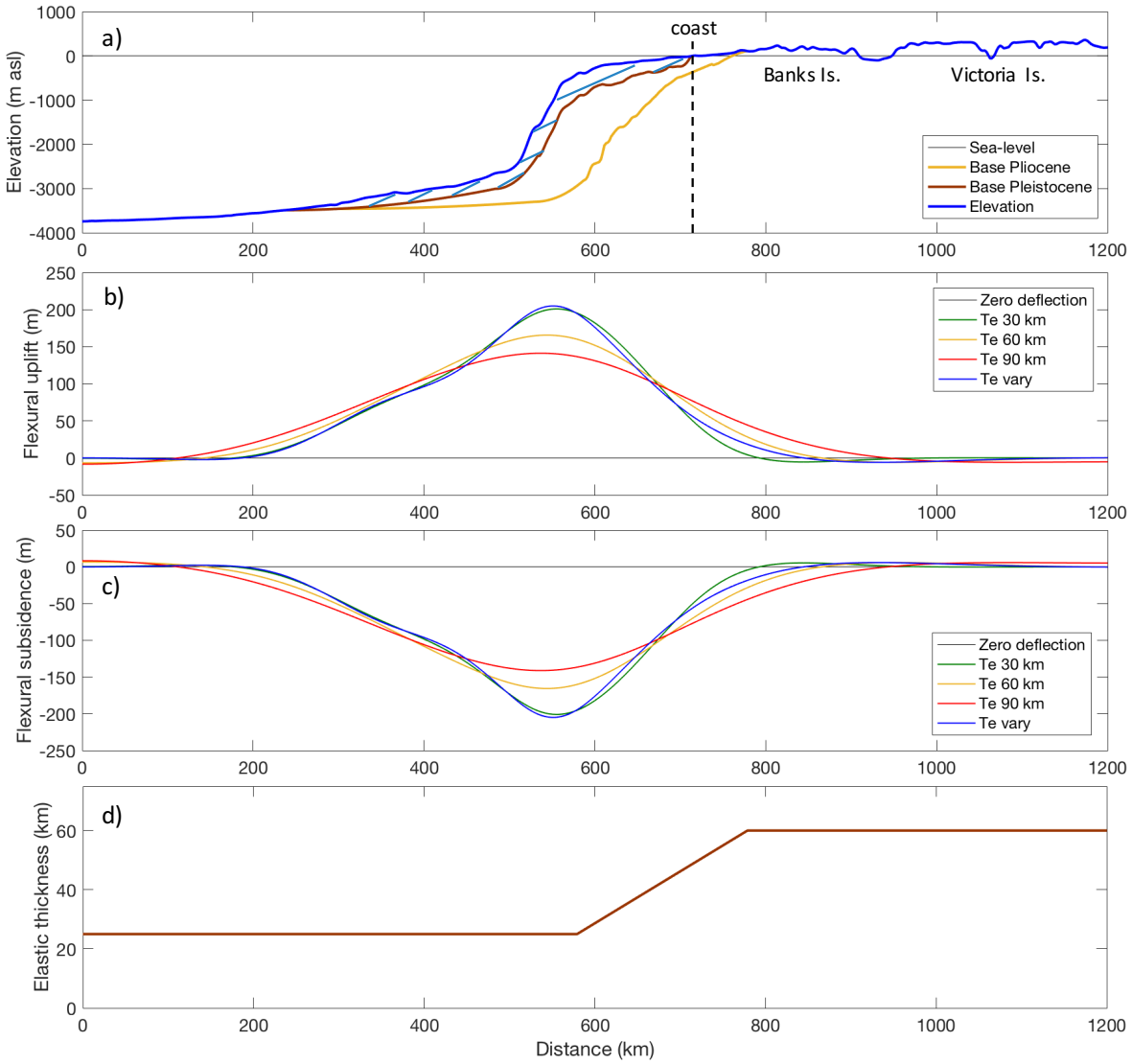

Figure 4.4 1D sediment backstripping for Pleistocene sedimentary package offshore of Banks Island (Fig. 4.1). a) cross-section for the late-Cenozoic sedimentary packages offshore (Pliocene and Pleistocene) with the Pleistocene unit marked by banded pattern. b) The flexural uplift calculated from the removal of the Pleistocene unit for various T_e. c) The flexural subsidence calculated for the addition of the Pleistocene unit for various T_e. d) Spatially variable elastic thickness used in variable T_e In b) and c). Model parameters can be found in Table 4.1.

(positive loading, negative deflection) (Fig. 4.3 (c) and 4.4 (c)). The results of the removal and addition of the units are expected to be symmetric about the equilibrium (zero deflection). The results are symmetrical about the equilibrium (Fig. 4.3 (b) and (c), 4.4 (b) and (c)). The maximum deflection from the removal of the Pliocene unit ranges from approximately 300-550 m (Fig. 4.3 (b) and (c)). Maximum deflection from the removal of the Pleistocene unit ranges from approximately 120-250 m (Fig. 4.4 (b) and (c)). The models predict a substantially larger

degree of deflection for the Pliocene unit, an expected result given the substantially greater thickness of the unit.

The 2D models also showed a regional flexural subsidence from the deposition of the units of interest. 2D models were run with T_e of 30, 60 and 90 km. No substantial difference was observed between the deflection ($d(x)$) for the variable T_e and the 30 km T_e. Therefore, a variable T_e was not analyzed in the 2D models. The 2D models predict the flexural uplift from the removal of the offshore Pliocene and Pleistocene units (Fig. 4.5 and 4.6 respectively). The 2D models therefore can be used to predict the flexural subsidence from the loading of the units because the deflection patterns for flexural uplift and subsidence form symmetric curves about equilibrium. The regional late-Cenozoic flexural net flexural subsidence for each T_e (Fig. 4.7) is the net change in the system over the time frame analysed (early-Pliocene to recent). Further analysis of the net change of the system aided in understanding the landscape evolution in the late-Cenozoic.

The thickness of the BF has a high variability near the modern Arctic coast. Fyles (1990) suggests from seismic analysis that the thickness of the BF along the coast of Prince Patrick Island reaches upwards of 1000 m and on average is 600 m near the coast. The accommodation space predicted along the modern Arctic coast from peripheral flexure owing to Pliocene sediment loading offshore is 200-250m. The ION-GXT seismic data provides an estimated thickness of 400 m for the Pliocene unit near the coast of Banks Island (Fig. 4.8). The values observed for the thickness of the Pliocene unit near the coast are greater than the accommodation space generated from Pliocene sediment loading offshore.

Models predict peripheral uplift east of the loading (past $x = x_\alpha$ where $d(x) = 0$) is small (up to 20 m) but not small enough to be negligible in analysis of landscape evolution. The peripheral uplift extends over 200-300 km inland and therefore gradients produced from peripheral uplift are very shallow but still sufficient enough to change drainage patterns.

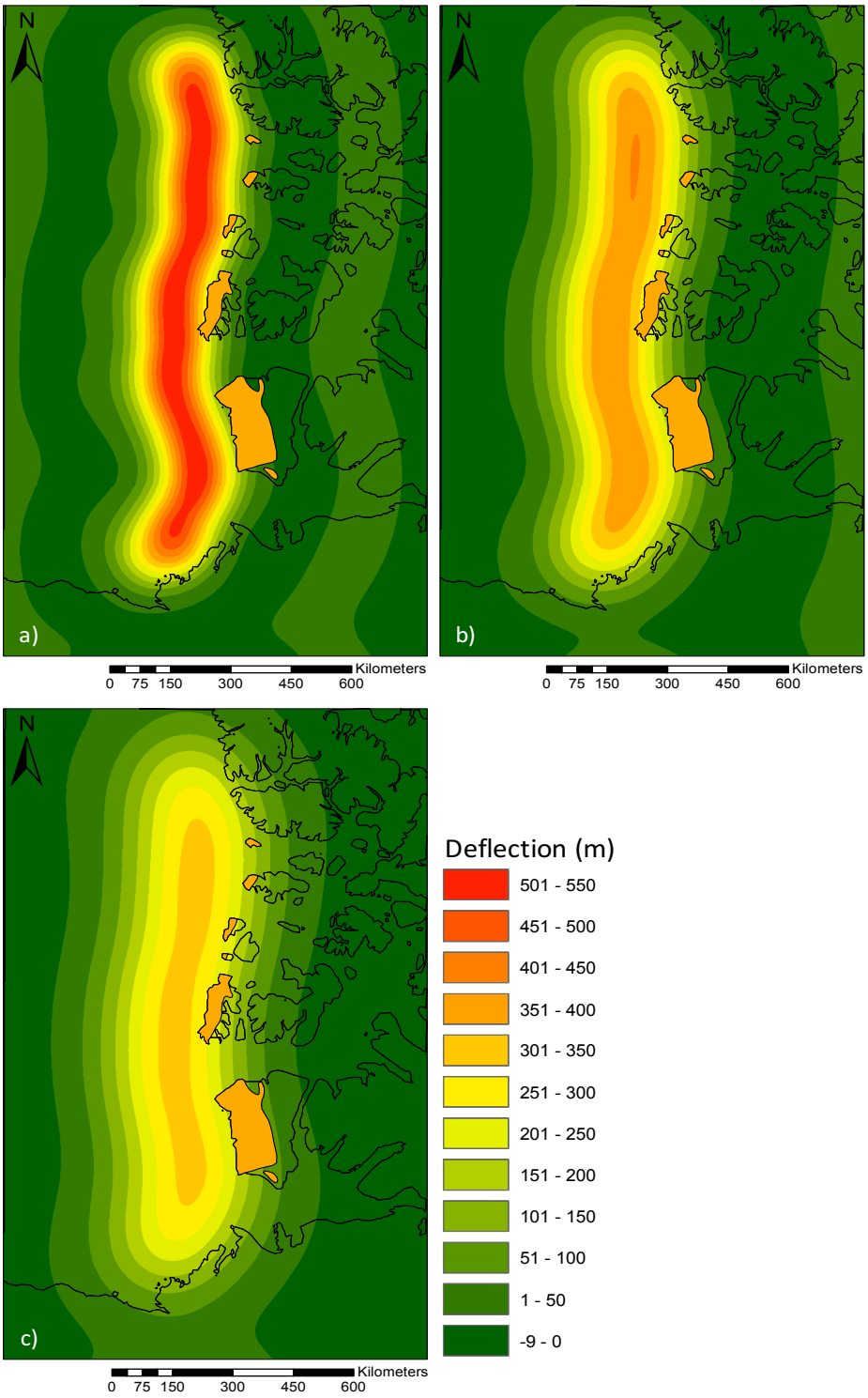

Figure 4.5 Calculated flexural uplift (deflection, $d(x)$) from the backstripping (removal) of the Pliocene unit for T_e a) 30 km, b) 60 km, and c) 90 km. The black lines outline the modern shoreline. The BF outcrops are outlined by the opaque orange polygons. Model parameters can be found in Table 4.1.

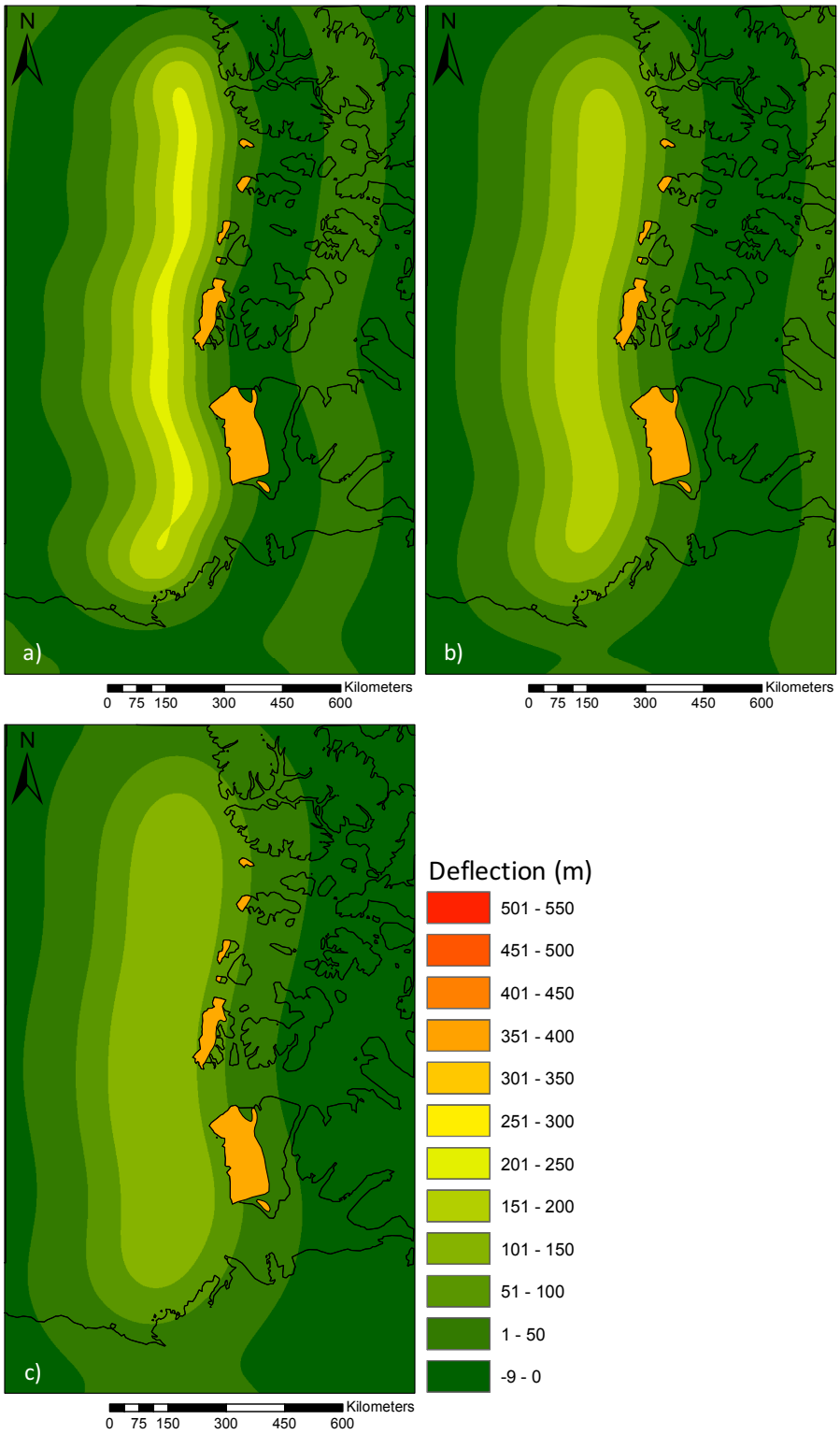

Figure 4.6 Calculated flexural uplift (deflection, $d(x)$) from the backstripping (removal) of the Pleistocene unit for T_e a) 30 km, b) 60 km, and c) 90 km. The black lines outline the modern shoreline. The BF outcrops are outlined by the opaque orange polygons. Model parameters can be found in Table 4.1.

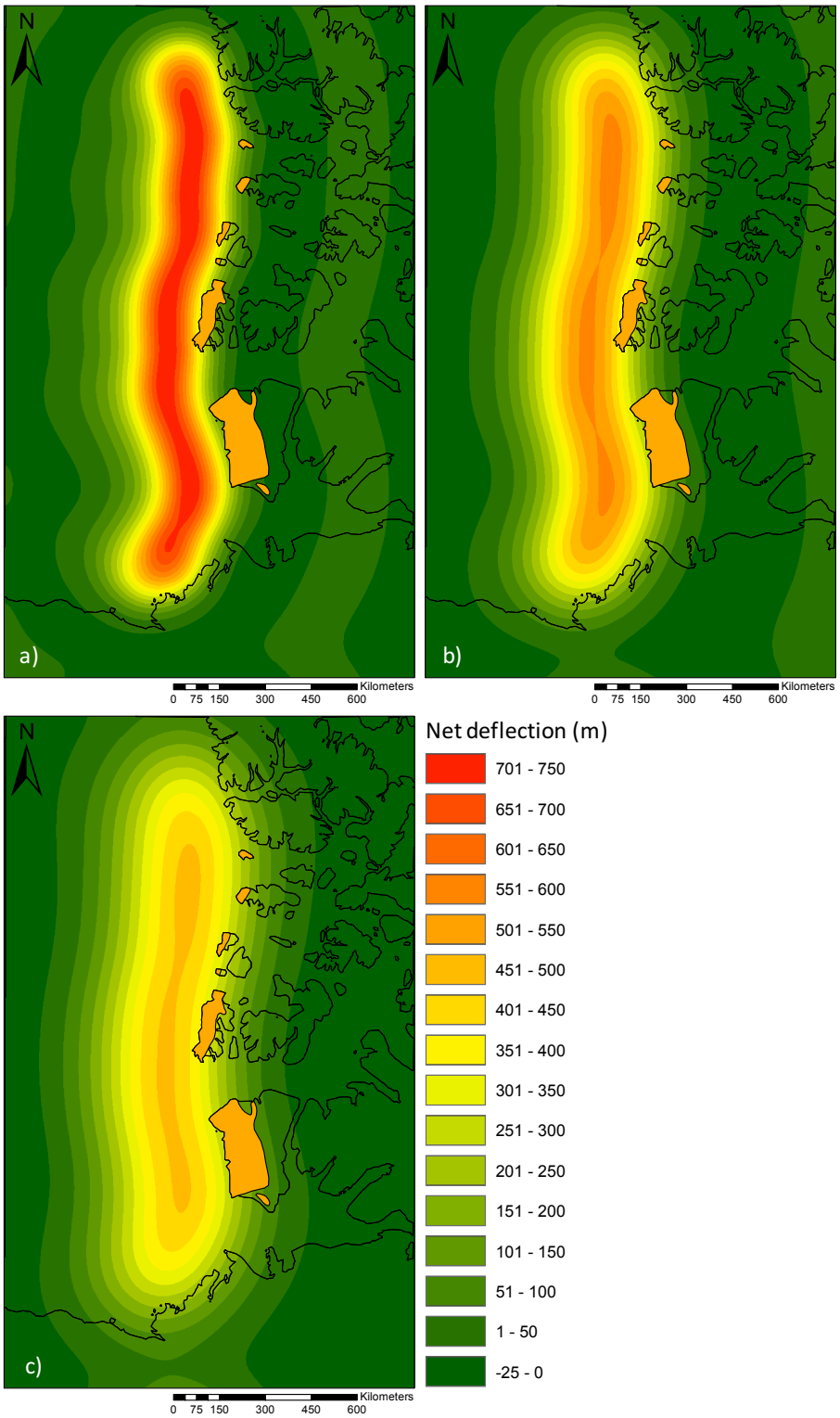

Figure 4.7 Net late-Cenozoic deflection (calculated uplift from sediment backstripping) for a) 30 km, b) 60 km, and c) 90 km T_e. The black lines outline the modern shoreline. The BF outcrops are outlined by the opaque orange polygons. Model parameters can be found in Table 4.1.

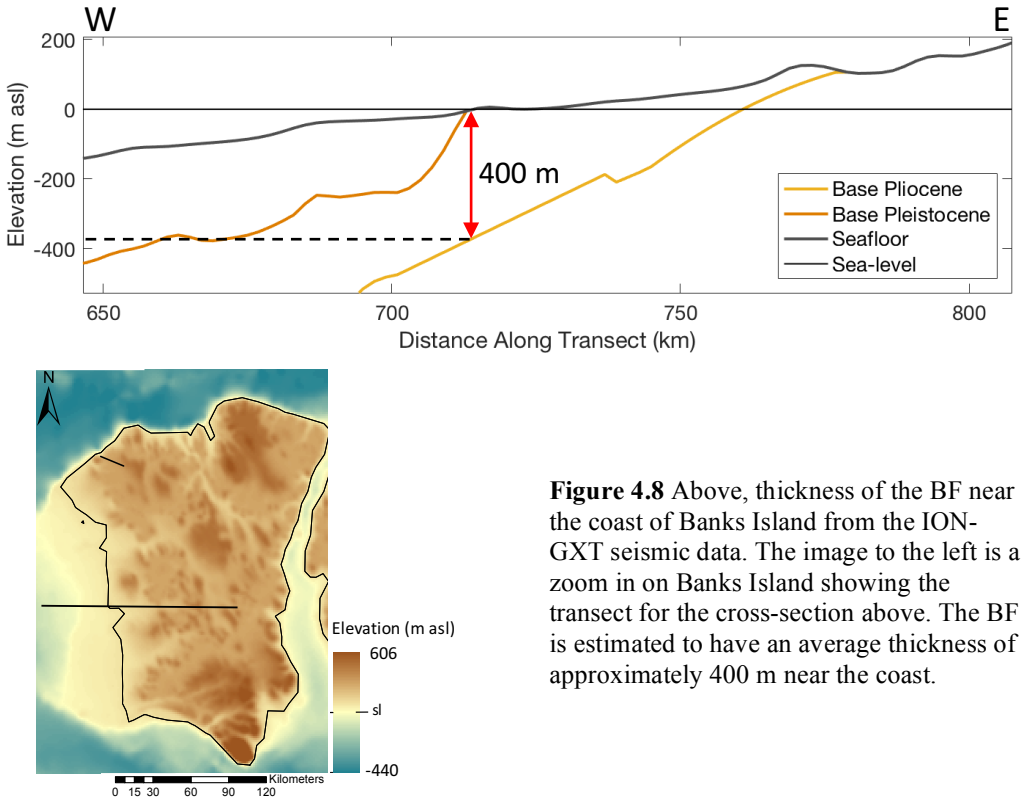

Figure 4.8 Above, thickness of the BF near the coast of Banks Island from the ION-GXT seismic data. The image to the left is a zoom in on Banks Island showing the transect for the cross-section above. The BF is estimated to have an average thickness of approximately 400 m near the coast.

The average observed tilt of the Miocene peat layer at Ballast Brook is 6.4 m/km (Fyles et al., 1994). Taking a cross-section of the net subsidence models for T_e of 30, 60 and 90 km through Ballast Brook provides an estimate for the tilting of the peat layer owing to flexural subsidence from sediment loading (Fig. 4.9). The cross-section through Ballast Brook is a small segment (~30 km) of the (net) deflection curves ($d(x)$) (~600 km wide). Deflection (~100's m) is also substantially less than the flexural wavelengths (~100's km) and therefore the flexure at Ballast Brook will appear as a linear function compared to the much greater regional damped sinusoidal flexure pattern. A linear regression (least squares best fit) for each small section of the deflection curves provided an estimation for the tilt generated in the Ballast Brook region from flexural downwarping during deposition. Tilting from flexural downwarping varies from 2.7-3.7 m/km (Fig. 4.9), half of the observed tilt of the peat at Ballast Brook.

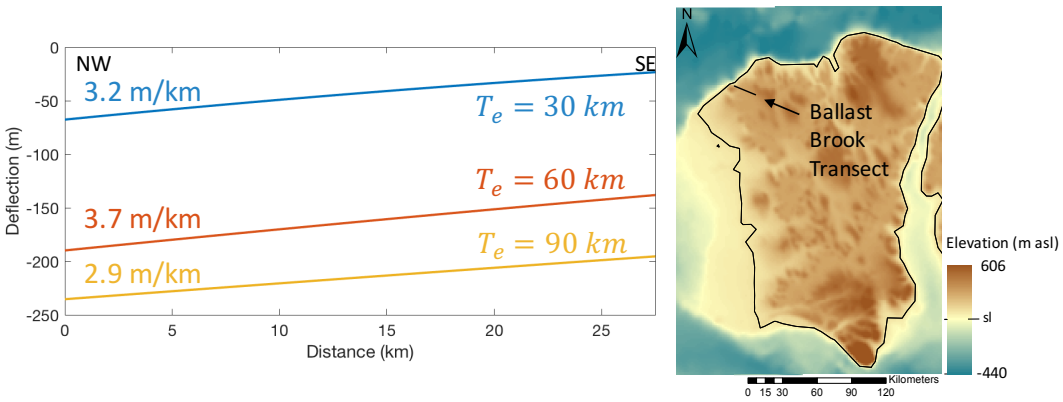

Figure 4.9 Flexural downwarping at Ballast Brook from net subsidence estimates (Fig. 4.7). Calculated gradients from linear regression for each model are shown on the left of the image. Right is a digital elevation model for Banks Island with transect through Ballast Brook (black line in the NW of Banks Island).

4.1.3 Uncertainty in sediment loading modelling

The largest degree of uncertainty in flexure calculations for sediment loading is from the estimations for the thickness of the Pliocene and Pleistocene sediment packages offshore. Precise calculations for flexure of Arctic lithosphere owing to late-Cenozoic sediment loading are not possible at this time without more complete interpretations of the seismic data. Predictions for flexural subsidence are likely within 100 m of the true deflection as models do incorporate the maximum thickness of each unit.

The amount of subsidence prior to the deposition of the Beaufort Formation is considered negligible. This may be not true. The ages of the Beaufort Formation and underlying Ballast Brook formation are still uncertain. If the time represented by the regression associated with the Miocene unconformity is short, then more accommodation space may have been available for the BF than calculated with loading from the Pliocene and Pleistocene units.

Some uncertainty exists in the chosen sediment density (ρ_s). It is difficult to precisely determine the variability in density in these units without values for parameters such as porosity and compaction. The assumed sediment density (2300 kg/m^3) reflects an estimated average for porous quartz-rich marine sands. Some error is caused by the invalid assumption that water is replaced by sediment in the subaerially exposed portions of the Pliocene sedimentary package (BF). Over the timeframe of the study (early-Pliocene to recent) the subaerially exposed Pliocene sediments have not displaced water. Therefore, the true density of material removed near the coast is greater than that offshore. However, the subaerially exposed sediment comprises a tiny

fraction of the total volume of onshore and offshore Pliocene sediment. Any increase in deflection generated by adjusting for this systematic error in density would be insignificant compared to the regional deflection pattern. Load densities were therefore not adjusted near the coast. A precise calculation can be run with accurate seismic velocity models or core data to constrain density variations and thicknesses throughout the units.

Lastly, there exists an uncertainty in sediment loading models from the elastic thickness (T_e). Without prior lithospheric flexure studies in the western Canadian Arctic, there is no way to incorporate previous constraints for T_e in the models. The best way to constrain the elastic thickness of the lithosphere is to run models for varying T_e and analyse the results for the best fit. This study was approached in such a way to constrain the elastic thickness of the Arctic lithosphere by varying T_e. The uncertainty in T_e will be touched upon further in Chapter 5.

4.2 Project 2: 1D erosional isostasy modelling

4.2.1 Approach to 1D erosional isostasy models

Three transects (A, B and C) across Amundsen Trough, Banks Island, M'Clure Strait, and Prince Patrick Island (Fig. 4.10) were analysed with 1D erosional isostasy models. The aim of the transect models was to estimate the peripheral uplift on Banks Island and Prince Patrick Island from the incision of Amundsen Trough and M'Clure straight. Topographic data for the transect models were taken from the IBCAO Version 2.23, 2 km grid resolution polar stereographic map (Jakobsson et al., 2008). Table 4.2 outlines the parameters used in erosional isostasy modelling. Hypotheses tested in Project 2 are:

Hypothesis 2a: The elevated regions of the Arctic islands are a result of uplift from incision of the Arctic channels.

Hypothesis 2b: The concave up topographic profiles are the result of greater uplift on the Arctic islands near the channels.

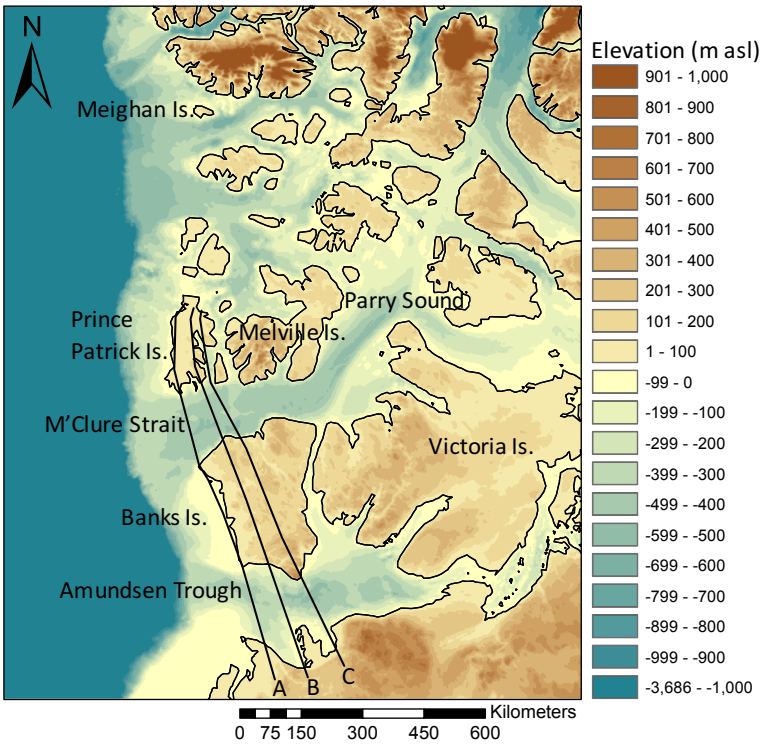

Figure 4.10 Area of interest for the erosional isostasy models. Transects A, B, and C are shown across Banks Island and adjacent channels. Elevation is measured in metres above modern mean sea level (m asl).

Table 4.2 1D erosional isostasy model parameters

Parameter	Value/Condition
Gravity constant (g)	9.81 m/s^2
Young's Modulus (E)	65 x 10^9 GPa
Poisson's Ratio (ν)	0.27
Mantle density (ρ_m)	3300 kg/m^3
Sediment density (ρ_s)	2165 kg/m^3
Water density (ρ_w)	1000 kg/m^3
Elastic thickness (T_e)	30, 60, and 90 km
Horizontal grid spacing (dx)	2 km
Vertical grid spacing (dy)	*Not applicable*
North boundary condition	*Not applicable*
South boundary condition	*Not applicable*
West boundary condition	Mirror
East boundary condition	Mirror

Two types of loading occurred during incision of the channels. Net loading in the channels includes the removal of sediment from the channels (negative loading) and infilling of water to modern sea level (positive loading). As demonstrated above (§4.2.1) lithospheric flexure is linear so the two loads can be calculated separately and summed to obtain the net loading. Multiplying the removed sediment thickness by the sediment density (dry porous quartz sand, $\rho_s = 2165$ kg/m^3) and the gravity constant ($g = 9.81$ m/s^2) converted the thickness to an applied load. Similarly, multiplying depths in the channels (from modern mean sea level) floor by the density of water ($\rho_w = 1000$ kg/m^3) and the gravity constant yields an applied water load in the channel.

For each initial 1D model the peripheral uplift on the Arctic islands was calculated in a forward model, incising the channels down from modern sea level. The uplift within the channel (uplift beneath the load) must be incorporated into the initial load to converge on a solution which matches the modern bathymetry. By masking the deflection on the islands only the uplift within the channels can be converted and added to the initial load (Fig. 4.11). Masking the islands allows for the peripheral uplift to be calculated without removing material from the islands. Iteratively adding the uplift in the channel to the initial load converged on a solution for the peripheral uplift on the adjacent channels and the modern bathymetry in the channels. Iterations did not consider changes in water loading. The net water load was set in the initial load and was not required to be adjusted. Therefore, increasing the sediment removed in the channels to include the deflection converged on a solution with modern bathymetry in the channels.

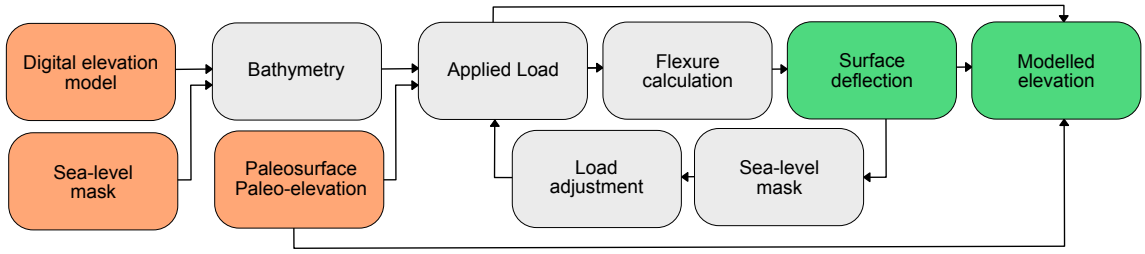

Figure 4.11 Flowchart for modelling incision of the channels. Orange boxes highlight model inputs and green boxes highlight model outputs.

Initial 1D models iteratively incised the channels down to modern bathymetry from modern mean sea level. The peripheral uplift on Banks Island was insufficient to achieve the observed elevations, suggesting a greater initial elevation. The observed topography on the islands was greater than the modelled elevations and therefore needed to be increased. Paleo-elevations estimated from the initial models were used to elevate the models and increase incision in the

channels. The paleo-elevations formed a 1.6 m/km paleogradient increasing eastward from the modern Arctic coast. Calculations for the models with initial paleo-elevations constituted the next stage of modelling.

By iteratively adjusting model outputs (deflection, $d(x)$) and applied loads, the model elevations (Fig. 4.11) converged on the modern elevations (Python codes in Appendix A). Removing the water load from the net applied load provided the net sediment load. Converting the sediment load to an eroded thickness provided the thickness of eroded sediment across the model. Adding the deflection, the eroded thickness and the paleo-elevation created a topographic profile for the 1D model. If the uplift of land proximal to the channels is positive, the result will be a concave-upward paleo-elevation cross-island transect oriented perpendicular to the channels.

In addition to incision of the channels, erosion on the Arctic islands was also included (Fig. 4.12). After initially converging on a solution, the peripheral flexure on Banks Island formed a smooth concave up curve and did not represent the observed topography of the island. Taking the difference in elevation between the model elevation and the observed topography indicated that additional erosion on land (from a higher paleo-surface) would be required to achieve topography similar to modern. Selecting the points where the model elevation is above the observed topography by masking all other points (with zeros) permitted the required erosion to be calculated (selected in Python code, Appendix A). Multiplying the masked difference between the model elevations and the observed topography by the sediment density (ρ_s) and the gravity constant (g) provided the additional load for erosion on the islands and in the channels. Adding the additional load to the previous load adjusted the net load to incorporate more erosion across the model (Fig. 4.11). Iteratively adding more erosion converged on a model solution. Iterations increased the deflection by increasing the net load (increasing eroded sediment). The increase in model elevations were still insufficient to achieve the observed topography on the islands. Models required further adjustments of the paleo-elevations and recalculation.

4.2.2 Results of 1D erosional isostasy modelling

Forward incision models for flexure of the Arctic lithosphere for all three T_e of 30, 60 and 90 km yielded the characteristic concave upwards 1D transects. As no prior elastic flexure models existed in the western Canadian Arctic, the outputs using different T_e provided constraint on the elastic thickness of the Arctic lithosphere by comparing the curvature of the 1D elevation

profiles with the modern topography. Initially, model incision originated at modern mean sea level using the iterative method outlined in section 4.2.1. Incising the channels from modern mean sea level was insufficient to reach the observed topography on Banks Island. Therefore, models required a greater paleo-elevation than modern mean sea level. A 1.6 m/km paleogradient increasing eastward raised the initial model elevations and subsequently the model elevations. Transect A had no initial paleo-elevation owing to its proximity to the Arctic coast. Assuming no net change in water loading from sea level change over the time period analysed requires the position of the coast to remain the same (assuming no erosion or deposition). The paleo-elevation for Transect B (60 km inland) was 100 m. The paleo-elevation for Transect C (100 km inland) was 160 m. Recalculation of the models involved incision of the channels from the paleo-elevation (Fig. 4.13 (a), 4.14 (a), 4. 15 (a)).

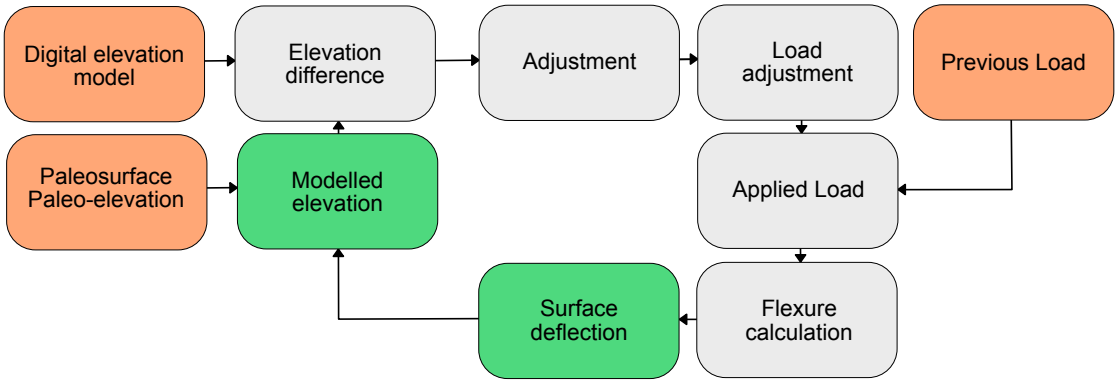

Figure 4.12 Flowchart for modelling erosion of the model across the western Canadian Arctic. Orange boxes highlight inputs and green boxes highlight outputs.

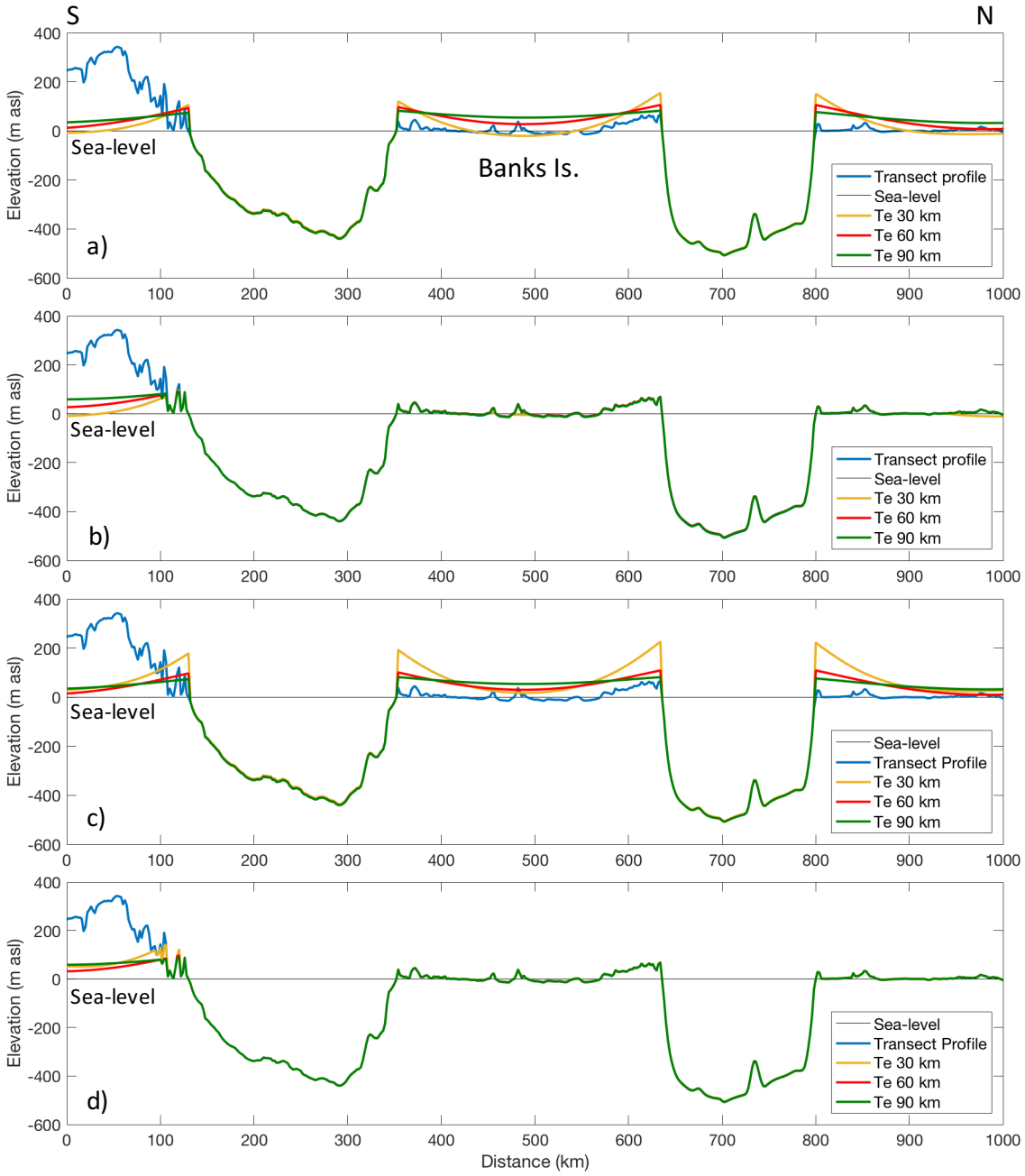

Figure 4.13 Models results for transect A. Transect can be found in Fig. 4.10. a) Model run for incision of channels only from a 1.6 m/km paleogradient originating at the coast. Initial model elevation is at modern mean sea level. b) Erosion of model in (a) on the observed topography. c) Adjusted model for incision of the channels only, incorporating the paleo-elevations found from b) (Table 4.3). d) Model erosion from c) down to observed topography. Note, the curves in d) are one on top of another. Model parameters can be found in Table 4.2. Elevations are measured in metres above modern mean sea level (m asl).

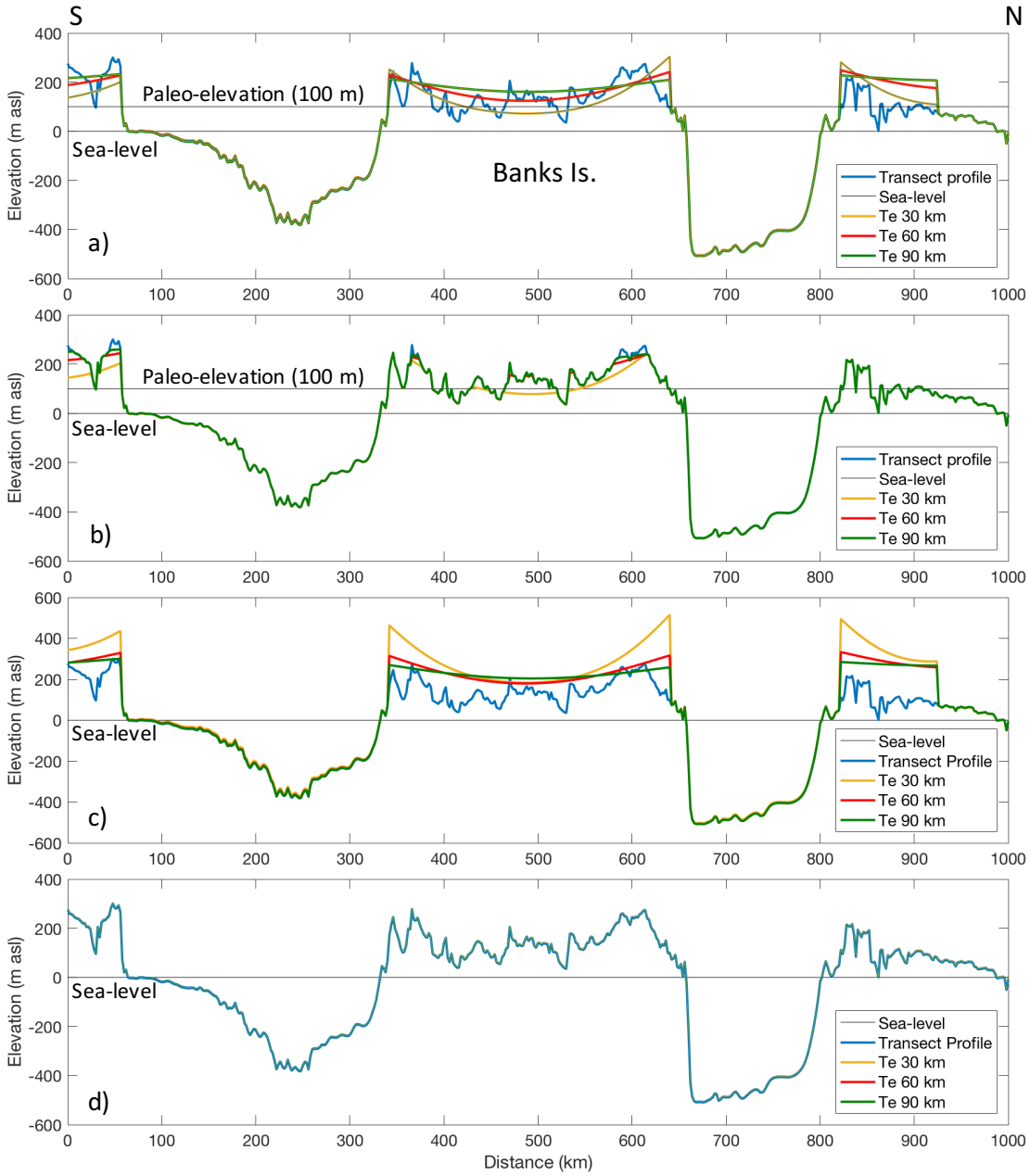

Figure 4.14 Models results for transect B. Transect can be found in Fig. 4.10. a) Model run for incision of channels only from a 1.6 m/km paleogradient originating at the coast. Initial model elevation is 100 m above modern mean sea level. b) Erosion of model in (a) on the observed topography. c) Adjusted model for incision of the channels only, incorporating the paleo-elevations found from b) (Table 4.3). d) Model erosion from c) down to observed topography. Note, the curves in d) are one on top of another. Model parameters can be found in Table 4.2. Elevations are measured in metres above modern mean sea level (m asl).

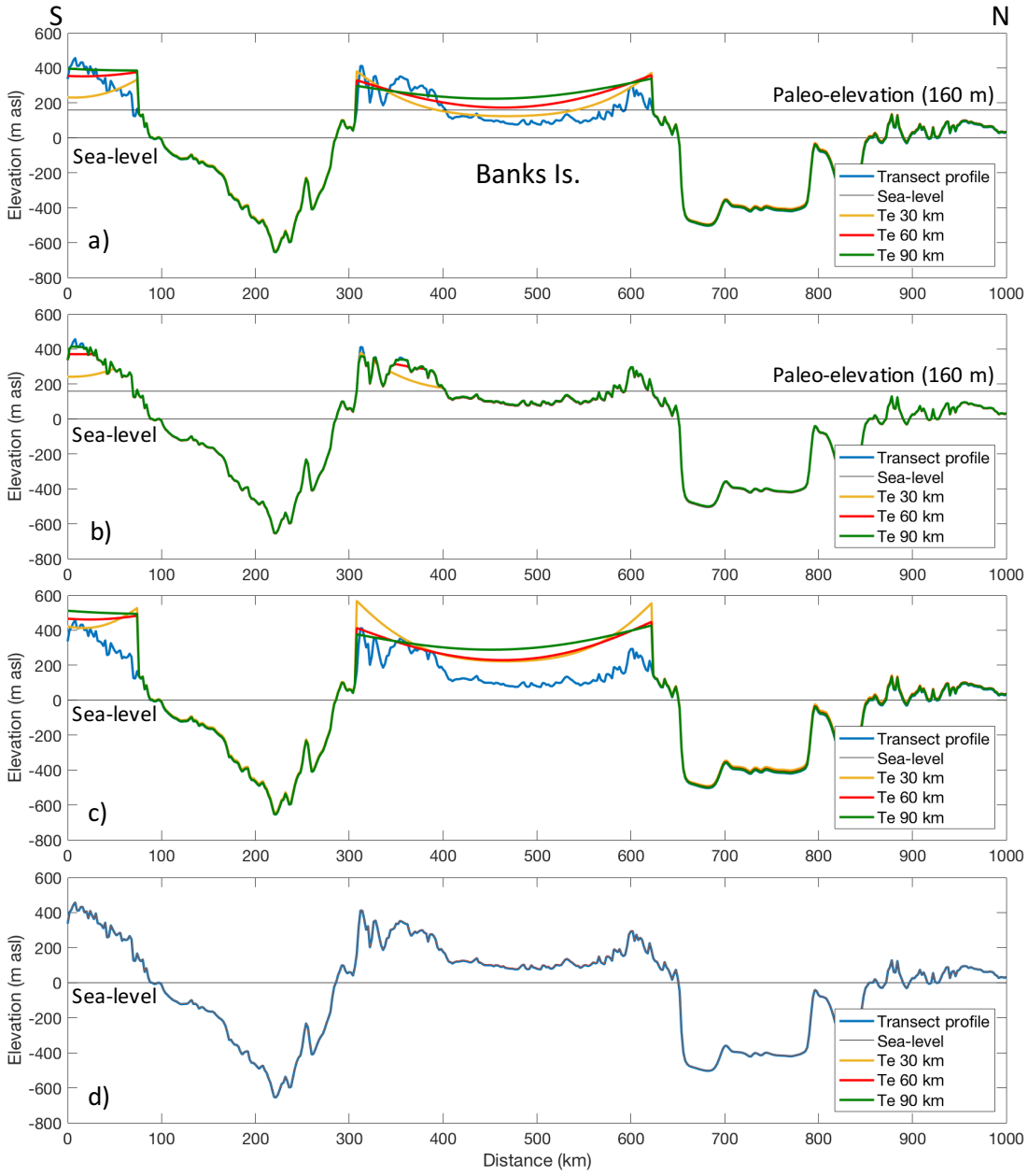

Figure 4.15 Models results for transect C. Transect can be found in Fig. 4.10. a) Model run for incision of channels only from a 1.6 m/km paleogradient originating at the coast. Initial model elevation is 160 m above modern mean sea level. b) Erosion of model in (a) on the observed topography. c) Adjusted model for incision of the channels only, incorporating the paleo-elevations found from b) (Table 4.3). d) Model erosion from c) down to observed topography. Note, the curves in d) are one on top of another. Model parameters can be found in Table 4.2. Elevations are measured in metres above modern mean sea level (m asl).

Modelled elevations formed smooth curves on Banks Island. The model elevations did not represent the observed topographic profile on Banks Island. For the models to sufficiently explain the elevated regions on the islands, the modern topography must be an achievable result

through erosion of the transects on the Arctic islands. Iteratively eroding the model to the observed topography on the islands was insufficient to achieve the modern topography (Fig. 4.13 (b), 4.14 (b), 4.15 (b)), suggesting a greater paleo-elevation and more erosion on Banks Island. Adding adjustments to the paleo-elevations based upon the previous model results by estimating the required elevations for each model converged on the observed topography (findings summarised in Table 4.3). Recalculation for incision of the channels from the adjusted paleo-elevations constructed profiles with elevations closer to the observed topography of the islands (Fig. 4.13 (c), 4.14 (c), 4.15 (c)). Again, the modelled elevation forms smooth concave up curves on Banks Island from the peripheral uplift. Eroding the models to the observed topography achieves an adequate match between the eroded model and observed topography (within 2 m) across Amundsen Trough, Banks Island, M'Clure Strait, and Prince Patrick Island (Fig. 4.13 (d), 4.14 (d), 4.15 (d)). This is expected in the model as raising the paleosurface (initial elevation) high enough will allow for erosion to the modern topography.

Table 4.3 Transect model paleo-elevations (measured above modern mean sea level)

T_e	30 km	60 km	90 km
Transect A	42 m	0 m	0 m
Transect B	224 m	151 m	135 m
Transect C	269 m	214 m	214 m

Additionally, the models predict a significantly larger degree of incision than from the current channel bathymetry. The increased incision in the channels resulted from the repeated additional incisions required to converge on a solution with the observed bathymetry in the channels. Differential erosion across the western Arctic will be discussed further in the 2D models.

4.3 Project 2: 2D erosional isostasy modelling

4.3.1 Approach to 2D erosional isostasy models

The expansion of 1D erosional isostasy models into 2D models involved map analysis for load calculations and interpretation of the 1D models results. A rotated version of the IBCAO Version 2.23 2 km raster (dot matrix composed of rectangular gridded point values) (Jakobsson et al., 2008) (slightly different than map used in sediment loading models) formed the dataset for 2D erosional isostasy models. Experimental models for 2D incision of the channels involved

expansion of the 1D models for 30, 60 and 90 km T_e. Table 4.4 outlines the constraints used in 2D erosional isostasy models.

Table 4.4 2D erosional isostasy model parameters

Parameter	Value/Condition
Gravity constant (g)	9.81 m/s^2
Young's Modulus (E)	65 x 10^9 GPa
Poisson's Ratio (ν)	0.27
Mantle density (ρ_m)	3300 kg/m^3
Sediment density (ρ_s)	2165 kg/m^3
Water density (ρ_w)	1000 kg/m^3
Elastic thickness (T_e)	30, 60, and 90 km
Horizontal grid spacing (dx)	2 km
Vertical grid spacing (dy)	2 km
North boundary condition	Periodic
South boundary condition	Periodic
West boundary condition	Mirror
East boundary condition	Mirror

Paleo-elevations from the 1D models (Table 4.3) provided constraints on the paleosurfaces for 2D modelling. Gradients constructed between transects A-B, and B-C (Table 4.3) estimated the paleosurface near the coast. Creation of the paleosurfaces (Appendix C) involved four segments: offshore, the area between transects A and B (0-60 km from the coast), the area between Transects B and C (60-100 km from the coast), and a continental plateau (east of Transect C). The offshore segment is constant with zero paleo-elevation. The offshore segment does not have any significance in the incision models and is therefore removed (masked with zeros) in the calculations. Flexure east of the loading offshore is tiny (less than 20 m) and is therefore insignificant in comparison the uplift from incision (100's m). Estimated gradients perpendicular to the strike of the coast from the 1D models laterally increase the paleosurface eastward. Results of the previous models (§4.2) indicated that the BF had a significantly greater volume than its current mapped distribution along the west edges of the archipelago. Therefore, a west-dipping gradient was assumed in accordance with the approach in §4.2. The validity of this assumption will be discussed in Chapter 5. The gradients calculated between Transects A and B

form the first increase in the paleosurfaces. Gradients between the Transects B and C form the second segment of eastward increase in the paleosurface. Lastly, east of Transect C the elevations are assumed to be constant to create a topographic plateau (equal to the paleo-elevation of transect C). Euclidean distance from the coast (in ArcMap) provided the distances for gradient calculations. Clipping the Euclidean distance rasters in the shape of the desired polygons created the separate segments for the paleosurface. Simple algebraic operations (using map algebra in ArcMap) on the clipped rasters manipulated the gradients and elevations of each segment. Combining the rasters (mosaic to raster in ArcMap) for the separate segments provided paleosurfaces for each model (30, 60 and 90 km T_e)(Appendix C). Uncertainties in the paleosurfaces will be discussed further in section 4.3.3.

2D erosional isostasy models for incision from a paleosurface involved the same techniques used in the 1D incision models (Fig. 4.11 and 4.12). Initial incision estimates come from the difference between the paleosurface elevation (above modern mean sea level) and the bathymetry of the Arctic channels. Multiplying the incision thickness by the sediment density ($\rho_s = 2165$ kg/m^3), gravity constant ($g = 9.81$ m/s^2), and mask (zeros) over the islands converted the sediment thickness to an applied (negative) load. Similarly, multiplying the bathymetry (depth below modern mean sea level) in the channels by the density of seawater and the gravity constant converted the water depth to an applied (positive) water load. Adding the water load and sediment load provided an initial load for the 2D incision of the channels. Initially, 2D models accounted for incremental increases of incision in the channels (owing to deflection in the channels) to calculate the peripheral uplift on the islands. The approach used for incrementally increasing the loads is the same as for the 1D models (Fig. 4.11). Similar to the 1D results, the 2D modelled elevations formed smooth curves on the islands. Therefore, 2D models required further incision on the Arctic islands to resemble the observed topography. The approach to eroding the models on the islands was the same as the 1D models (Fig. 4.12).

Lastly, the negative loading across the western Canadian Arctic predicted by the models indicates widespread differential erosion. Eroded thickness maps were constructed by removing the water load from the applied load and converting the remaining applied load to sediment that would have been removed throughout the western Arctic. The eroded thickness was also used in the construction of model elevations (Fig. 4.11).

4.3.2 *Results of 2D erosional isostasy modelling*

2D models for incision of Arctic channels involved modelling incision from paleosurfaces for 30, 60 and 90 km T_e (Fig. 4.13, 4.14 and 4.15). Initial models incorporated only the iterative solutions for the incision of the channels and predicted the elevations on the islands from the initial paleosurface and peripheral uplift (Fig. 4.16, 4.17, and 4.18). These models form smooth curves on the Arctic islands which reflect the regional deflection pattern ($d(x)$) and not the observed topography.

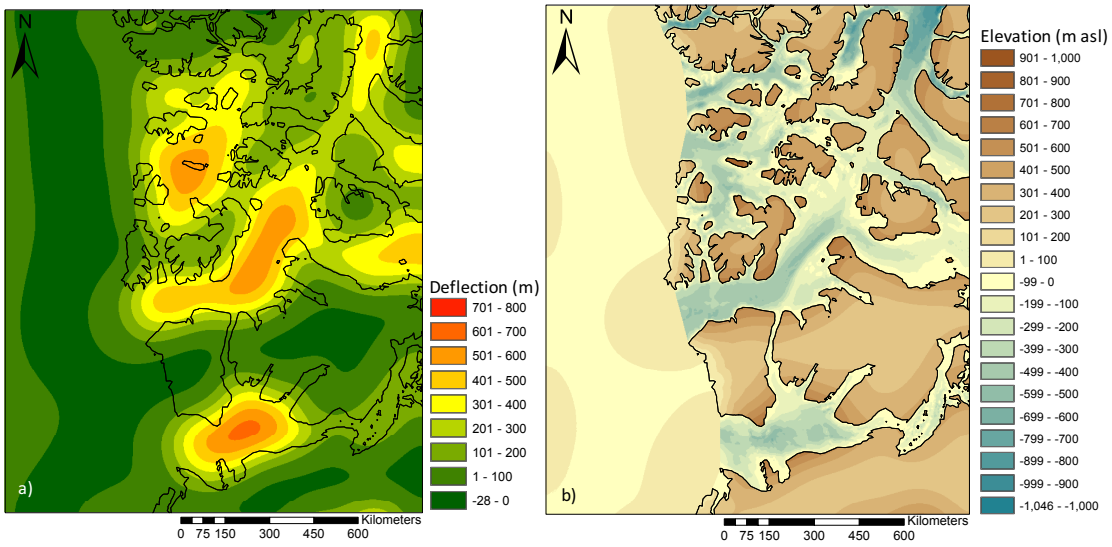

Figure 4.16 Model result for incision of the channels only under 30 km T_e. a) Regional isostatic uplift (deflection, $d(x)$) for the western Arctic. b) Modelled elevations from regional deflection and incision. Elevation is measured in metres above modern mean sea level (m asl). Model parameters can be found in Table 4.4.

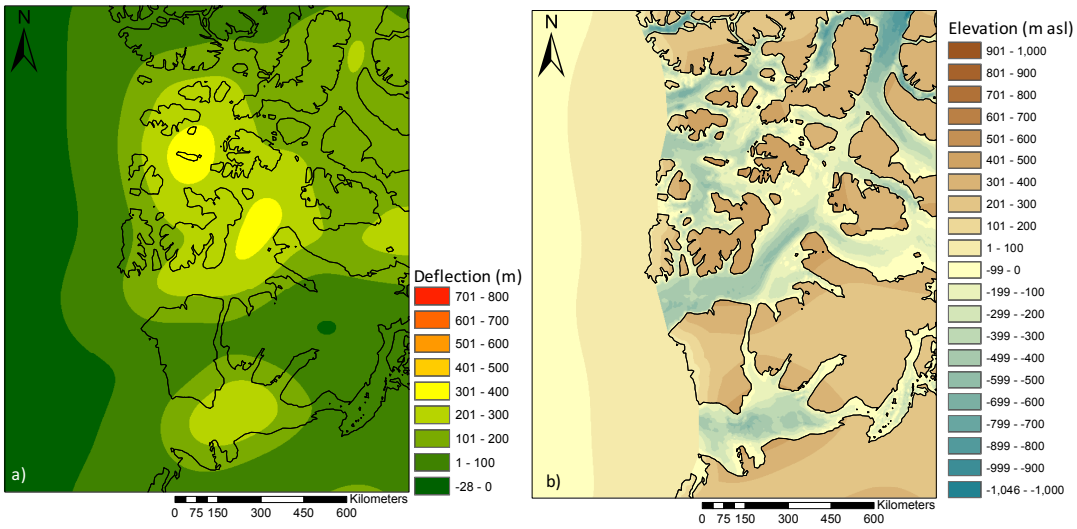

Figure 4.17 Model result for incision of the channels only under 60 km T_e. a) Regional isostatic uplift (deflection, $d(x)$) for the western Arctic. b) Modelled elevations from regional deflection and incision. Elevation is measured in metres above modern mean sea level (m asl). Model parameters can be found in Table 4.4.

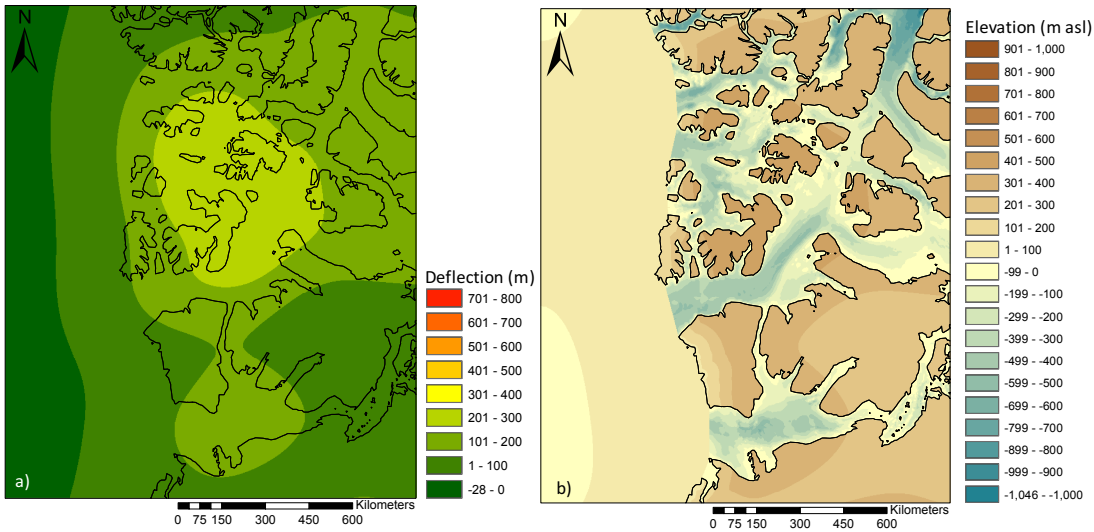

Figure 4.18 Model result for incision of the channels only under 90 km T_e. a) Regional isostatic uplift (deflection, $d(x)$) for the western Arctic. b) Modelled elevations from regional deflection and incision. Elevation is measured in metres above modern mean sea level (m asl). Model parameters can be found in Table 4.4.

Incorporating erosion on the islands converged on more realistic model elevations that resemble the observed topography (Fig. 4.19, 4.20, and 4.21). As expected, increasing the net (negative) loading increases the regional deflection across the Arctic. Observed topography on the islands are adequately achieved (within several m's) in the 60 and 90 km T_e models. Predictions in 30 km T_e model were not sufficient enough to reach the observed topography

towards the centre of some islands. The inability to reach the observed topography in the centre of the islands stems from a smaller flexural wavelength (λ) than the width of the islands (Fig. 4.19).

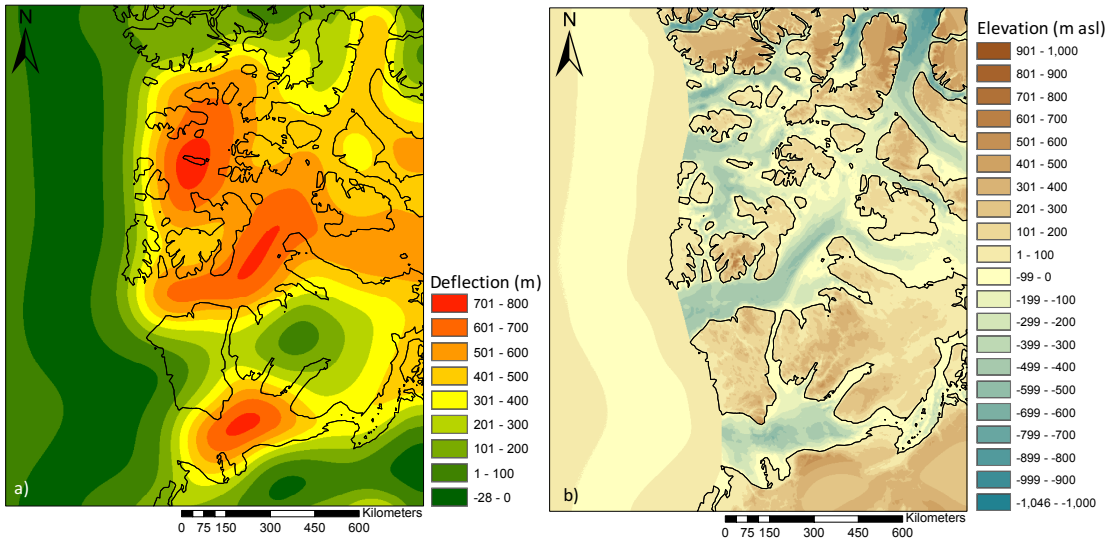

Figure 4.19 Model result for incision of the channels and erosion across the western Arctic for 30 km T_e. a) Regional isostatic uplift (deflection, $d(x)$) for the western Arctic. b) Modelled elevations from regional deflection, incision and erosion. Elevation is measured in metres above modern mean sea level (m asl). Model parameters can be found in Table 4.4.

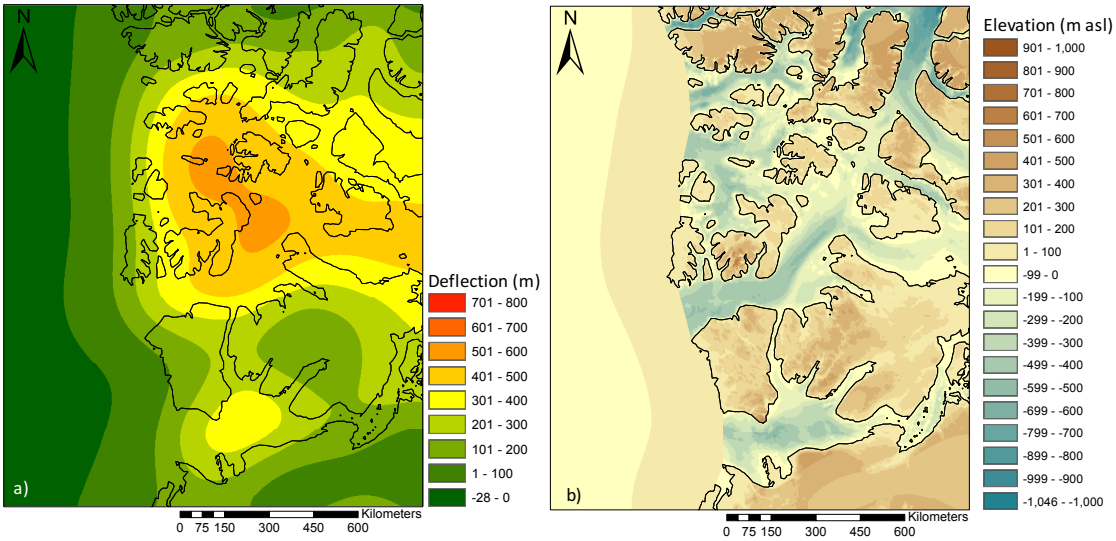

Figure 4.20 Model result for incision of the channels and erosion across the western Arctic for 60 km T_e. a) Regional isostatic uplift (deflection, $d(x)$) for the western Arctic. b) Modelled elevations from regional deflection, incision and erosion. Elevation is measured in metres above modern mean sea-level (m asl). Model parameters can be found in Table 4.4.

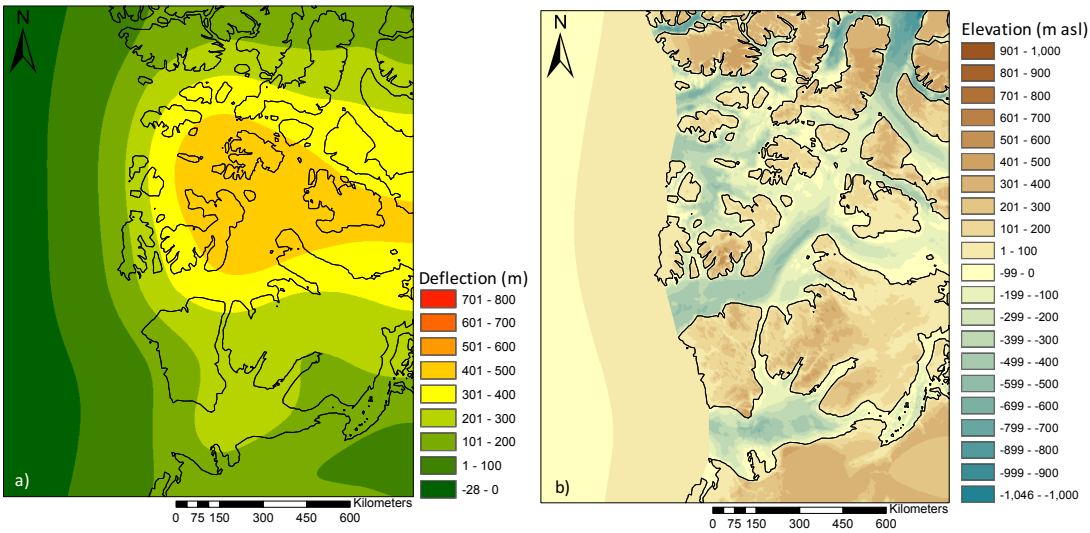

Figure 4.21 Model result for incision of the channels and erosion across the western Arctic for 90 km T_e. a) Regional isostatic uplift (deflection, $d(x)$) for the western Arctic. b) Modelled elevations from regional deflection, incision and erosion. Elevation is measured in metres above modern mean sea level (m asl). Model parameters can be found in Table 4.4.

The 2D models constructed for incision of the Arctic channels show smooth surfaces on the islands, similar to those observed in the modern topography of the islands. The curvature of the curves trend perpendicular to the strike of the channels which agrees with the results from the 1D incision models (§4.2). The models predict topographic highs on the islands from peripheral uplift along the channel flanks, proximal to the channel edge. The surface uplift along the channel shoulders appear to mimic the topographic highs observed on several of the western Arctic islands, such as the southeastern and northeastern coasts of Banks Island (Fig. 4.10).

Removing the water load from the net applied load leaves the removed sediment load which can be converted to the thickness of sediment removed across the model (Fig. 4.22, 4.23, and 4.24). A significant degree of differential erosion is predicted in the late-Cenozoic flexural models. The models predict incision in the channels is substantially larger than the observed elevation change, reaching upwards of 1600 m (in the 30 km T_e model) in Parry Sound (Fig. 4.22).

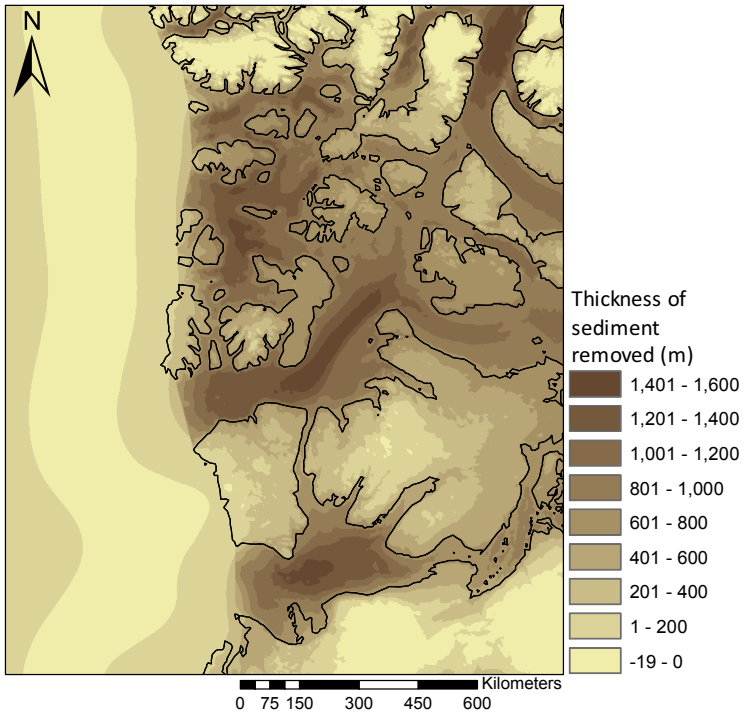

Figure 4.22 Thickness of sediment removed across the western Artic from the incision and erosion for a 30 km T_e.

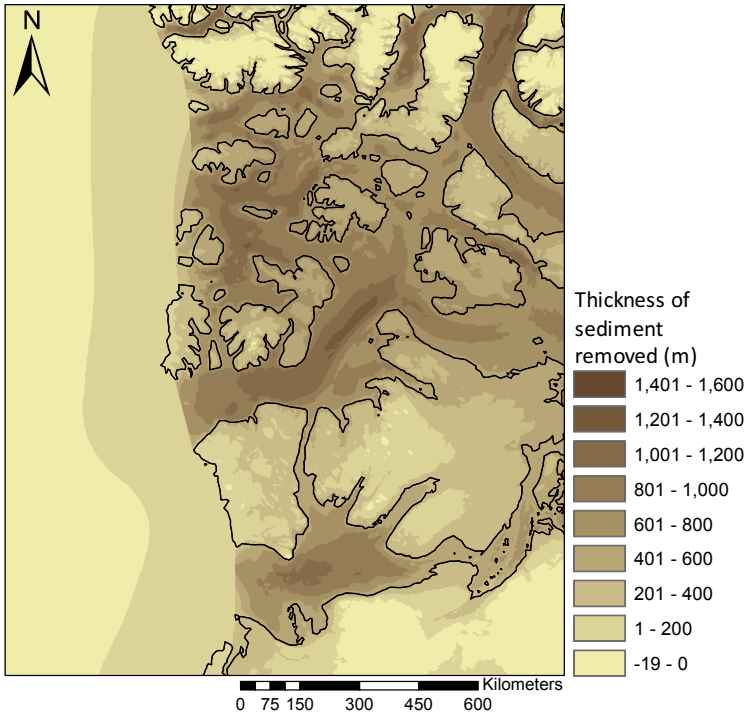

Figure 4.23 Thickness of sediment removed across the western Artic from the incision and erosion for a 60 km T_e.

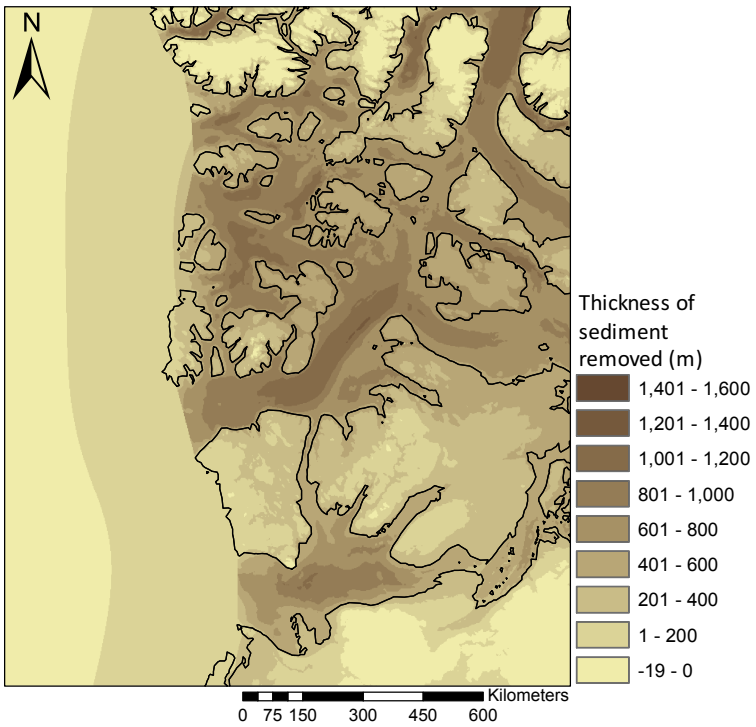

Figure 4.24 Thickness of sediment removed across the western Artic from the incision and erosion for a 90 km T_e.

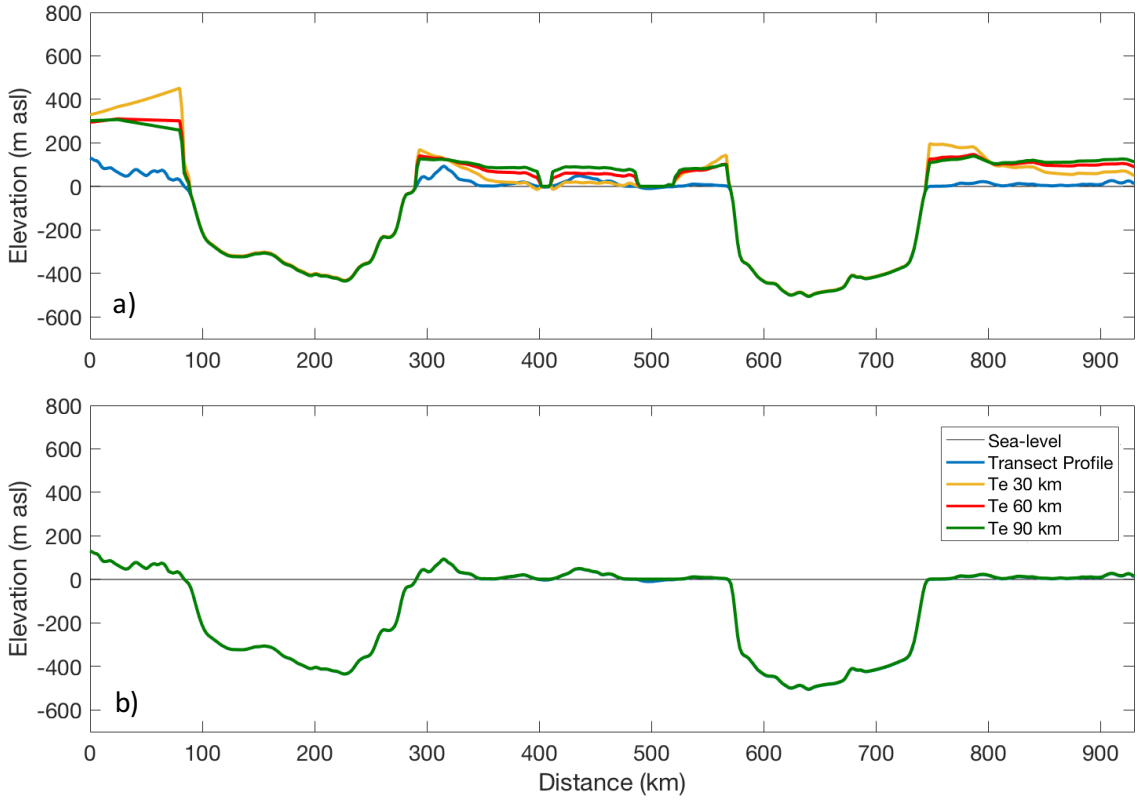

Figure 4.25 Results for 2D models along Transect A. a) The modelled elevations from the 2D models along transect A. b) The eroded 2D model results along Transect A. Elevation is measured in metres above modern mean sea level.

Transects A, B and C can be taken through the 2D models to compare the 1D and 2D model results (Fig. 4.25, 4.26, and 4.27). A larger peripheral flexure is observed in the 2D models owing to increased loading from the expansion from 1D to 2D. This is to be expected as the 1D models only account for an infinitesimal small load perpendicular to the strike of the transect, not accounting for the additional flexure from material removed proximal to the transects. The largest variation is observed in the 30 km T_e 2D model, predicting an elevation of 800 m southern Banks Island (Fig. 4.25), greater than the 600-m predicted in the 1D model (Fig. 4.16 (c)) and the observed topography (~400 m) (Fig. 4.16 (d)).

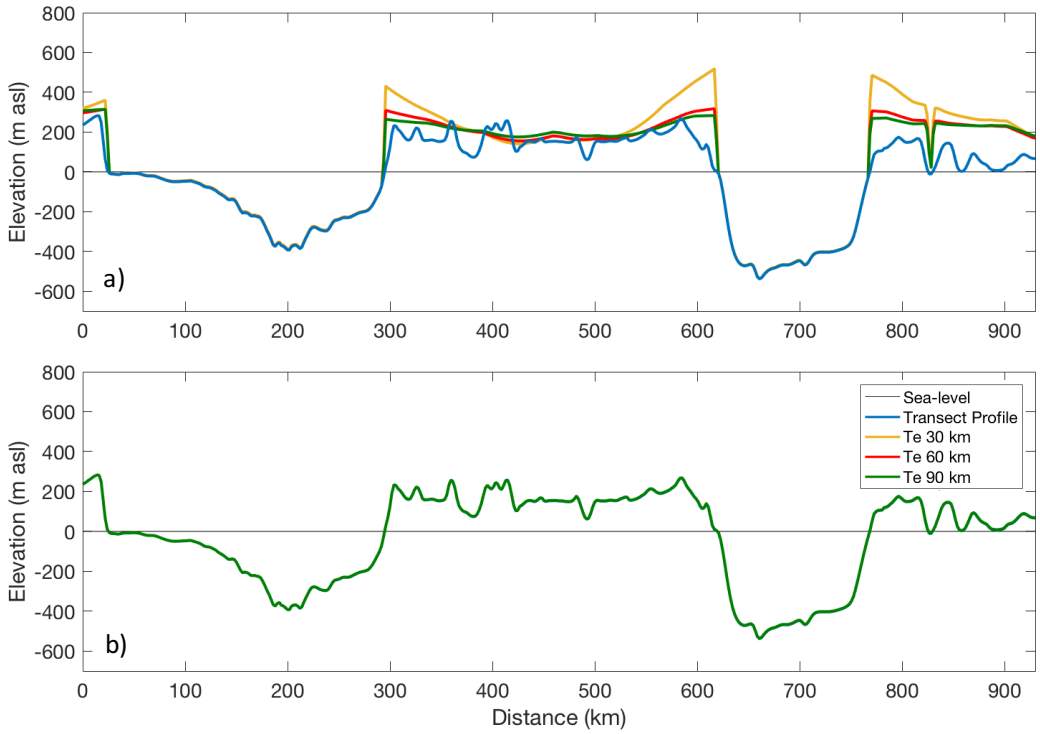

Figure 4.26 Results for 2D models along Transect B. a) The modelled elevations from the 2D models along Transect B. b) The eroded 2D model results along Transect B. Elevation is measured in metres above modern mean sea level.

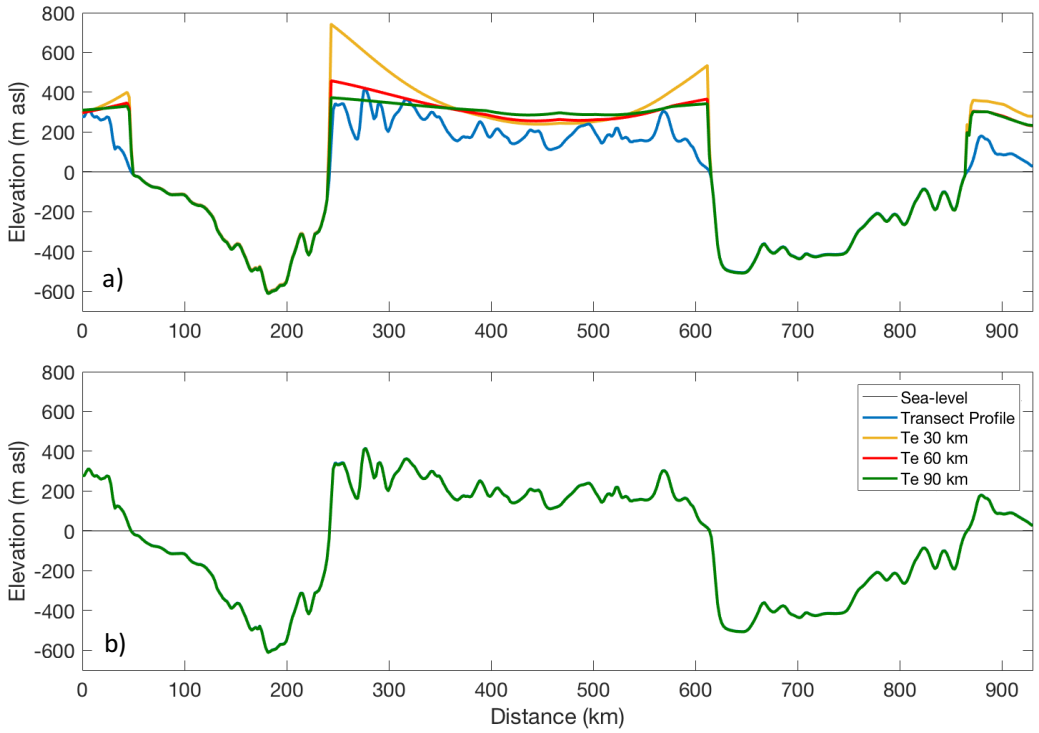

Figure 4.27 Results for 2D models along Transect C. a) The modelled elevations from the 2D models along Transect C. b) The eroded 2D model results along Transect C. Elevation is measured in metres above modern mean sea level.

4.3.3 *Uncertainty in erosional isostasy models*

The largest uncertainty in the erosional isostasy models is the paleo-elevations (1D models) and the paleosurface (2D models). Thermal maturity records from late-Cretaceous sediments suggesta substantial degree of the sediment has been deposited and removed in the Cenozoic (Bustin, 1986). Thermal maturity data could therefore aid in constraining the paleotopography of the western Canadian Arctic. However, it is uncertain if it was BF removed and can therefore not be used at this time to constrain the paleo-elevations for the top of the Bf. The only applicable constraints on potential paleotopography are from the sedimentological studies of the BF. The transect models predict a minimum elevation above modern mean sea level for which incision must have begun to reach the observed topography of the islands. The paleo-elevation may have been above this minimum elevation and has since eroded down to the observed topography. Therefore, the best estimation for minimum paleo-elevations near the coast are those from the 1D models.

There is uncertainty in the model around the highlands close to the northern, eastern and southern boundaries. These regions lie outside the study area and are therefore not considered when analysing and interpreting the model results. These areas, such as the Eureken Orogen to the east, have had external factors influencing lithospheric flexure. Paleosurfaces do not incorporate the topography in these elevated regions. The models predict these regions surrounding the western Canadian Arctic have experienced some degree of peripheral uplift from incision of the channels.

Additionally, there is uncertainty in the density of material eroded from the channels. Models assume sediment filled the channels during the Pliocene. Calculations involve only the removal of sediment from the channels with no consideration for the removal of bedrock. However, incision of the channels may have involved the removal of bedrock. Removing bedrock from the channels increases the density of the material removed and subsequently increases the regional deflection (uplift). If incision of the channels involved the removal of bedrock, an expected increase in peripheral uplift on the arctic islands and increased incision in the channels from the increase in net loading (more mass removed). Further analysis of seismic data could show incision through bedrock or excavation of sediment in the channels.

As in the previous sections, uncertainty exists in the elastic thickness of the Arctic lithosphere. The elastic thickness of the Arctic lithosphere will be discussed further in Chapter 5.

Chapter 5 Discussion

5.1 Interpretation of results

5.1.1 Late-Cenozoic landscape evolution of the western Canadian Arctic

Lithospheric flexure had partial control over late-Cenozoic landscape evolution of the western Canadian Arctic. The landscape during the Pliocene (during deposition of the BF) was proposed by others to be a continuous shallow-dipping coastal braid plain (Braschi, 2015; Fyles, 1990; Rybczynski et al., 2013; Tozer, 1955) which may have extended from the Mackenzie Delta region to Ellesmere Island. Sedimentation increased significantly during the Pliocene (Braschi, 2015; McNeil et al., 2001). Erosion and deposition redistributed sediment (changing surface loading) across the western Arctic and will have caused regional isostatic adjustments. Seismic interpretations show deposition of a thick sequence of sediment offshore during the Pliocene (Helwig et al., 2011).

5.1.2 Ribbon-like distribution of the Beaufort Formation

The geometry and distribution of the BF suggest an outside factor controlling available accommodation space. Models predict significant (up to 500 m) flexural subsidence along the western continental shelf from deposition offshore during the Pliocene. Models for Pliocene sediment loading predict peripheral uplift on the western Arctic islands up to 20 m, extending up to 200 km from the modern coast. Despite being relatively low, the predicted uplift may be sufficient to marginally alter Pliocene drainage patterns for low order streams. This is similar to how small anticlines above blind thrusts or in regions of transpression have been observed to deflect streams around them. However, the rate of the peripheral bulge uplift may be too slow to allow this. While more field work is necessary to demonstrate the possibility that a low amplitude bulge could deflect streams and preserve the

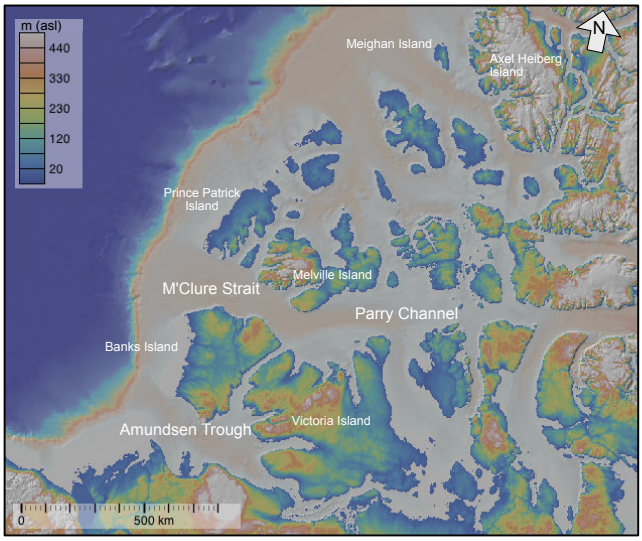

Figure 5.1 Map of western Arctic Map of the western Canadian Arctic outlining the islands and regions discussed in Chapter 5. Basemap from Jakobsson et al. (2008).

ribbon of BF along the western portion of these islands, the significant variation in topographic relief in the onshore BF surface today would easily allow for antecedent streams to have flowed through the bulge at different times. Furthermore, L. Hills (unpublished field notes) and Braschi (2015) report a > 10 m high cut and fill sequence on northern Banks Island that generally parallels paleoflow orientations obtained throughout the BF. That channel may have been an example of relief on the BF coastal plain (perhaps generated through one glacial-interglacial cycle). Changes in stream erosion may explain the north-south trending channel (along strike of the coast) between Banks Island and Victoria Island (Fig. 5.1). Deposition persisted west of the peripheral uplift where accommodation space was available allowing for the thin ribbon-like distribution of BF.

One factor not considered in this study is the effect of Miocene sediment loading offshore. There may be some additional accommodation space created from Miocene deposition offshore which would increase the overall accommodation space available for the BF. Further modelling is required to quantify the degree of flexural downwarping required from Miocene sediment loading in addition to the Pliocene and Pleistocene. These tests can be carried out by quantifying the addition flexural downwarping required for deposition of the entire BF.

5.1.3 Opening of the Northwest Passages

Global cooling began in the Pleistocene (Hansen et al., 2013; Lisiecki and Raymo, 2005). The Innuitian and Laurentide Ice-Sheets covered much of the western Canadian Arctic during the glacial periods. Erosion underneath the ice-sheets likely increased in weaker regions where fluvial incision had previously existed (England, 1987). Ice-streaming carved into the sediment-filled channels while preserving the extant Arctic islands under ice caps and ice divides which were eroded to a much lower degree (England et al., 2006; Lakeman and England, 2012; Stokes et al., 2005). Glacial incision of the Arctic channels transported sediment offshore and therefore changed the surface loading across the western Arctic. The Arctic lithosphere adjusted to the changes in loading by uplifting in the regions where sediment was removed and subsiding in the regions of sediment deposition. Peripheral uplift on the Arctic islands shaped the topography of the islands to form concave up topographic profiles. Lithospheric flexure cannot completely explain the topography on the islands, suggesting elevations of the Pliocene coastal plain were greater than modern mean sea level, a consistent observation from the lithofacies of the BF. Furthermore, the models predict strong differential erosion across the western Arctic. Models

predict the greater late-Cenozoic erosion of the central Arctic islands (i.e. Melville Island) than those to the west. These correspond to areas of higher deflection from the incision of the channels (around Parry Sound, Fig. 5.1).

5.1.4 Pliocene paleosurface

The model predictions are insufficient in and of themselves to explain the elevations for many of the Arctic islands. Models required adjusting the initial paleosurface and additional erosion to achieve the observed topography on the islands. The initial paleo-elevations for models with T_e of 60 and 90 km do not exceed a maximum elevation of 214 m with shallow (less than 10 m/km) topographic gradients near the coast. Therefore, elevations of the western Canadian Arctic Islands likely did not exceed 214 m at the end of the Pliocene. Models predict deposition of the BF formed a paleosurface consisting of a shallow dipping (toward the Beaufort Sea, west-northwest) coastal plain. The paleosurface predictions are consistent with interpretations of the depositional environment of the BF and the paleoflow measurements within the BF.

Models and field observations (paleoflow) indicate that during deposition of the BF the Northwest Passages could not have been present and were likely filled with sediment. Incision of the sediment filled channels led to uplift of the adjacent Arctic islands and opening of the Northwest Passages (England, 1987).

5.1.5 Erosion across the western Canadian Arctic

The smooth topography on the islands predicted in the models is not accurate compared to the observed topography. Eroding the models across the western Arctic to the observed topography provides a second-order approximation for the minimum thickness of sediment eroded. However, mapping the predicted eroded thickness for each model (Fig. 4.22, 4.23, and 4.24) across the western Arctic shows a higher degree of erosion on the central Arctic Islands such as Melville Island (Fig. 5.1). The deflection is greater in the central Arctic and therefore the model predicts greater elevations and requires more erosion to reach observed topography. The higher T_e models (60 and 90 km) predict significantly less erosion on the central islands. Similarly, deflection in the channels required significantly greater incision in the channels than observed by topographic relief between the topography of the islands and depths of the channels. Models predict up to 1600 m (Parry Sound in 30 km T_e model for erosional isostasy) of erosion in order to compensate for concurrent isostatic uplift in the channel and obtained the observed

bathymetry. Glaciers can erode channels this deep and below sea-level if they are sufficiently thick (Medvedev et al., 2008; Medvedev et al., 2013), thereby deepening of the Arctic channels through glacial incision.

5.1.6 Elastic thickness of the Arctic lithosphere

Model results suggest the elastic thickness (T_e) of the Arctic lithosphere is likely no less than 60 km. The correlation between 60 and 90 km T_e in the incision models suggests a 60 km T_e is an adequate elastic thickness for the Arctic lithosphere. A T_e greater than that present will provide a similar result to the actual value, as variations in the deflection start to decease as you increase T_e past the value. A 30 km T_e was insufficient in most models and suggests either the paleo-elevation was insufficient or the modelled plate was not strong enough and therefore required a greater T_e. A T_e of 60 km or greater is consistent with the regional geology. The Laurentian Crust forming most of the Arctic lithosphere (Houseknecht and Bird, 2011) is a notably strong tectonic environment in other regions of Canada (Flück et al., 2003) (70-110 km T_e). Project 1 results do not favour a specific T_e. Potentially a thinner T_e could explain the thickness of the BF along the coast by increasing the amplitude of deflection ($d(x)$) and decreasing the flexural wavelength. To test this idea requires further testing with lower values of T_e for flexural downwarping from Pliocene sediment loading.

Work of Schaeffer et al (2014) shows a thick Arctic lithosphere around Banks Island which thins to the north (towards Axel Heiberg Island). The lithospheric thickness maps presented in Schaeffer et al (2014) is sufficient to have an elastic fraction (T_e) thicker than 60 km and are thereby in agreement with the models presented. The thinning of the lithosphere towards the north likely corresponds to a decrease in T_e and a change in flexural patterns. The decrease in T_e would accompany a narrower region along the coast to be affected by flexure and may therefore explain the thinning of exposed BF in the north.

5.2 Answers to initial questions

5.2.1 Modelling Project 1: sediment loading

The questions asked pertaining to the first modelling project were: a) Is the ribbon-like distribution of the BF the result of accommodation space created from flexural subsidence? and b) Is the observed tilt of the peat layer at Ballast Brook a consequence of flexural downwarping along the western Arctic margin?

Hypothesis 1a: The orientation, width, and thickness of the currently exposed BF is consistent with the geometry and orientation of the accommodation space generated by loading. This hypothesis was not falsified. The late-Cenozoic sediment loading models predict a measurable portion of the BF near the western Arctic coast is the result of accommodation created from flexural subsidence during the Pliocene. Subsidence from the deposition of the Pliocene unit offshore is slightly smaller than the observed thickness of the BF near the coast. The geometry of the accommodation space predicted in the modes (Fig. 4.8) matches the observed geometry of the BF. Furthermore, peripheral flexure east of the loading may have been sufficient to slightly reduce the amount of lateral planation that may otherwise have occurred on them. However, the models do not predict the full observed thickness of the BF near the coast. This discrepancy between model predictions and observations could be caused by an error in picking the seismic horizons and analysis of sediment cores.

Hypothesis 1b: The tilt of an originally horizontal Miocene peat bed should be basinward and equal or greater than that predicted by loading by the Pliocene and Pleistocene sediments. The peat at Ballast Brook is observed to have a tilt of 6.4 m/km. Its orientation would require that if the peat had an overall basinward gradient, the tilt would be greater than the 6.4 m/km rake. The models predict the tilt of the peat from flexural subsidence along the western Arctic margin is 2.7-3.7 m/km in the same direction as the observed tilt, i.e. a component of the basinward gradient. The predicted tilt is only half of the observed tilt. Therefore, the observed tilt of the peat at Ballast Brook is only partially explained by flexural subsidence from sediment loading offshore. The greater observed tilt may be attributed to uncertainties in the boundary conditions or parameters used in the models. However, the peat may also have been deformed by local faulting or slumps into the Ballast Brook valley.

The most significant geological result of this study is the lack of explanation for the tilt of the peat. Only half of the 6 m/km tilt can be explained, suggesting another process(es) have affected the western Canadian Arctic since the late-Miocene. These could be related to active faulting in the region, evident by large listric faulting offshore. However, these faults tend not to cross-cut the Pliocene-Pleistocene sedimentary packages.

5.2.2 Modelling Project 2: erosional isostasy models

The second modelling project consisted of forward models for the incision of the Arctic channels. The modelling experiments evaluated the response of the Arctic lithosphere from the

incision of the Arctic channels through elastic flexure of the Arctic lithosphere. One question asked of the models was: can the elevated regions on some of the Arctic islands be explained by the regional isostatic response from incision of the channels? Furthermore, are the concave up shapes (perpendicular to the strikes of the channels) of some of the islands the result of isostatic adjustments of the Arctic lithosphere from incision of the channels?

The erosional isostasy models predict elevated regions on the Arctic islands are a result of elastic flexure of the Arctic lithosphere from incision of the channels. Peripheral uplift from the incision of the channels is greatest on the islands proximal to the channels. This result explains the concave up shape of some of the islands.

5.3 Support for models and future work

High-resolution seismic data are required to validate or refute the models presented. Shallow seismic surveys are required to understand the surficial geology of the Arctic Islands and to comprehend late-Cenozoic landscape evolution of the western Canadian Arctic fully. Better constraints on parameters that showed uncertainty in this study (densities, elastic thickness, sediment thickness, etc.) could significantly increase the accuracy and quality of the models.

Future work to understand late-Cenozoic landscape evolution of the western Canadian Arctic should include sedimentological, geochronological, geodynamical and geophysical studies. A better understanding of Pliocene and Pleistocene erosion rates would aid in future geodynamical modelling. Studies into the active and recent tectonics along the western Arctic margin would support or refute some of the findings of this study. Lastly, better constraints on the distribution, thickness and extents of the BF would significantly help future Arctic Cenozoic research in the western Canadian Arctic.

Sedimentological studies for grain size analysis could provide estimates for the paleogradient the BF was deposited. This would further constrain the base Pliocene and lead to estimates for the Pliocene paleosurface for the top of the BF.

Further coal moisture and thermal maturity estimates of the ESG and late-Cretaceous sediments would provide better constraints on the thickness of eroded sediment on the islands. This would provide a link with the sediment erosion maps outlined in the 2D erosional isostasy models and may provide a better control on the elastic thickness of the Arctic lithosphere.

5.4 Social/economic implications

Much of the economic significance of this research pertains to petroleum exploration in the western Canadian Arctic and navigation of the Canadian Arctic. The petroleum industry has a vested interest in research of this nature for an understanding of the evolution of the Canadian Arctic and petroleum prospects and plays in the Beaufort Sea. Petroleum production has occurred in Alaska and the Canada Basin since the 1920's symmetric rift flanks from the western Arctic Archipelago. Exploration of the hydrocarbon potential in recent decades increased research interests along the western Arctic margin in the geological community. With diminishing sea-ice cover in recent decades, hydrocarbon extraction in the western Canadian Arctic is more feasible. Petroleum industries must have knowledge of the formations overlying prospective reservoirs, potentially impacting hydrocarbon recovery.

Petroleum companies must consider the environmental impacts of their work. Understanding the surficial geology, it's origin and potential geological and environmental hazards is required for companies to initiate work. The BF is exposed along much of the Arctic coast and holds may paleoenvironmental records which petroleum companies should acknowledge.

The total amount of the apparent tilt of the Miocene peat in Ballast Brook cannot be explained through the flexural downwarping. Thus there are likely other processes affecting the landscape in the western Canadian Arctic in this region. These may include tectonic activity which pose hazards for petroleum exploration and locals in the western Arctic.

Chapter 6 Conclusions

Late-Cenozoic flexure of the Arctic lithosphere affected landscape evolution of the western Canadian Arctic. Sediment loading from the deposition of Pliocene and Pleistocene sedimentary packages offshore drove regional subsidence along the western Arctic margin. Incision of the channels drove uplift on the Arctic islands, leading to erosion and exhumation of lower stratigraphic units on the islands from secondary differential erosion.

Several hundred metres of subsidence from sediment loading created accommodation space along the Arctic coast during the Pliocene. The orientation and geometry of the flexural subsidence resembles the mapped onshore distribution of the Beaufort Formation. Furthermore, flexural subsidence models predict half the tilt observed in a marker bed on northern Banks Island. However, it is also possible that all or some of the tilting of the marker bed may be the result of unrecognized tectonic activity or slumping. Incision of the channels has led to several hundred metres of regional isostatic uplift across the western Canadian Arctic, upwards of 500 m of uplift in areas. Deflection patterns suggest significantly greater incision of the channels is required to reach the modern bathymetry, reaching as much as 1200 m in Parry Channel.

Interpretation of additional high-resolution seismic surveys is required to support or refute the models presented in this study. Access to these data in the channels are required to confirm the apparent lack of faults under the channel wall escarpments. Further research into the nature and extent of neotectonics in the region, such as on Prince Patrick Island, is required to fully understand recent regional landscape evolution.

Analysing the behaviour of the equilibrium from surface loading can help understand and model isostatic adjustments (flexural uplift and subsidence) affecting landscape evolution. The elastic flexure models constructed in this study for isostatic adjustments from changing surface loads provide insight into the late-Cenozoic landscape evolution of the western Canadian Arctic. The results strongly favor the hypothesis by others that until the end of the Pliocene, the western Arctic Archipelago, and possibly lowlands farther east, were covered by the Beaufort Formation and that the incision of the Northwest Passages occurred in the Pleistocene.

References

Ballantyne, A. P., Greenwood, D. R., Sinninghe Damsté, J. S., Csank, A. Z., Eberle, J. J., and Rybczynski, N., 2010, Significantly warmer Arctic surface temperatures during the Pliocene indicated by multiple independent proxies: Geology, v. 38, no. 7, p. 603.

Ballantyne, A. P., Rybczynski, N., Baker, P. A., Harington, C. R., and White, D., 2006, Pliocene Arctic temperature constraints from the growth rings and isotopic composition of fossil larch: Palaeogeography, Palaeoclimatology, Palaeoecology, v. 242, no. 3, p. 188-200.

Barendregt, R. W., Vincent, J. S., Irving, E., and Baker, J., 1998, Magnetostratigraphy of Quaternary and late Tertiary sediments on Banks Island, Canadian Arctic Archipelago: Canadian Journal of Earth Sciences, v. 35, no. 2, p. 147-161.

Barrell, J. C. F. p. d. N. D., 1914, The Strength of the Earth's Crust: The Journal of Geology, v. 22, no. 8, p. 729-741.

Beaumont, C., Quinlan, G., and Hamilton, J., 1988, Orogeny and Stratigraphy: Numerical Models of the Paleozoic in the Eastern Interior of North America: Tectonics, v. 7, no. 3, p. 389-416.

Berton, P., 2001, The Arctic Grail: The Quest for the North West Passage and the North Pole, 1818-1909, Random House Incorporated.

Blum, M. D., and Aslan, A., 2006, Signatures of climate vs. sea-level change within incised valley-fill successions: Quaternary examples from the Texas GULF Coast: Sedimentology and Sequence Stratigraphy of Fluvial DepositsA Tribute to Andrew Miall17th International Sedimentological Congress, v. 190, no. 1–4, p. 177-211.

Braschi, L. C., 2015, Chronostratigraphy of the Beaufort Formation, western Canadian Arctic Archipelago [Master of Science: Dalhousie University, 243 p.

Brigham-Grette, J., and Carter, L. D., 1992, Pliocene Marine Transgressions of Northern Alaska: Circumarctic Correlations and Paleoclimatic Interpretations: ARCTIC; Vol 45, No 1 (1992): March: 1–104.

Burov, E. B., 2010, The equivalent elastic thickness (Te), seismicity and the long-term rheology of continental lithosphere: Time to burn-out “creme brulee”? Insights from large-scale geodynamic modeling: Tectonophysics, v. 484, p. 4-26.

Burov, E. B., 2011, Rheology and strength of the lithosphere: Marine and Petroleum Geology, v. 28, no. 8, p. 1402-1443.

Bustin, R. M., 1986, Organic maturity of late Cretaceous and Tertiary coal measures, Canadian Arctic Archipelago: International Journal of Coal Geology, v. 6, p. 71-106.

Caldwell, J. G., and Turcotte, D. L., 1979, Dependence of the thickness of the elastic oceanic lithosphere on age: Journal of Geophysical Research: Solid Earth, v. 84, no. B13, p. 7572-7576.

Chandan, D., and Peltier, W. R., 2017, Regional and global climate for the mid-Pliocene using CCSM4 and PlioMIP2 boundary conditions: Climate of the Past: Discussions, v. 2017, p. 1-41.

Chian, D., Jackson, H. R., Hutchinson, D. R., Shimeld, J. W., Oakey, G. N., Lebedeva-Ivanova, N., Li, Q., Saltus, R. W., and Mosher, D. C., 2016, Distribution of crustal types in Canada Basin, Arctic Ocean: Tectonophysics, v. 691, p. 8-30.

Csank, A. Z., Tripati, A. K., Patterson, W. P., Eagle, R. A., Rybczynski, N., Ballantyne, A. P., and Eiler, J. M., 2011, Estimates of Arctic land surface temperatures during the early Pliocene from two novel proxies: Earth and Planetary Science Letters, v. 304, no. 3, p. 291-299.

De Paor, D. G., Bradley, D. C., Eisenstadt, G., and Phillips, S. M., 1989, The Arctic Eurekan orogen: A most unusual fold-and-thrust belt: Geological Society of America Bulletin, v. 101, no. 7, p. 952-967.

Dyke, A. S., and Prest, V. K., 1987, Late Wisconsinan and Holocene history of the Laurentide ice sheet: Géographie physique et Quaternaire, v. 41, no. 2, p. 237-263.

Eaton, D. W., Darbyshire, F., Evans, R. L., Grütter, H., Jones, A. G., and Yuan, X., 2009, The elusive lithosphere–asthenosphere boundary (LAB) beneath cratons: Continental Lithospheric Mantle: The Petro-Geophysical ApproachThe Structure of the Lithosphere: the petro-geophysical approach, v. 109, no. 1–2, p. 1-22.

England, J., 1987, Glaciation and the Evolution of the Canadian High Arctic Landscape: Geology, v. 15, p. 419-424.

England, J., Atkinson, N., Bednarski, J., Dyke, A. S., Hodgson, D. A., and Ó Cofaigh, C., 2006, The Innuitian Ice Sheet: configuration, dynamics and chronology: Quaternary Science Reviews, v. 25, no. 7–8, p. 689-703.

Flück, P., Hyndman, R. D., and Lowe, C., 2003, Effective elastic thickness Te of the lithosphere in western Canada: Journal of Geophysical Research: Solid Earth, v. 108, no. B9, p. n/a-n/a.

Fyles, J. G., 1990, Beaufort Formation (Late Tertiary) as Seen from Prince Patrick Island, Arctic Canada: Arctic, v. 43, no. 4, p. 393-403.

Fyles, J. G., Hills, L. V., Matthews, J. V. J., Barendregt, R., Baker, J., Irving, e., and Jette , H., 1994, Ballast Brook and Beaufort Formations (Late Tertiary) on Northern Banks Island, Arctic Canada: Quaternary International, v. 22/23, p. 141-171.

Gosse, J. C., Ballantyne, A., Barker, J., Csank, A., Fletcher, T., Grant, G., Greenwood, D., McPhee, R., and Rybczynski, N., submitted 2017, POLAR-FIT: PliOcene Landscape and Arctic Remains, Frozen In Time: Geoscience Canada.

Hansen, J., Sato, M., Russell, G., and Kharecha, P., 2013, Climate sensitivity, sea level and atmospheric carbon dioxide: Philosophical Transactions of the Royal Society A: Mathematical, Physical and Engineering Sciences, v. 371, no. 2001.

Harrison, J. C., and Brent, T. A., 2005, Basins and Fold Belts of Prince Patrick Island and Adjacent Areas, Canadian Arctic Islands, Volume Bulletin 560, Geological Survey of Canada, p. 211.

Helwig, J., Kumar, N., Emmet, P., and Dinkelman, M., 2011, Regional seismic interpretation of crustal framework, Canadian Arctic passive margin, Beaufort Sea, with comments on petroleum potential: Geological Society, London, Memoirs, v. 35, no. 1, p. 527-543.

Houseknecht, D. W., and Bird, K. J., 2011, Geology and Petroleum Potential of the Rifted Margins of the Canada Basin: The Geological Society of London.

Jakobsson, M., Macnab, R., Mayer, L., Anderson, R., Edwards, M., Hatzky, J., Schenke, H. W., and Johnson, P. C. L., 2008, An improved bathymetric portrayal of the Arctic Ocean: Implications for ocean modeling and geological, geophysical and oceanographic analyses: Geophysical Research Letters, v. 35, no. 7, p. n/a-n/a.

Japsen, P., Bonow, J. M., Green, P. F., Chalmers, J. A., and Lidmar-Bergström, K., 2006, Elevated, passive continental margins: Long-term highs or Neogene uplifts? New evidence from West Greenland: Earth and Planetary Science Letters, v. 248, no. 1–2, p. 330-339.

Japsen, P., and Chalmers, J. A., 2000, Neogene Uplift and Tectonics Around the North Atlantic: Global and Planetary Change, v. 24, p. 165-173.

Karlstrom, K. E., Crow, R., Crossey, L. J., Coblentz, D., and Van Wijk, J. W., 2008, Model for tectonically driven incision of the younger than 6 Ma Grand Canyon: Geology, v. 36, no. 11, p. 835.

Lakeman, T. R., and England, J. H., 2012, Paleoglaciological insights from the age and morphology of the Jesse moraine belt, western Canadian Arctic: Quaternary Science Reviews, v. 47, p. 82-100.

Lazear, G., Karlstrom, K., Aslan, A., and Kelley, S., 2013, Denudation and flexural isostatic response of the Colorado Plateau and southern Rocky Mountains region since 10 Ma: Geosphere, v. 9, no. 4, p. 792-814.

Lisiecki, L. E., and Raymo, M. E., 2005, Pliocene-Pleistocene stack of globally distributed benthic stable oxygen isotope records, Supplement to: Lisiecki, LE; Raymo, ME (2005): A Pliocene-Pleistocene stack of 57 globally distributed benthic d18O records. Paleoceanography, 20, PA1003, doi:10.1029/2004PA001071, PANGAEA.

Lowry, A. R., Ribe, N. M., and Smith, R. B., 2000, Dynamic elevation of the Cordillera, western United States: Journal of Geophysical Research: Solid Earth, v. 105, no. B10, p. 23371-23390.

MacLean, B., Blasco, S., Bennett, R., Lakeman, T., Hughes-Clarke, J., Kuus, P., and Patton, E., 2015, New marine evidence for a Late Wisconsinan ice stream in Amundsen Gulf, Arctic Canada: Quaternary Science Reviews, v. 114, p. 149-166.

Malone, S. J., McClelland, W. C., von Gosen, W., and Piepjohn, K., 2014, Proterozoic Evolution of the North Atlantic–Arctic Caledonides: Insights from Detrital Zircon Analysis of Metasedimentary Rocks from the Pearya Terrane, Canadian High Arctic: The Journal of Geology, v. 122, no. 6, p. 623-647.

Matthews, J. V., and Ovenden, L. E., 1990, Late Tertiary Plant Macrofossils from Localities in Arctic/Subarctic North America: A Review of the Data: Arctic, v. 43, no. 4, p. 364-392.

McNeil, D. H., Duk-Rodkin, A., Dixon, J., Dietrich, J. R., and et al., 2001, Sequence stratigraphy, biotic change, (87)Sr/(86)Sr record, paleoclimatic history, and sedimentation rate change across a regional late Cenozoic unconformity in Arctic Canada: Canadian Journal of Earth Sciences, v. 38, no. 2, p. 309-331.

Medvedev, S., Hartz, E. H., and Podladchikov, Y. Y., 2008, Vertical motions of the fjord regions of central East Greenland: Impact of glacial erosion, deposition, and isostasy: Geology, v. 36, no. 7, p. 539.

Medvedev, S., Souche, A., and Hartz, E. H., 2013, Influence of ice sheet and glacial erosion on passive margins of Greenland: Geomorphology, v. 193, p. 36-46.

Miall, A. D., 1976, Sedimentary structures and paleocurrents in a Tertiary deltaic succession, northern Banks Basin, Arctic Canada: Canadian Journal of Earth Sciences, v. 13, no. 10, p. 1422-1432.

Miall, A. D., 1984, Sedimentation and tectonics of a diffuse plate boundary: the Canadian Arctic island from 80 Ma B.P. to the present: Tectonophysics, v. 107, p. 261-277.

Molnar, P., and England, P., 1990, Late Cenozoic uplift of mountain ranges and global climate change: chicken or egg?: Nature, v. 346, no. 6279, p. 29-34.
Moore, P. D., and Bellamy, D. J., 1974, Peatlands, Springer-Verlag.
Moucha, R., Forte, A. M., Mitrovica, J. X., Rowley, D. B., Quéré, S., Simmons, N. A., and Grand, S. P., 2008, Dynamic topography and long-term sea-level variations: There is no such thing as a stable continental platform: Earth and Planetary Science Letters, v. 271, no. 1–4, p. 101-108.
Moucha, R., Forte, A. M., Rowley, D. B., Mitrovica, J. X., Simmons, N. A., and Grand, S. P., 2009, Deep mantle forces and the uplift of the Colorado Plateau: Geophysical Research Letters, v. 36, no. 19.
Pedersen, V. K., Huismans, R. S., and Moucha, R., 2016, Isostatic and dynamic support of high topography on a North Atlantic passive margin: Earth and Planetary Science Letters, v. 446, p. 1-9.
Pederson, J. L., Mackley, R. D., and Eddleman, J. L., 2002, Colorado Plateau uplift and erosion evaluated using GIS: GSA Today, p. 4-10.
Roberts, G. G., White, N. J., Martin-Brandis, G. L., and Crosby, A. G. C. T., 2012, An uplift history of the Colorado Plateau and its surroundings from inverse modeling of longitudinal river profiles: Tectonics, v. 31, no. 4, p. n/a-n/a.
Roy, M., Jordan, T. H., and Pederson, J., 2009, Colorado Plateau magmatism and uplift by warming of heterogeneous lithosphere: Nature, v. 459, no. 7249, p. 978-982.
Rybczynski, N., Gosse, J. C., Harington, R., Wogelius, R. A., Higy, A. J., and Buckley, M., 2013, Mid-Pliocene warm-period deposits in the High Arctic yield insight into camel evolution: nature communications, v. 2516, p. 9.
Schaeffer, A. J., and Lebedev, S., 2014, Imaging the North American continent using waveform inversion of global and USArray data: Earth and Planetary Science Letters, v. 402, p. 26-41.
Stokes, C. R., Clark, C. D., Darby, D. A., and Hodgson, D. A., 2005, Late Pleistocene ice export events into the Arctic Ocean from the M'Clure Strait Ice Stream, Canadian Arctic Archipelago: Global and Planetary Change, v. 49, no. 3–4, p. 139-162.
Tesauro, M., Audet, P., Kaban, M. K., Bürgmann, R., and Cloetingh, S., 2012, The effective elastic thickness of the continental lithosphere: Comparison between rheological and inverse approaches: Geochemistry, Geophysics, Geosystems, v. 13, no. 9, p. n/a-n/a.
Tozer, E. T., 1955, Geological reconnaissance : Prince Patrick, Eglinton, and western Melville islands, Arctic Archipelago, Northwest Territories, Ottawa, Ottawa : Dept. of Mines and Technical Surveys.
Tufano, B. C., 2016, Coupled flexural-dynamic subsidence modeling of a retro-foreland basin, Western Canada Sedimentary Basin10134290]: State University of New York at Binghamton, 147 p.
Turcotte, D. L., and Barry, S., 1979, Flexure, Advances in Geophysics, Volume Volume 21, Elsevier, p. 51-86.
van Wees, J. D., and Cloetingh, S., 1994, A finite-difference technique to incorporate spatial in rigidity and planar faults into 3-D models for lithospheric flexure, v. 117, p. 179-195.
Wickert, A. D., 2016, Open-source modular solutions for flexural isostasy: gFlex v1.0: Geoscientific Model Development, v. 9, no. 3, p. 997-1017.

Appendix A - gFlex and model codes

gFlex incorporates parameter inputs such as density of mantle (ρ_m), Young's Modulus (E), Poisson's Ratio (ν), horizontal spacing (dx), vertical spacing (dy), and model boundary conditions. Surface loads can either be generated from reading text files or populated through code in the python script. A beneficial feature in gFlex is the ability to incorporate a variable elastic thickness (T_e), allowing for variations in elastic strength of the lithosphere to be incorporated into the model. The following section provides the codes used in modelling in this study.

gFlex

```
import gflex
import numpy as np
from matplotlib import pyplot as plt

flex=gflex.F2D()    ### dimension of model, 1D or 2D ###
flex.Quiet=False
flex.Debug=False
flex.Verbose=False
flex.Method='FD'      ### finite-difference method ###
flex.PlateSolutionType='vWC1994'   ### solution type outlined in van Wees and
Cloetingh (1994) ##
flex.Solver='direct'
convergence=0.001   ### precision of model output ###

flex.g=9.81  ### Gravity constant ###
flex.E=65E9  ### Young's Modulus ###
flex.nu=0.27 ### Poissons' Ratio ###
flex.rho_m=3300 ### Mantle density ###
flex.rho_fill=0 ### Density of infilling material ###

flex.Te=30000                    ### elastic thickness ###
flex.qs=np.genfromtxt('PF_30_q14.txt')  ### load generated from text file array ###
flex.dx=2000                     ### grid spacing x direction ###
flex.dy=2000                     ### grid spacing y direction, 2D model only ###

flex.BC_W='Mirror'  ### model boundary conditions for 2D, only W and E for 1D ###
flex.BC_E='Mirror'
flex.BC_S='Periodic'
flex.BC_N='Periodic'
```

```
flex.initialize()
flex.run()
flex.finalize()

#flex.plotChoice='both'
flex.wOutFile='PF_30_out15.txt'  ### deflection output ###
flex.output()
```

Model Elevation

```
import numpy as np
import re
fixtext = re.compile("\r\n|\r|\n")

Output = open('PF_30_out15.txt','r')       ### deflection output from gFlex ###
Input = open('PF_30_q14.txt','r')          ### net applied load ###
Fgrav = open('PF_gravfull.txt','r')        ### load conversion factor ###
fwat = open('water.txt','r')               ### calculated water load ###
fpal = open('PF_30_paleosurface.txt','r')   ### initial paleosurface/paleo-elevation ###

x=[]
y=[]
w=[]
m=[]
p=[]
it=[]
qq =[]
zz=[]
rr=[]

for line in Output:
   out = line.split()
   for index in out:
      x.append(float(index))

   grav = Fgrav.readline().split()
   for index in grav:
      y.append(float(index))

   init = Input.readline().split()
   for index in init:
      it.append(float(index))

   wat = fwat.readline().split()
```

```
    for index in wat:
        w.append(float(index))

    pal = fpal.readline().split()
    for index in pal:
        p.append(float(index))

for i in range(len(x)) :
    q = x[i] + ((it[i] - w[i])/y[i]) + p[i]    ### model elevation calculation###
    qq.append(q)

qq_arr=np.array(qq)

with open('PF_30_p15.txt','w') as prof:          ### model elevation output ###
    for i in qq_arr.reshape(849,706):            ###(rows,columns)###
        prof.write(' '.join(map(str, i)) + '\n')

print 'topo calculated'

Output.close();
Input.close();
Fgrav.close();
prof.close();
```

Iteration for incision of channels only

```
import numpy as np
import re
fixtext = re.compile("\r\n|\r|\n")

foutput = open('PF_30_out6.txt','r')  ### deflection output from gFlex ###
fgrav = open('PF_grav.txt','r')       ### masked load conversion (density x g) ###
finitial = open('PF_30_q0.txt','r')   ### Do not change, initial load ###

x=[]
y=[]
it=[]
qq =[]
zz=[]
rr=[]

for line in foutput:
    out = line.split()
    for index in out:
```

```
        x.append(float(index))

    grav = fgrav.readline().split()
    for index in grav:
        y.append(float(index))

    init = finitial.readline().split()
    for index in init:
        it.append(float(index))

for i in range(len(x)) :
    q = it[i] - (x[i]*(y[i]));   ### erode the deflection in the channels and substract from
initial load ###
    qq.append(q)

qq_arr=np.array(qq)

with open('PF_30_q6.txt','w') as fnew:          ### new load ###
    for i in qq_arr.reshape(849,706):           ###(rows,columns)###
        fnew.write(' '.join(map(str, i)) + '\n')


print"new load computed"

foutput.close();
fgrav.close();
finitial.close();
fnew.close();
```

Elevation difference

```
import numpy as np
import re
fixtext = re.compile("\r\n|\r|\n")

Inp = open('PF_30_p14.txt','r')    ### model elevation ###
out = open('aoi_adjust.txt','r')   ### observed topography ###
oss = open('os_mask.txt','r')      ### offshore mask with zeros ###

y=[]
q=[]
z=[]
t=[]
zz=[]
```

```
for line in Inp:

   I = line.split()
   for index in I:
      q.append(float(index))

   O = out.readline().split()
   for index in O:
      y.append(float(index))

   S = oss.readline().split()
   for index in S:
      t.append(float(index))

for i in range(len(q)):

      z = q[i]-y[i]*t[i]   ### difference between model elevation and observed topography,
negating offshore ###
      zz.append(z)

y_arr=np.array(zz)

with  open('topo_diff_8.txt','w') as fnew:      ### calculated difference ###
   for j in y_arr.reshape(849,706):           ###(rows,columns)###
      fnew.write(' '.join(map(str, j)) + '\n')

print 'array adjusted'

Inp.close();
out.close();
oss.close();
```

Masking elevation difference

```
import numpy as np
import re
fixtext = re.compile("\r\n|\r|\n")

Inp = open('topo_diff_8.txt','r')      ### difference between model and observed
topography ###
QIn = open('topo_mask_8.txt','w')      ### masked difference between model and
topography ###

for line in Inp:
```

```
    I = line.split()
    for index in I:
        if float(index)<=(0):       ### select where model is below topography ###
            q = 0
        else:
            q = index               ### leave if model is above topography ###

        QIn.write(str(q) + " ")
    QIn.write("\n")

print 'array adjusted'

Inp.close();
QIn.close();
```

Iteration including erosion on the islands

```
import numpy as np
import re
fixtext = re.compile("\r\n|\r|\n")

foutput = open('topo_mask_8.txt','r')  ### selected (masked) elevation difference ###
fgrav = open('PF_gravfull.txt','r')    ### load conversion across model ###
finitial = open('PF_30_q13.txt','r')   ### previous load ###

x=[]
y=[]
it=[]
qq =[]
zz=[]
rr=[]

for line in foutput:
    out = line.split()
    for index in out:
        x.append(float(index))

    grav = fgrav.readline().split()
    for index in grav:
        y.append(float(index))

    init = finitial.readline().split()
    for index in init:
```

```
        it.append(float(index))

for i in range(len(x)) :
    q = it[i] - (x[i]*(y[i]));  ### remove (substract) elevation difference (load) from the
previous load ###
    qq.append(q)

qq_arr=np.array(qq)

with open('PF_30_q14.txt','w') as fnew:          ### new load ###
    for i in qq_arr.reshape(849,706):            ###(rows,columns)###
        fnew.write(' '.join(map(str, i)) + '\n')


print"new load computed"

foutput.close();
fgrav.close();
finitial.close();
fnew.close();
```

Appendix B - Additional material for models

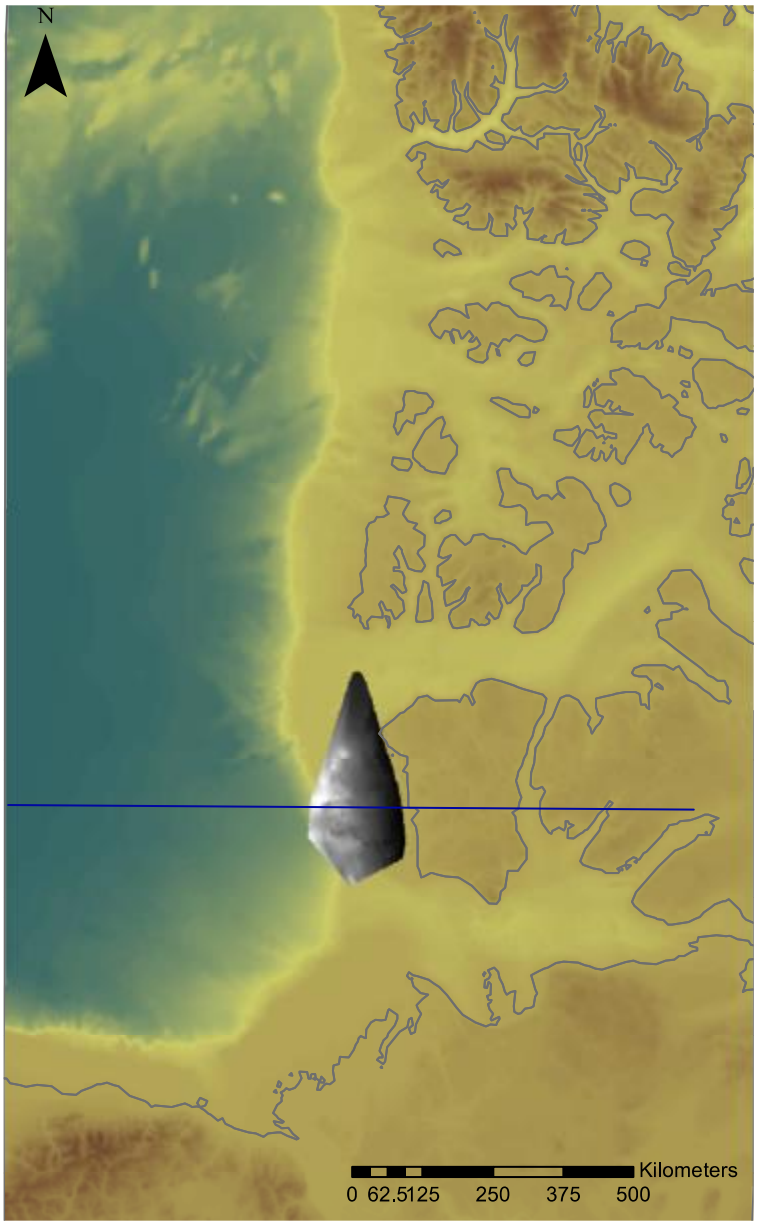

Figure B1 Ariel extent (overlaid grayscale raster) of the seismic data provided by the GSC (pre-stack depth migrated (PSDM) BasinSPAN™ seismic courtesy GX Technology Corporation). Blue line is the east-west transect used in experiment one.

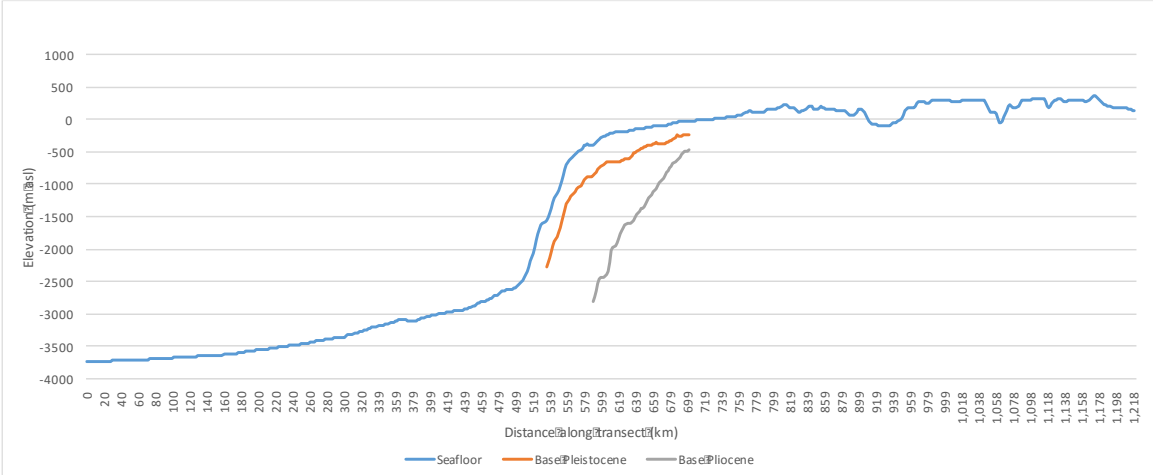

Figure B2: East-west transect through the seismic data provided in (Fig. A1).

Appendix C – Paleosurfaces for erosional isostasy models

Model Paleosurfaces for incision models

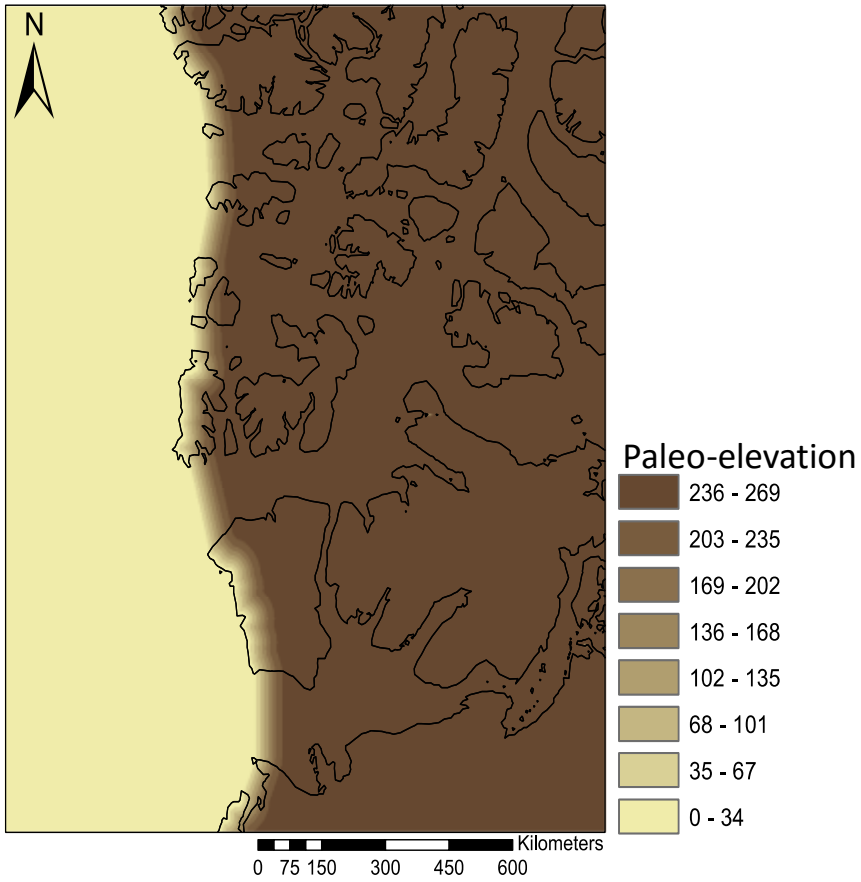

Figure C1 Paleosurface for 30 km T_e erosional isostasy model. Paleo-elevation is measured in metres above modern mean sea-level.

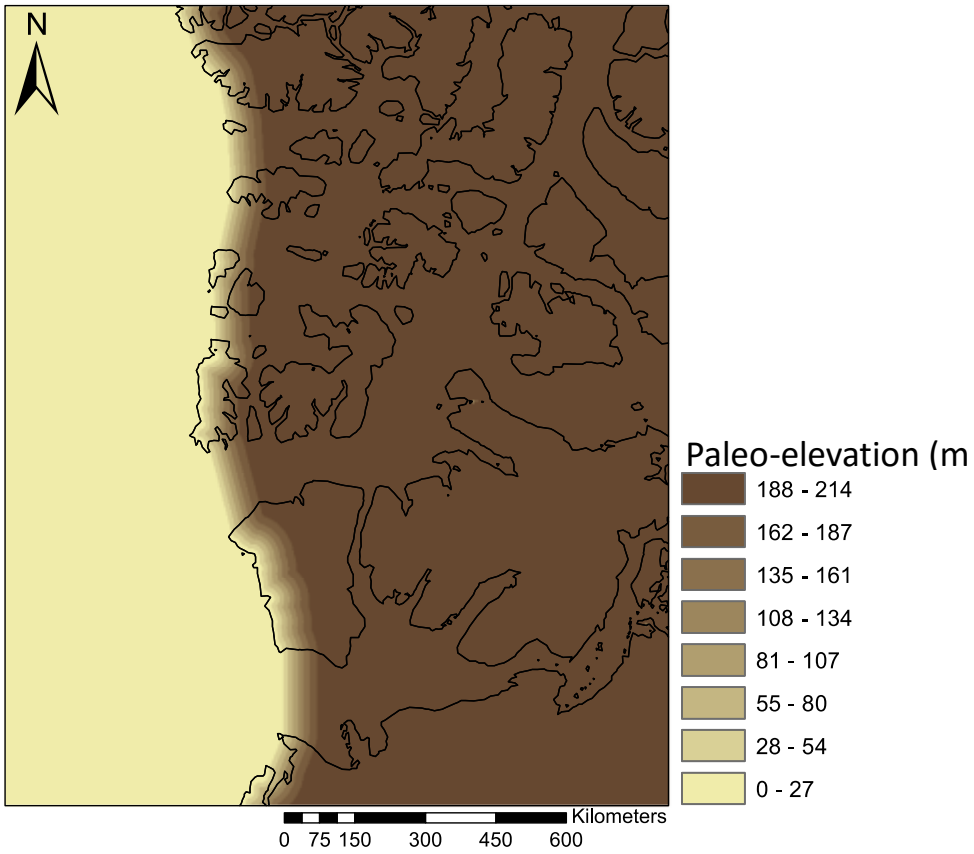

Figure C2 Paleosurface for 60 km T_e erosional isostasy model. Paleo-elevation is measured in metres above modern mean sea-level.

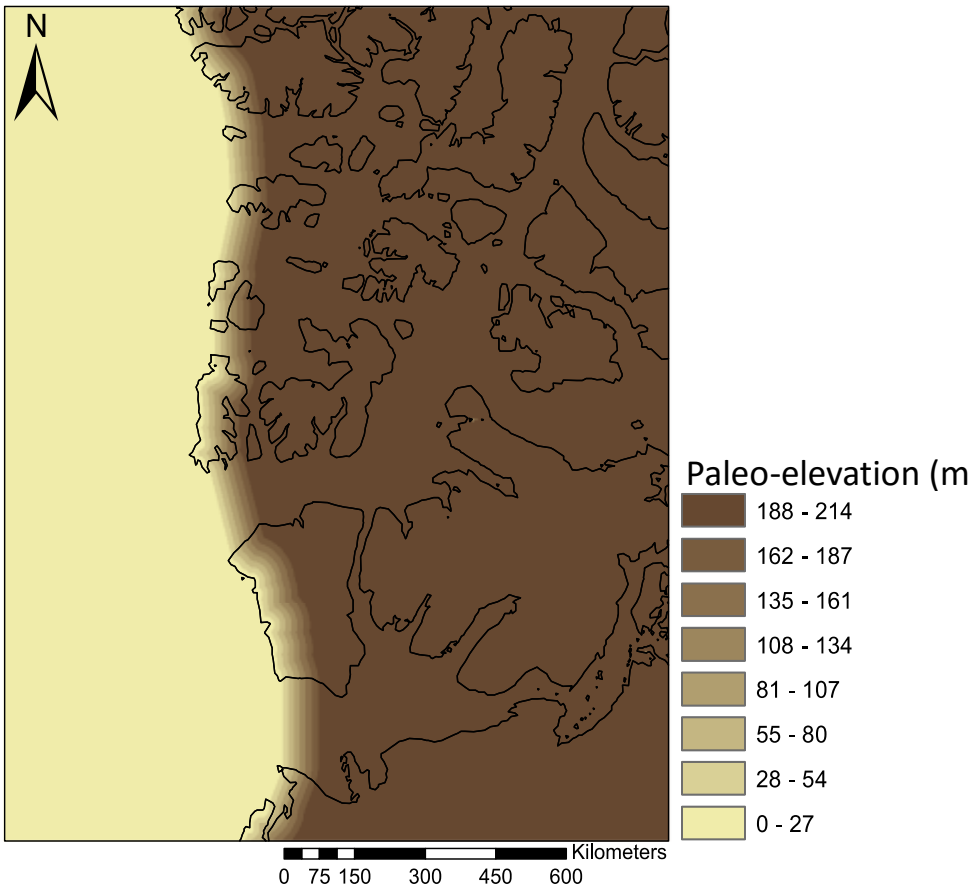

Figure C3 Paleosurface for 90 km T_e erosional isostasy model. Paleo-elevation is measured in metres above modern mean sea-level.